

MASTER OF SCIENCE THESIS

---

# Investigation of Trailing Edge Sub-Components in Wind Turbine Blades

Final Report

Sebastien Lachance-Barrett

---

August 16, 2016

Faculty of Aerospace Engineering · Delft University of Technology



# **Investigation of Trailing Edge Sub-Components in Wind Turbine Blades**

## **Final Report**

MASTER OF SCIENCE THESIS

For obtaining the degree of Master of Science in Aerospace  
Engineering at Delft University of Technology

Sebastien Lachance-Barrett

August 16, 2016



Copyright © Sebastien Lachance-Barrett  
All rights reserved.

DELFT UNIVERSITY OF TECHNOLOGY  
DEPARTMENT OF  
AEROSPACE STRUCTURES AND MATERIALS

The undersigned hereby certify that they have read and recommend to the Faculty of Aerospace Engineering for acceptance a thesis entitled **“Investigation of Trailing Edge Sub-Components in Wind Turbine Blades”** by **Sebastien Lachance-Barrett** in partial fulfillment of the requirements for the degree of **Master of Science**.

Dated: August 16, 2016

Head of department:

\_\_\_\_\_  
Dr. Christos Kassapoglou

Supervisor:

\_\_\_\_\_  
Dr. Sofia Teixeira de Freitas

Reader:

\_\_\_\_\_  
Dr. Kim Branner



---

# Summary

In order to achieve high aerodynamic performance, the trailing edge of wind turbine blades is designed to be very thin. One major drawback is that it makes this region susceptible to buckling which in turn often leads to failure due to debonding. There is high interest in the industry to investigate the buckling behavior of the trailing edge section of wind turbine blades in order to reduce failure in this region. A promising experimental technique, called sub-component testing, aims at testing critical regions of the blades, such as the trailing edge. Sub-component testing of cut-out trailing edge sections is quite challenging, however, because it is difficult to accurately load the specimen such as to mimic the loading seen by the full-blade and to obtain results that are not influenced by boundary effects. So far, no clear solutions has been found to solve these problems. This research project aims to find solutions to solve these two problems by performing numerical simulations using the finite-element software Abaqus.

A numerical model was first created to replicate a preliminary buckling experiment done on a 3 m cut-out section of a 34 m SSP blade. This model was then used for three other 3 m blade sections coming from different radial distances along the full blade. The goal was to understand how to best cut their cross-sections such that the applied loading would closely match that of the full-scale. Buckling simulations were then performed on these sections to try to predict how they would naturally buckle. The sections were inspected to understand why some would buckle close to the boundaries while others would not. The buckling location was determined to be affected mainly by a variation in panel flexural stiffness along the specimen length due to some panels having different core thicknesses, and from a lesser extent to the difference in distance between the panels from one end of the blade section to the other. These findings reveal that solutions to shift the buckling wave towards the center of the specimen should be directed towards making the panels have relatively constant flexural rigidity. This flexural rigidity is proposed to be tuned by either applying over-lamination and/or implementing a slim cut in the specimen. This thesis provides a wealth of results that sets the stage for further developments of this promising testing procedure.



---

# Acknowledgements

I would first like to thank my thesis supervisors for their valuable input and guidance. Each of my supervisors provided help and support in a unique way and I found their diversity in opinions and background to be extremely valuable.

Thank you to Kim Branner, senior scientist at the Technical University of Denmark (DTU), for his help in defining the thesis project, and to clearly communicate the direction to take and the end goals to strive for.

Thank you to Philipp Ulrich Haselbach, postdoc at DTU, for his patience, availability and willingness to help me on a frequent basis. I owe Philipp my deepest gratitude for his time teaching me how to use the finite-element software Abaqus, troubleshooting problems with my simulations and providing very thorough feedback on my draft reports. It was a real pleasure working with Philipp and I could not have asked for a better daily supervisor.

Thank you to Sofia Teixeira de Freitas, assistant professor at Delft University of Technology (TU Delft), for her constructive feedback on my draft reports, for providing structure in the thesis project and for enforcing the deadlines even from far away. While the topic of this thesis fell outside of Sofia's main area of expertise, her outsider's perspective was actually extremely welcomed because it greatly helped improve the clarity of the text.

Thank you to Peter Joosse, structural designer at Suzlon Blades Technology, for sharing his wisdom from an industry perspective. His insightful comments during meetings and in the draft reports were very well appreciated. Also a big thank you to Suzlon for providing me with financial assistance. I hope that this thesis helped Suzlon gain a better understanding of trailing edge sub-component testing and that it will help them adopt this testing method in the near future, if it is not already in the works.

I would then like to express my sincere gratitude to Malo Rosemeier, research associate at IWES Fraunhofer Institute for Wind Energy, and to Peter Berring, senior development engineer at DTU, for their constructive inputs during our meetings at DTU Risø Campus.

I would also like to thank my committee chair, Christos Kassapoglou, associate professor at TU Delft, for reading and evaluating this work. Christos is an excellent professor who

happened to teach my favorite course of my master program called Design and Analysis of Composite Structures 1.

Finally, I would like to express my deepest appreciation to my family for their constant encouragement during this endeavor. This thesis would not have been possible without their love and support.

Copenhagen, Denmark  
August 16, 2016

Sebastien Lachance-Barrett

---

# Contents

<b>Summary</b>	<b>v</b>
<b>Acknowledgements</b>	<b>vii</b>
<b>Nomenclature</b>	<b>xiii</b>
<b>1 Introduction</b>	<b>1</b>
<b>2 Literature Review</b>	<b>3</b>
2.1 Sub-Component Testing . . . . .	3
2.2 Buckling: Concept and Definition . . . . .	9
2.3 Buckling Numerical Analysis . . . . .	13
2.3.1 Linear Eigenvalue Buckling Analysis . . . . .	14
2.3.2 Nonlinear Static Analysis . . . . .	15
2.3.3 Dynamic Implicit Analysis . . . . .	16
2.4 Buckling Analysis of Wind Turbine Blades . . . . .	17
2.4.1 Industry Guidelines . . . . .	17
2.4.2 Buckling in Full-Scale Tests . . . . .	19
2.4.3 Buckling in Sub-Components . . . . .	21
2.5 Buckling Analysis of Aerospace Structures . . . . .	23
2.6 Final Remarks . . . . .	25
2.7 Research Questions, Objective and Sub-Goals . . . . .	26
<b>3 Validation of Numerical Model with Previous Experiment</b>	<b>29</b>
3.1 Test Specifications . . . . .	29
3.2 Modelling Approach . . . . .	33
3.2.1 Full-Scale Blade Model . . . . .	33
3.2.2 Blade Section . . . . .	34

3.2.3	Plates and Assembly . . . . .	35
3.2.4	Boundary Conditions . . . . .	38
3.2.5	Elements and Meshes . . . . .	39
3.2.6	Analysis Types . . . . .	40
3.3	Results . . . . .	41
3.3.1	Results of Mesh Refinement Study . . . . .	41
3.3.2	Linear Eigenvalue Buckling Analysis Results . . . . .	43
3.3.3	Nonlinear Analysis Results . . . . .	44
3.4	Side Study #1: Effect of Imperfections . . . . .	51
3.5	Side study #2: Effect of Blade Angle . . . . .	52
3.6	Analysis and Discussion . . . . .	55
<b>4</b>	<b>Simulation of Full-Scale Blade Model under LTT Loading</b>	<b>57</b>
4.1	Simulation Setup . . . . .	58
4.2	Method for Obtaining Longitudinal Strain . . . . .	59
4.3	Results . . . . .	63
4.3.1	Global Deformation and Longitudinal Strain Field. . . . .	63
4.3.2	Results Between Automatic and Manual Averaging of Strain . . . . .	64
4.3.3	Longitudinal Strain vs. Z-Location . . . . .	67
4.3.4	Longitudinal Strain vs. Load Levels . . . . .	68
4.3.5	Verification of Results With a Different Model . . . . .	70
<b>5</b>	<b>Comparison of Local Loading Between Full-Scale and Sub-Component</b>	<b>75</b>
5.1	Description of the Blade Sections . . . . .	75
5.2	Methodology of the Transverse Cut . . . . .	76
5.3	Simulation Set-Up . . . . .	80
5.4	Results . . . . .	83
5.5	Discussion . . . . .	93
<b>6</b>	<b>Buckling Analysis of the Three Sections</b>	<b>97</b>
6.1	14.5 Section . . . . .	98
6.2	19.4 Section . . . . .	102
6.3	20.75 Section . . . . .	105
6.4	Discussion . . . . .	107
<b>7</b>	<b>Factors Affecting Buckling Wave Location</b>	<b>111</b>
7.1	Inspection of the Blade Section Geometries . . . . .	111
7.2	Inspection of the Composite Design . . . . .	116
7.3	Discussion . . . . .	120
<b>8</b>	<b>Solutions to Translate the Buckling Wave</b>	<b>123</b>
8.1	Cutting Away a Section of the Blade . . . . .	123
8.2	Recommended Solutions to Attempt Next . . . . .	128
<b>9</b>	<b>Conclusion</b>	<b>131</b>
	<b>References</b>	<b>135</b>





---

# Nomenclature

DNV	Det Norske Veritas
DTU	Technical University of Denmark
FEA	Finite-Element Analysis
GL	Germanischer Lloyd
HAWC2	Horizontal Axis Wind turbine simulation Code 2nd generation
IEC	International Electrotechnical Commission
LTT	Leading Towards Trailing
MPC	Multi-Point Constraint
NREL	National Renewable Energy Laboratory
SSP	SSP Technology
TU Delft	Delft University of Technology



---

# Chapter 1

---

## Introduction

Trailing edge failure of wind turbine blades accounts for 35 percent of wind turbine rotor failure and leads to increased downtime and operating costs [1]. It is therefore a critical area to investigate for failure analysis. This region is highly complex due to its cross-sectional curvature, the transition from sandwich to pure laminate and the transfer of loads from the caps/box girder to the trailing edge giving a complex load field. Additionally, the presence of adhesive joints at the trailing edge increases the complexity of the section. While higher aerodynamic performance is achieved when the trailing edge is thin, it has the drawback of making the region prone to buckling. This instability induced failure mode is often the critical parameter for wind turbine blade failure as it often leads to debonding of the trailing edge [2] [3].

The standard approach to verify the integrity of the blades, including the trailing edge region, is by performing full-scale tests. Both static and dynamic tests are done following the IEC 61400-23 [4] standard on full-scale testing. While this test method is very realistic, it is very expensive and time consuming. The cost of the blade to be tested to failure is very high, and the dynamic test can take several months to complete.

An alternative approach is to determine the structural response and load bearing capacity of selected parts or sections. This testing method, called sub-component testing, while being relatively new to the wind energy industry, shows great potential to become a much faster and cheaper method to certify blade designs and is of high interest for the industry.

Numerical and experimental investigations of cut-out trailing edge sections via sub-component testing could therefore help understand the structural response in this region and lead to improved designs. For example, it could be used to evaluate trailing edge adhesive thicknesses or assess trailing edge adhesive manufacturing techniques. However, testing of cut-out trailing edge specimen under compressive loading, which is the load configuration that leads to the dominant failure mode of trailing edge panel buckling, is very challenging and no significant work has been done on this topic. The challenges mainly arise from the complexity of the trailing edge section coupled with the challenges brought by the sub-component testing methodology. These extra challenges are more specifically to accurately load the specimen such as to mimic the loading seen by the full-blade and

to obtain results that are not influenced by boundary effects. So far, no clear solutions has been found to solve these problems.

As a matter of fact, the Technical University of Denmark (DTU) recently developed a test rig for compression of trailing edge panels and found from a preliminary test that a crack initiated at the boundary and clearly influenced the failure of the specimen [3]. The study concluded that more analysis is needed to move the buckling wave towards the middle of the specimen in order to reduce the influence of the boundaries.

The thesis project aims to solve the problems associated with sub-component testing with specific application to wind turbine blade trailing edge sections. More specifically, the aim is to mitigate boundary condition effects during static compression loading such that the buckling behavior of the blade piece from testing correctly mimics the condition seen by the blade in full-size testing and in the field. This would be achieved by analyzing different solutions with the help of numerical and experimental methods in order to move the buckling wave toward the center of the specimen. The setup should also mimic the internal loading of the full-blade that is subjected to edgewise loading. The thesis project is a direct continuation of the preliminary study on trailing edge sub-component testing at DTU.

Solving these problems could benefit wind turbine manufacturers in successfully implementing state of the art sub-component testing in their testing procedures, with the end goal of increasing the reliability of the blades and reduce development cost and time of new blade designs.

The thesis report is organized as follows. An in-depth literature review is provided in Chapter 2 on sub-component testing, buckling theory, buckling of wind turbine blades and buckling in aerospace structures. This is then followed by the research questions and objectives of the thesis project. Chapter 3 is about creating the model and simulating the first buckling experiment performed at DTU. In Chapter 4, the full-scale blade model is loaded such that the trailing edge sees a compressive loading and the longitudinal strain distribution is then extracted at selected cross-sections. Chapter 5 is about loading three different blade sections with the numerical model that was created and modify these sections in order to try to match the longitudinal strain on these sections with the longitudinal strain found from the full-scale simulation. In Chapter 6, buckling analyses are performed on the three sections and their responses are investigated to detect any trends. In Chapter 7, the geometry and composite details of these sections are inspected to find explanations for the results in Chapter 6. Finally, the knowledge gained is then applied in Chapter 8 to test and suggest different solutions to solve the boundary effect and loading distribution problems of trailing edge sub-component testing.

---

## Chapter 2

---

# Literature Review

With the aim of the thesis being to address some of the main challenges of trailing edge sub-component testing, namely boundary condition effects and accurate load introduction, the literature study aims to provide a review of past buckling experiments of wind turbine blades and of similar-sized composite specimens as trailing edge sub-components in the research project in order to grasp industry best practices in experimental and numerical work. The review starts by giving a thorough introduction of sub-component testing methodology. Then, since the project involves looking into the buckling behavior of the structure, the concept of buckling is explained in detail. This is followed by an overview of industry guidelines on buckling analysis of wind turbine blades, full-scale buckling tests from prior studies and numerical buckling analysis of blade sections. The review then goes over relevant sub-components buckling experiments from aerospace engineering since it contains a lot more information on this type of study, being a more mature field than wind energy. Special attention is put on methods taken by previous projects to address boundary effects, numerical modeling approaches, measurement techniques and obtained results. This information is then evaluated and analyzed in order to provide a solid knowledge foundation for the present thesis project.

### 2.1 Sub-Component Testing

This section aims to deliver an understanding of current industry practices with regards to testing procedures, with particular attention to the concept of sub-component testing.

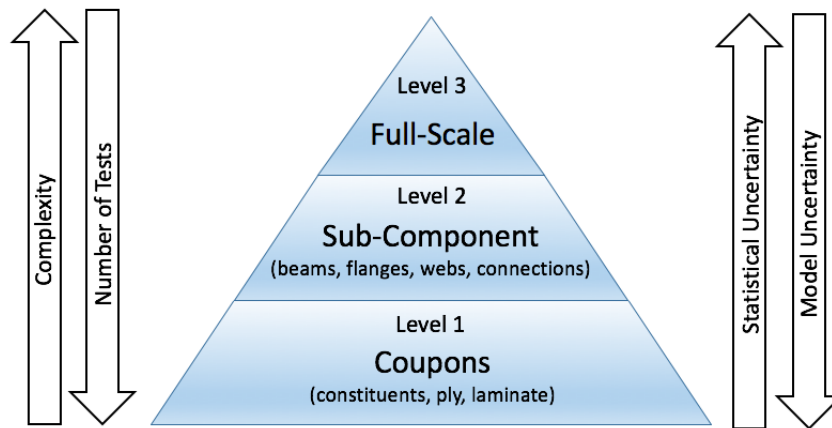


**Figure 2.1:** Illustration of the test pyramid.

The design of wind turbine blades includes tests of different scales and are often broken down by the levels shown in Figure 2.1. The traditional practice is for the material properties to be determined via small coupon tests, while in a later stage, full-scale blade tests are to be performed to verify the results predicted by the numerical model of the blades. Often no intermediate stage tests are done between coupon and full-scale tests.

At the coupon level, small specimens made out of the basic materials used in the blade are tested in order to determine their materials properties for both tensile and fatigue limit states. Since the specimens are relatively inexpensive to manufacture and because testing time is relatively quick, many repetitions can be performed. This in turn minimizes the statistical uncertainty of the results. The material properties are then fed as inputs in the numerical model of the blade.

At the full-scale level, full-scale prototypes of the blades are tested both statically and dynamically according to the IEC 61400-23 [4] standard on full-scale tests. These tests are done at the end of the design process to ensure that the numerical model correctly predicted the load-carrying capability of the blades. While the full-scale test is very realistic in that the final structure is tested in its whole and that it can capture some failure modes not seen in other test, it does have important disadvantages [3].

- The tests are very expensive and time-consuming. The cost of the blade to be failed is very high and the fact that the fatigue test requires several months to complete also induces costs due to greater time to market.
- They are usually performed at the end of the design process as a last verification step. Design iterations at this stage based on the results are therefore highly unpractical and could further increase cost and time-to-market.
- Only one blade is tested. The results are therefore prone to blade-to-blade variations which are then accounted for in conservative safety factors which then leads to more conservative and expensive designs.
- Fatigue testing approaches do not represent reality very well because the blades are made to constantly oscillate at their first natural frequency (while they are designed to operate away from their natural frequencies) and at higher loadings than seen in

the field. This is done in order to minimize the energy required to run the test and to lower the number of cycles needed.

One possibility that can resolve some of these problems is to perform down-scaled tests. In this way, the costs are much lower, a larger number of tests can be performed and these tests could appear earlier in the design process. However, it has many disadvantages that make these methods not ready to become a useful tool in the industry and to be accepted by certifying companies. It is not clear how well the down-scaled blade represents the real blade, how to down-scale a composite layup, how the manufacturing errors in the down-scaled blade are representative of the manufacturing errors in full-scale blades and new moulds would have to be made for the down-scaled blades [3]. A lot more research is needed before it can be useful for the wind energy industry and it is not clear whether it is a direction to move into.

Another experimental test method, called sub-component testing, is the testing of selected parts or sections of the full structure. Sub-component testing aims at only testing the structural response and load bearing capacity of the most complex and critical regions of the blade and to verify the numerical models for critical details. They lie at an intermediate level between coupon tests and full-scale tests in terms of complexity, number of tests performed, statistical uncertainty and model uncertainty as illustrated in Figure 2.1. Thus, its complexity lying between coupons and full-scale means that a few tests are performed for each sub-component.

Sub-component testing plays a very important role in experimental research but are still in its infancy in the wind energy field. It offers the advantage of cost and time savings compared with the costs of full-scale tests. This then makes it much easier to test radically new designs because less money and time is lost if the design does not work. Unlike down-scaled testing, they do not suffer from size effects which are particularly problematic in the area of fracture mechanics since material plasticity does not scale with size, and that fracture location and fracture modes might differ significantly [3]. This means that it is important that the sub-component has similar size like that of the full-scale. However, the challenge with sub-component testing is to correctly mimic the force and displacement boundary conditions on the edges of the specimen such that it realistically represents full-scale loading. The application of the boundary conditions should also not influence the results. For example, a crack forming at the edge is an indication that the boundary condition could have reduced the strength from a stress concentration.

Sub-component specimens can be made in the laboratory specifically for testing or be cut-out from actual produced blades. There are advantages and disadvantages in both methods. In general, specimens produced in the laboratory will differ from the manufactured product. The laboratory specimen may be more perfect than the manufactured product because only a few specimens are created and they receive careful attention, or the opposite may be true where the automation has been fine-tuned and variance between specimens is lower. The manufacturing process of wind turbine blades tend not to be as automated as some other industries and so the laboratory specimens tend to be seen as more perfect than the manufactured product. In other words, the accuracy of tolerance is higher and there is less variance present. This means that the results deviate less and it is also easier to compare the results with analytical models. This means however that the

lower scatter of data can lead to results that are non-conservative. Some failure modes might also be missed out [3].

As for the specimens made from cut-out pieces from full-scale blades, the testing will give a more accurate representation of the actual strength of the joint, however, it may lead to a higher scatter of data which ultimately lowers the characteristic strength. Comparison with analytical models might also be more difficult considering that more failure modes can be present [3].

While sub-component testing has been developed by the automotive industry and is also present in civil and aerospace engineering applications, it is relatively new to the wind energy field. Some wind turbine manufacturers have started doing a few laboratory-made specimens. For example, LM Wind Power has made a few specimens in the laboratory to represent the trailing edge of their blades and investigates the effect of different laminate and adhesive thickness on moment applied to failure as well mode I fracture toughness [3]. While these can be seen as relatively small studies and do not form a large part of the design process yet, the situation is likely to change very fast. There is strong interest from the industry to implement sub-component testing on a large scale because it could accelerate the certification process and be cheaper than full-scale testing. Progress is being made not only from the industry side but also from the certification side which will likely accelerate its development very quickly. In December 2015, DNV-GL released their first wind turbine blade standard, named DNV-GL-ST-0379 [5], and it is quite significant because it marks the first time that guidelines on how to do sub-component testing are included in a wind energy standard. The standard states that sub-component testing can be used as part of the design verification process in addition to coupon and full-scale tests or can be used as partial substitute for full-scale blade testing. It also specifically mentions that it should be performed on a few critical regions, like the trailing edge. Other important guidelines given by the standard are:

- “The [sub-component] test specimens shall be representative of the actual blade in terms of materials, structural design, manufacturing processes and quality control
- The specimens shall be built to a geometrical scale of 1:1, unless justification as per section [2.2.6] is provided.
- The size of specimens shall be chosen such that the boundaries do not interfere with the structural response of the area (or a design feature) under investigation.
- The test loads shall be defined such that the local loading conditions of the area (or design feature) under investigation are equivalent to the actual blade structure.”

and that the testing should be accompanied by structural analysis (FEA or analytical methods) to have correspondence in results between the test specimen and the full blade. More specifically, the standard asks for the following comparisons:

- “Predictions from the specimen model compared to the intermediate level test results (such as strain readings).
- Predictions from the actual blade model compared to the full scale blade test results.
- Predictions from the specimen model compared to predictions from the actual blade model.”

Note: The words specimen and intermediate level test refers to the sub-component while the actual blade and full-scale blade test refers to the full-scale blade.

Sub-component testing of wind turbine blades is currently mainly aimed at testing the strength of adhesive bonds and the strength of the root inserts [6]. With the exception of one notable manufacturer, adhesive joints are used to link the bottom and top shells of the wind turbine blades along the whole length of the blade at the leading and trailing edges as well as connecting the spar cap to the shear web. The blades are simply more likely to fail in the joints than in the composite material sections due to abrupt changes in geometry in these sections, creating local stress singularities. The behavior of adhesive joints is very complex and there is a lack of knowledge about them in industry and academia. According to [3], the behavior of adhesive joints are complex because they are affected by:

non-uniform cross-sections struggling with each other caused by taper and twist, cross-sectional curvature of panels associated with ovalization effects (i.e. in-plane cross-section deformations caused by geometric nonlinearity), local buckling effects, and material anisotropy associated with Poisson ratio effects. Furthermore, adhesive joints are affected by adhesive properties, bi-material interface properties (e.g. fiber bridging capabilities), local joint geometry (stiffness) all of which are affected by different manufacturing techniques themselves affecting the presence of flaws and imperfections in the bondline. The complexity is even more increased by the fact that the blades are subject to aero-elastic loads which depend on many factors bearing high levels of uncertainty (e.g. turbulence levels, yaw direction, controller performance, etc.).

In addition to the modeling complexities, the manufacturing also poses issues in that the final product is often not built as it was specifically designed. For example, a small difference in bondline thickness due to not so exact blade dimensions can create large difference on strength compared with what was originally predicted. To remedy these problems, wind turbine manufacturers at best include partial safety factors in order to accommodate the uncertainties from the adhesive joints. The outcome are blades that are heavier and overdesigned without a clear grasp of the issue [3].

In 2015, a national study from the Technical University of Denmark (DTU) found that statically loading a full 34 meter blade (manufactured by SSP Technologies) to failure at its most critical angle created buckling at the trailing edge and led to adhesive bond failure [3]. This occurred on all three blades tested. This clearly showed that adhesive debonding at the trailing occurring from large local buckling waves is an important failure mode that should be studied more thoroughly.

The same study goes into more detail on specific information about trailing edge sub-component made out of cut-out sections. The edge of the sub-component panel is said to be subject to complex 3D stress that varies linearly along the cut. This is because the shells experience out-of-plane and in-plane deformations that involves all six components of the forces in the local shell section along the cut. These boundary conditions are difficult to realise. Another issue is that boundary affects appear near the introduction of

the load and so the region needs to be reinforced so that failure does not happen at the boundary. But adding reinforcements changes the stiffness of the specimen. Also, the boundary effects can alter the real stress and strain state quite far from the boundary. This means that a larger specimen would be needed but it compromises the advantages of sub-component testing. These difficulties means that a compromise is needed between identifying important damage modes and simplifying the sub-component testing methodology.

Also part of the study was a first attempt at performing a sub-component trailing edge test. A test rig has been developed and constructed at DTU Wind Energy for sub-component testing of trailing edge panels cut-out from full scale blades. The cut-out sections to be tested include the trailing edge panels, the shear web closest to the trailing edge and part of the caps, as shown in Figure 2.2 and Figure 2.3a. The test set-up can fit specimens of different sections of the blade but they should be 3 meters long. The loading is applied by using a spindle and the use of an actuator which forces vertical frames at each end to apply a linear varying compressive displacement on the blade piece. The compressive displacement is zero at the hinge and maximum at the trailing edge. This is meant to simulate edgewise bending on the section. The load history is monitored via a load cell. The purpose was to check the compressive strength under simplified loading which is currently more practical and realistic than applying more complicated intelligent boundary conditions.

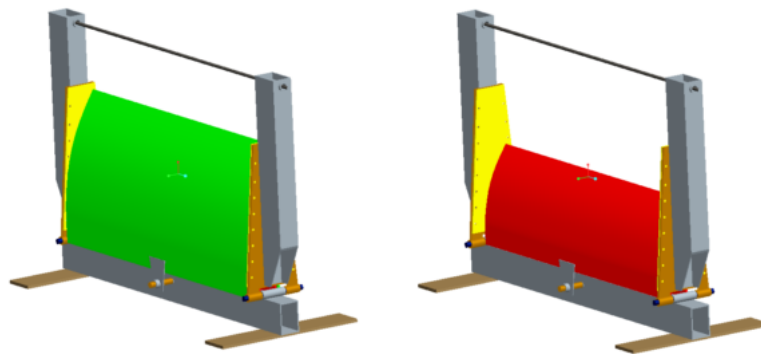


**Figure 2.2:** The test rig at DTU for testing of sub-component trailing edge panels. Blade specimens from different lengthwise blade sections can be used. [3]

One test was done on a 3m cut-out section of one of the SSP 34m blades and the test showed buckling waves similar to the ones seen on the full-scale tests. These were observed along the trailing edge. The results overall mean that the principle of the sub-component test works. However, as Figure 2.3b demonstrates, a crack initiated at one of the boundary and it clearly influenced the failure of the specimen. The conclusion is that more analysis is needed to find solutions to move the buckling more towards the middle part of the specimen. This is precisely the aim of the present research project and is a direct continuation of the study done by DTU. The following sections aim to provide in-depth information on buckling analysis.

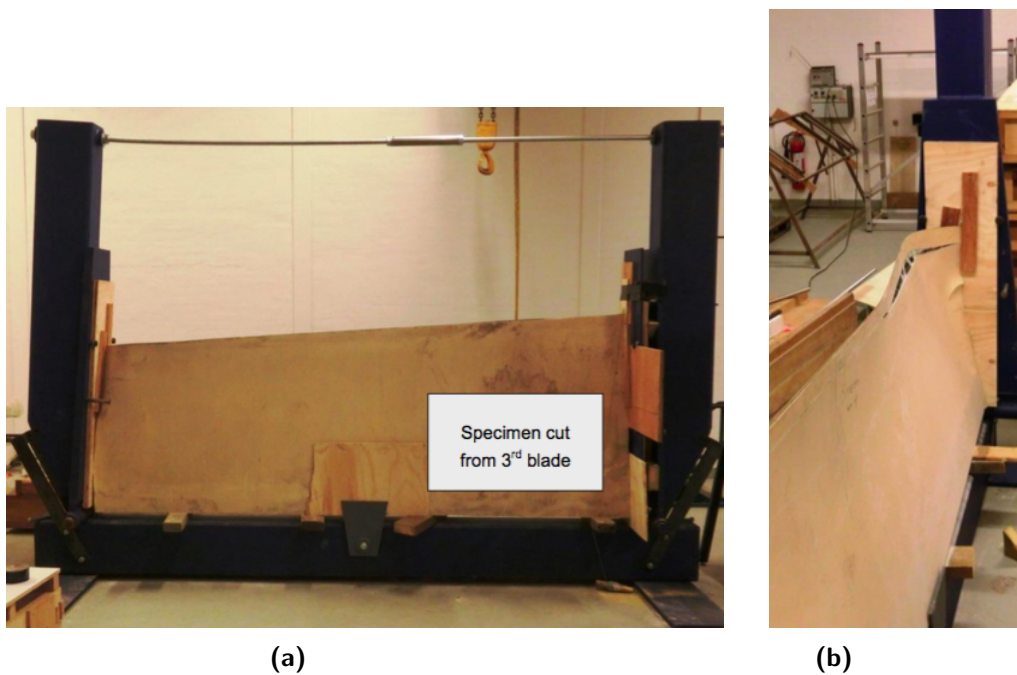


**Figure 2.3:** (a) A trailing edge specimen cut from an SSP 34m blade installed in the test rig, section from 26 to 29 meters along the blade length. (b) Buckling and failure of the trailing edge during the first test. [3]

## 2.2 Buckling: Concept and Definition

Buckling describes an instability applicable to thin structures that is defined by a nonlinear increase in out of plane deflection with a change in compressive load [4]. It happens when a structure converts membrane strain energy to bending strain energy at a given load [7]. It leads to failure at a compressive stress that is lower than the ultimate compressive stresses that the material can withstand and so buckling is the dominant failure mode of thin structures under compressive loading. This phenomenon involves important changes in the shape of the structure with geometric nonlinear effects.

An important keyword in the definition of buckling is the word instability. According to [8], “structural stability can be informally defined as the power to recover equilibrium”. Thus, a structure is deemed to be stable at an equilibrium position if it is able to return to that position after being disturbed by a perturbation. Mathematically speaking, the transition from stability to instability happens at critical points. When these critical points are reached, the structure might collapse, depending on post-critical behaviors. There exist two types of critical points; bifurcation points and limit points. These conveniently corresponds to the two different forms of buckling observed which are bifurcation buckling (also known as Euler buckling) and limit point buckling (also known as snap-through buckling).

The concepts mentioned can be well illustrated on load vs. end-displacement graphs (see Figure 2.4a, for example). On these graphs, the curves represent the equilibrium paths. The section of the equilibrium path prior to reaching a critical point is called the

primary path (or prebuckling state) while the equilibrium path after the reaching the critical point is called the secondary path (or post-buckling state). Additionally, the term reference state is used to express the state of zero deflection and zero load.

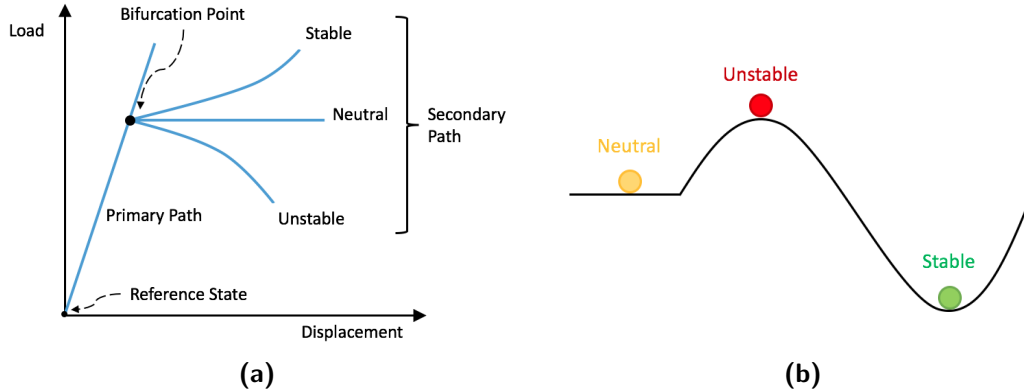


**Figure 2.4:** (a) Bifurcation buckling and its post-buckling behavior. (b) Ball analogy showing that equilibrium does not imply stability.

Bifurcation buckling comes from the word bifurcation which means that there is more than one solution possible. In effect, equilibrium is satisfied by more than one solution at this critical point, hence it coincides with the intersection of multiple equilibrium paths. Figure 2.4a shows that while increasing the applied load initially induces mainly axial or in-plane deformation, a new mode of out of plane bending deformation occurs at the bifurcation point. This can result in three types of post-buckling behaviors, unstable, neutral and stable post-buckling. Unstable post-buckling behavior comes from brittle materials and is characterized by large deflections suddenly developed with no increase in applied load. Neutral post-buckling behavior comes from plastic type failure and large deflections occurs with small increase in load. Finally, stable post-buckling behavior is common for ductile type of failure where the out-of-plane deflection develops gradually in a stable manner as the load is further increased [9]. Thus, the structure may still bear additional load in a post-buckling state given that it is stable. While more than one branch satisfies equilibrium, the structure will have to select one path and it will do so based on the one where energy is minimized. A common analogy used to represent this concept are balls tending towards points of lower potential energy when acted by gravity, as shown in Figure 2.4b. It is also important to note that the load that is applied when the bifurcation point is reached (i.e the critical load) is the solution of an eigenvalue problem where the elastic buckling load is the eigenvalue and the corresponding buckling mode deformation is the eigenvector [10]. This concept is explained in more details in the section on numerical analysis of buckling. Finally, structural engineers commonly refer to bifurcation buckling simply as buckling.

Limit point buckling occurs when the the stiffness of the structure decreases with increasing load until the stiffness eventually reaches zero (i.e the stiffness matrix becomes singular) at a certain load called the limit load (Figure 2.5b). This critical point is therefore at the local maxima on the load-displacement curve since the slope is zero at this location. Thus, very large displacements can occur with no increase in load. Failure of the structure is usually dramatic and almost instantaneous therefore indicating the collapse

of the structure [7]. For arches, caps and cones, or even a simple two-bar truss as shown in Figure 2.5a, this highly non-linear process then typically results in an unstable dynamic process called snap-through where the structure suddenly jumps from A to B (as seen in Figure 2.5b) by following the dotted line to a new state that resembles the inverted form of the initial structure. For this reason, structural engineers commonly refer to limit point buckling as snapping.

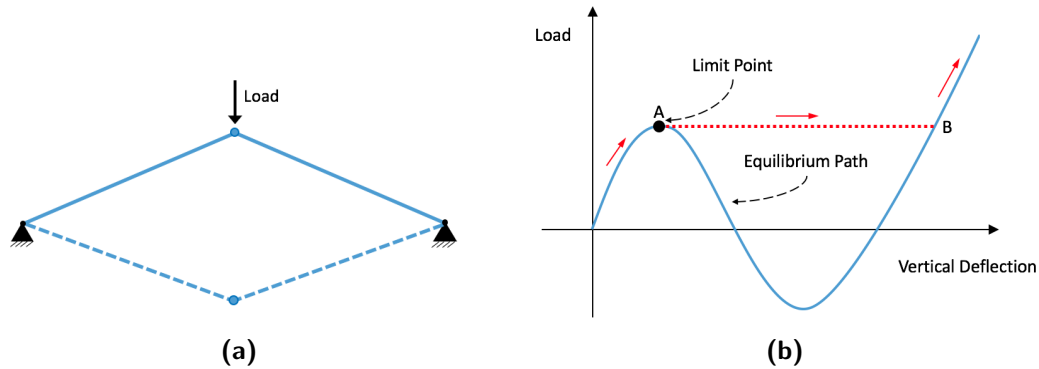


**Figure 2.5:** (a) Two bar truss, before and after snap-through. (b) Load-displacement curve of the center node showing the full equilibrium path (solid line) and real path taken from the snap-through dynamic process (dashed line)

Complex structures typically have a mixture of limit points and bifurcation points and so one question that immediately arises is: which of the critical point should be chosen to determine the safety factor against buckling? According to [8], while most textbooks simply say to pick the lowest critical load, it is not the preferred method if post-buckling behavior is also taken into consideration. This is because there could be a situation, although uncommon, in which the lowest critical load occurs at a critical point that is not the first one observed in the loading process (as illustrated in Figure 2.6b). A better method, as claimed by [8], is to select the critical load that is “located on the primary path that is nearest to the reference state”. For clarification, the primary path is the path that goes through the reference state. Therefore, the critical load to select is the load corresponding to the bifurcation point of Figure 2.6a, and of the limit point of Figure 2.6b.

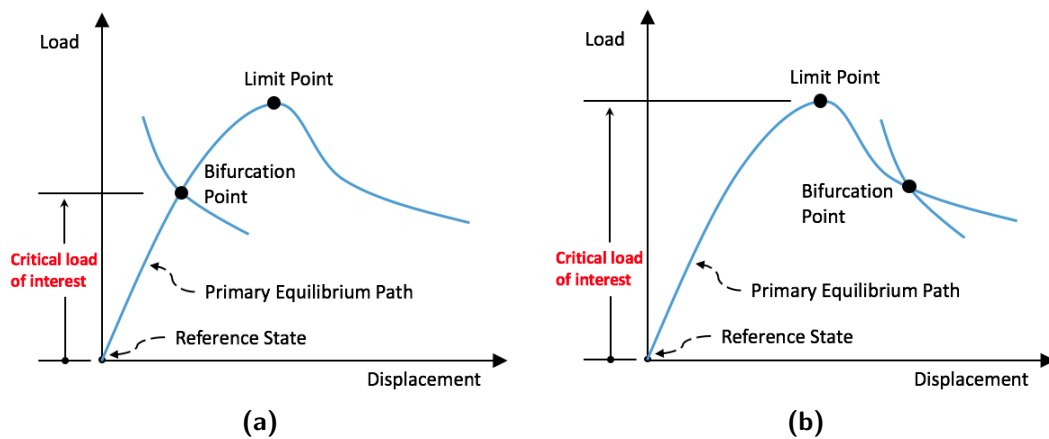


**Figure 2.6:** (a) Equilibrium path where bifurcation buckling occurs before limit-point buckling (b) Equilibrium path where limit point buckling occurs before bifurcation buckling.

An extremely important point to understand is that bifurcation is a mathematical concept and, although useful, differ from what is seen in practice. True bifurcation buckling does not actually exist because it is a feature that essentially comes from “geometrically perfect structures”, which are structures idealized as having no imperfections [10]. In real life, all structures contain unavoidable imperfections. These can be geometrical imperfections like out-of-straightness or out-of-roundness coming from manufacturing, load imperfection since the compressive load cannot be perfectly centered and support imperfections like connection eccentricities and moving foundations. These cause the real structure to follow a different fundamental path where the instability arises by limit-point buckling and in which the critical load is lower than for the ideal case (see Figure 2.7). In fact, it follows the bifurcation path as an asymptote, with greater imperfection leading to lower critical loads [11]. In summary, the structure already contains imperfections and so the structure will simply amplify these initial imperfections when loaded therefore decreasing the stiffness and following the limit load curve instead of a sharp sudden change as predicted by bifurcation theory. Although true bifurcation buckling is not real, the bifurcation model is still very useful because it often leads to a good approximation of the failure load and mode [7].

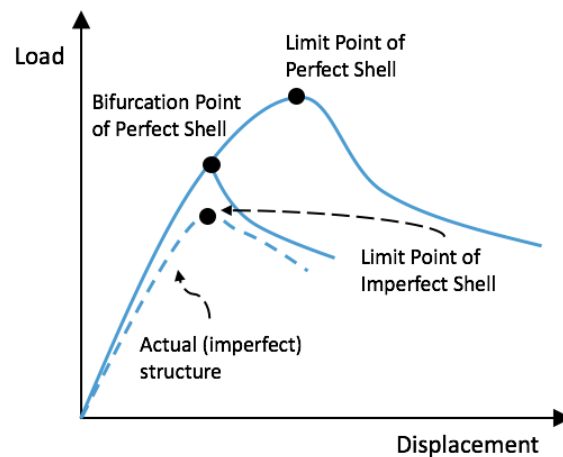


**Figure 2.7:** Load-displacement diagram showing equilibrium paths for idealized perfect structures and real imperfect structures.

Buckling may occur in different scales. When buckling is said to occur at the global level, the deformation occurs for either the entire structure, or for a complete structural member. When it occurs at the local level, the deformation is prescribed at only a specific region of the member (e.g. local buckling of an I-beam flange) [9].

Finally, buckling may trigger other failure modes in composites like fibre failure, matrix cracking or adhesive bond failure. The presence of damage in the composite or the adhesive may also affect the buckling behavior significantly. As an example, buckling in wind turbine blades can occur from what is known as buckling-driven delamination. It is a progressive failure mechanism in composite plates which arises from delamination (i.e areas of poor or no bonding between plies) already present in the structure [12]. This delamination effectively splits the structure into two sub-laminates and the critical buckling load of these sub-laminates may be much lower than the critical buckling load of the original structure. Buckling may therefore occur much earlier than expected.

## 2.3 Buckling Numerical Analysis

Buckling analysis can be modeled quite effectively in finite-element software. Two types of analysis are generally performed; a linear eigenvalue buckling analysis and nonlinear static analysis.

One limitation of buckling analysis using finite-element analysis (FEA) is the inherent use of geometrically perfect structures (unless imperfections are added manually in the case of the nonlinear static analysis). The supports are also modelled as being perfect. This means that if the structure is also symmetric (the loading therefore being centered everywhere and thus not being a source of imperfection), in theory buckling will only be triggered if a geometrical imperfection or trigger load is implemented. While theory states that no buckling would take place under this ideal condition free of imperfections, buckling will in fact still happen in the FEA model but from discretization errors. A more thorough explanation of each analysis type now follows.

### 2.3.1 Linear Eigenvalue Buckling Analysis

The easiest way to carry out a buckling analysis numerically is by doing a linear eigenvalue buckling analysis. This analysis is used to compute the bifurcation load by solving an eigenvalue problem. The eigenvalue is the bifurcation load while the eigenvector is the mode shape. This is often the first and at times the only analysis done because the structural engineer might only be interested in ensuring the safety against attaining the buckling load. It is important, however, to understand the limitations of this method which are [13] [14] [15]:

1. It only considers the undeformed structure in the analysis and so it assumes small geometric changes and linear elastic material response in the prebuckling region (i.e stiff structure). Some structures show significant non-linearity before buckling occurs and so this assumptions is not always appropriate.
2. It does not take into account the imperfections present in real structures. The theoretical buckling load from this approach may therefore be significantly higher than what would be found in practice.
3. It does not show any post-buckling behavior. It can therefore not be known whether the structure will collapse or retain its load-bearing capacity.
4. Only the buckling shape is outputted, not the actual deformation magnitude.

The way this analysis works is by a linear perturbation, meaning that set of loads are applied until a wanted state occurs. The desired state is buckling and this happens when the stiffness matrix becomes singular. According to [16], the formulation works as follows. The buckling loads, which we call  $\mathbf{P}_c$ , is a multiplication of the applied set of loads,  $\mathbf{P}_0$ , with by a scalar multiplier,  $\lambda$ , which is called the critical load factor. The equation is then  $\mathbf{P}_c = \lambda\mathbf{P}_0$ . The total stiffness matrix of the geometrically nonlinear problem,  $\mathbf{K}$ , is expressed as:

$$\mathbf{K} = \mathbf{K}_L + \mathbf{K}_{NL}(\mathbf{P}) \quad (2.1)$$

where  $\mathbf{K}_L$  is the ordinary stiffness matrix from the linear problem and  $\mathbf{K}_{NL}$  is the non-linear stiffness matrix addition which is dependent on the load.

For the linear approximation,  $\mathbf{K}_{NL}$  is proportional to the load, meaning that:

$$\mathbf{K} = \mathbf{K}_L + \lambda\mathbf{K}_{NL}(\mathbf{P}_0) \quad (2.2)$$

The singularity of the stiffness matrix occurs when its determinant is zero. Therefore, this forms the eigenvalue problem:

$$(\mathbf{K}_L + \lambda\mathbf{K}_{NL}(\mathbf{P}_0))\mathbf{u} = 0 \quad (2.3)$$

where the lowest eigenvalue,  $\lambda$ , is the critical load factor, and  $\mathbf{u}$  is the corresponding eigenmode showing the buckling shape. The user can also select to output any number of modes as higher order modes might also be of interest. Sometimes, negative eigenvalue are reported and this simply means that the structure would buckle if it was loaded in the opposite direction. In general, the linear eigenvalue buckling approach is very similar to a modal analysis which calculates the natural frequency and gives the modal shapes, but the actual magnitude of displacements.

### 2.3.2 Nonlinear Static Analysis

The nonlinear static analysis is a much more elaborate and accurate method for predicting the buckling behavior. While the linear buckling analysis could only predict, in a nonconservative way, the bifurcation load and buckling shape, the nonlinear static analysis predicts the complete prebuckling and postbuckling behavior of the structure. This means that the displacement magnitude and stresses is fully computed during its load-displacement response (i.e its equilibrium path) even when the structure shows a negative stiffness (i.e past the limit point). While being much more computationally intensive, it does not have the limitations of the linear eigenvalue buckling analysis. In summary, its advantages are as follows [13] [14] [15]:

1. As opposed to the linear analysis, it is able to capture the geometric and material nonlinearity seen in most structures during the prebuckling and postbuckling phases.
2. It can take into account the imperfections present in real structures (after they have been manually entered). It therefore allows to investigate imperfection sensitivity, which is extremely important. The theoretical buckling load from this approach may therefore also be much closer to what is seen in practice as compared with the linear buckling analysis.
3. It captures the full post-buckling behavior. It therefore allows to predict whether the structure will collapse or retain its load-bearing capacity.
4. The full nodal displacement history is outputted at the correct magnitude. This means that it also outputs the full stress and strain history.

The nonlinear analysis works by gradually applying the load in multiple steps as opposed to a linear analysis in which the load is applied in one step. At each load increment, the structure changes shape and this then changes the stiffness matrix. The stiffness matrix is therefore updated at each increment. An iterative process is also performed at each increment in order to find the equilibrium solution, which is a balance between the internal forces in the structure and the external forces applied to the structure. The iteration terminates when the difference in forces, called the residual, fall below a small prescribed value such that the solution is deemed to have converged. The full non-linear displacement path is then recovered.

Two different nonlinear algorithms are typically used to perform this analysis. The most common general nonlinear solver is the Newton-Raphson method shown in Figure 2.8a. The procedure essentially follows what was explained in the previous paragraph with the additional specification that the load increment is constant. While this algorithm is generally quite effective, it diverges near limit points due to the stiffness matrix becoming ill-conditioned (i.e becomes zero) or from the load step being greater than the limit load. This limitation led to the development of the arc-length algorithm (known as the Riks method in Abaqus). This method is similar to the Newton-Raphson method, the main difference being that in addition to the displacements, the load level also varies during the iterations. This is in effect regulated by an arc constraint that is centered at the last solution point and it has the effect of making the load level decrease slightly with each

iteration. This is clearly seen in Figure 2.8b which shows the iterative process that is part of one increment. It should first be noted that in this example, the arc radius  $\Delta L$  (which is a predefined value and essentially acts as a load increment) has been made unreasonably large in order to show the capability of the algorithm to recover the equilibrium path past a limit point. The iteration works as follows: The stiffness matrix of the last solution point, called point 1, is used in the first iteration to compute the displacement at point A which is when the path crosses the arc. Equilibrium is out of balance and so a new iteration is performed starting at point a and by using the updated stiffness matrix the displacement at point B is found. Unlike the Newton-Raphson method, this corresponds to a load level that is lower than point A. This iterative process continues up until finding the equilibrium solution called point 2. The full equilibrium path would be recovered by using a sufficiently small arc radius. The arc-length algorithm is therefore the preferred method for nonlinear buckling analysis in which negative stiffness or snap-through might be present. More thorough information on nonlinear numerical methods can be found in [17] and [18].

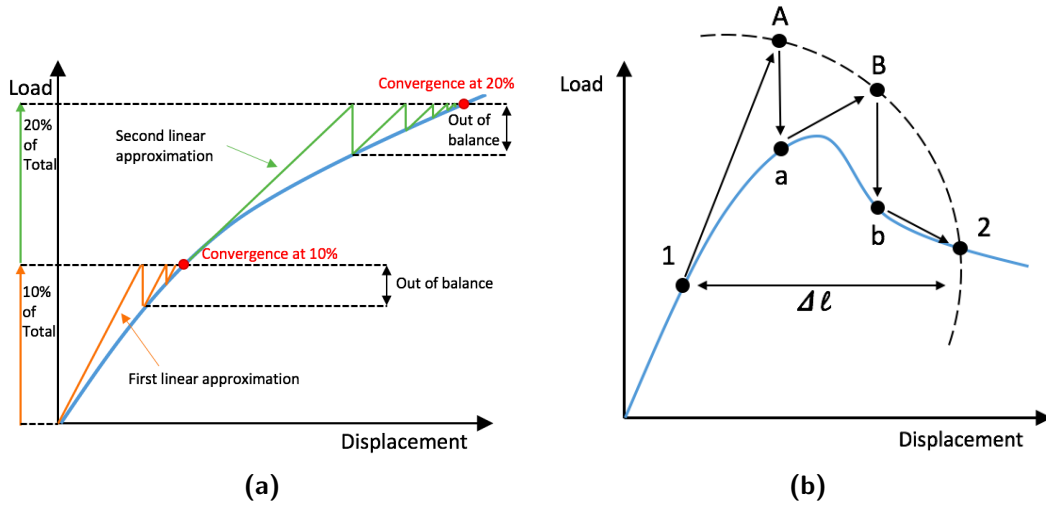


Figure 2.8: (a) The Newton-Raphson method. (b) The arc-length method.

### 2.3.3 Dynamic Implicit Analysis

The dynamic implicit solver is another analysis type that can be used to solve nonlinear problems such as buckling. It has the potential of performing better than the nonlinear static analysis if complicated interactions are present in the model, such as contacts. This type of analysis can be used for dynamic problems or quasi-static problems. Quasi-static means that dynamic effects do not appear or can be neglected [19]. If the dynamic solver is used for a buckling problem, then it would be modeled as quasi-static since the loading on the structure is applied slowly (i.e it does not involve any impact). To ensure that dynamic effects are small enough such that a quasi-static state is observed, the kinematic energy should be verified to be less than 5 % of the strain energy [19].

While a static structural analysis follows the system of equation,

$$KD = R \quad (2.4)$$

where  $K$  is the global stiffness matrix,  $D$  is the displacement vector of all nodes and  $R$  is the nodal force vector, the dynamic formulation follows the second-order time-dependent differential equation:

$$KD_n + C\dot{D}_n + M\ddot{D}_n = R_n \quad (2.5)$$

where,

$R_n$  = Known time-dependent forcing function

$D$  = Displacement

$\dot{D}$  = Velocity

$\ddot{D}$  = Acceleration

$K$  = Stiffness

$C$  = Damping

$M$  = Mass

For a quasi-static simulation, the velocity and acceleration terms are extremely small, therefore making the formulation look "almost" static. The very small velocity term is quite important, however, because the term  $C\dot{D}_n$  provides the slight damping that helps maintain solution equilibrium and thus makes this solver more robust than the static solver in solving highly nonlinear problems.

## 2.4 Buckling Analysis of Wind Turbine Blades

Buckling is a structural nonlinear instability that is very important to consider during the design of wind turbine blades [12]. In fact, while static failure of a wind turbine blade typically arises from exceeding the material strength or buckling of the structure, buckling is often the critical parameter [2]. This failure mode arises primarily from the fact that wind turbine blade cross-sections are made of thin shells, in order to minimize material use to achieve lightweight cost-effective structures, and are subjected to large flap-wise bending moments [20]. While buckling of the surface panels near the blade root are particularly prone to this instability, the trailing edge of the blades must also be checked since this region is very sensitive to stability effects which are caused by small geometrical imperfections [21]. These arise from manufacturing deviations such as fibre misalignment or trailing edge shape. Secondly, this region must now especially be checked for buckling since blades have increased in size considerably in recent years, therefore increasing the edgewise fatigue loads induced by gravity acting on the trailing edge [12].

### 2.4.1 Industry Guidelines

Industry standards are very beneficial for wind turbine blade designers as it sets a standard on the level of analysis that should be performed and lays-out detailed guidelines to follow. The information presented in these standards gives a great general overview of industry best practices with regards to buckling analysis. The main standards currently used by industry for the design of wind turbine blades are the DNV-DS-J102 standard released by the company Det Norske Veritas (DNV) in 2010 [10], the standard on offshore wind

turbines by the company Germanischer Lloyd (GL) in 2012 [22] and the newly released standard DNVGL-ST-0376 which is the first standard on wind turbine blades after the merger of the two companies DNV and GL in 2013 [5].

These standards reveal a few key points that are useful for the current research project. DNVGL-ST-0376 states that all parts of the blades shall be verified for buckling like spar caps, shells, ribs, and shear webs and that the buckling analysis may be done using two approaches, by analyzing individual components of a simple shape like beams, plates and shells, tubular sections and/or analyzing the entire structure or complex component [5]. The simple shapes could be analyzed for buckling via analytical methods, however, this method is so general that a very high partial reduction factor (e.g. a safety factor) of 1.5 shall be used [10]. The standard by GL further specifies that analytical methods shall be mainly restricted to geometrically perfect structures except for simple structural members with imperfections of simple shapes. It further states that simple analytical formulas for buckling of flat and curved orthotropic plates are useful to check whether the buckling will change the strain distribution of the blade or if the strain distribution for extreme loads necessitates more analysis [22].

When analyzing complex structures for buckling, often no closed-form equation describing the physical process exist. These complex structures, like wind turbine blades, are instead analyzed numerically via finite-element analysis (FEA). Different numerical analysis types yields different levels of uncertainty and this uncertainty is often expressed by partial safety (or reduction) factors. The greater the value, the greater the uncertainty. The partial reduction factors to use according to DNVGL-ST-0376 ranges between 1.0 and 1.4 depending on the numerical model type chosen. The factors to use are prescribed by DNV-GL as: 1.0 if the nonlinear FEA is validated by full scale tests; 1.05 if a nonlinear FEA is performed; 1.25 if a linear FEA is performed modelling the full blade; 1.4 if a linear FEA is performed analyzing selected cross sections [5]. Therefore, these certifying bodies recommend the use of nonlinear analysis for more accurate results. The nonlinearity in this case is a geometrical nonlinearity due to large displacements as opposed to material nonlinearity.

A linear analysis, which is the linear eigenvalue buckling analysis mentioned earlier, is typically the first analysis performed. The undeformed structure is used along with initial (non-degraded) laminate elastic properties. The structure is also modelled as being geometrically perfect (i.e no imperfections). The GL standard states that a mesh convergence shall be performed for the linear FEA analysis and that a sufficiently accurate mesh is obtained when the buckling eigenvalue does not change by more than 5% when the number of element is doubled [22].

A nonlinear analysis is then usually performed but with imperfections included. The addition of imperfections in the numerical model is necessary if the structure is originally modelled as being perfect and symmetric because it would not buckle otherwise. In practice, the structure can never be perfect and symmetric and so buckling occurs due to slight imperfections. According to DNV-DS-J102, it is recommended to do a study on the size and shape of the initial geometrical imperfections in order to evaluate its influence on the buckling behavior [10]. The most critical initial imperfection is typically a shape close to the first eigenmode itself and so DNVGL-ST-0376 recommends to apply the 1st linear eigenmode shape to the structure as an initial imperfection [5]. The GL standard

adds that as a general rule of thumb, the global scaling of this 1st eigenmode should make the maximum height of the global buckle to be  $1/400$  of its wavelength [22].

Another important recommendations by the standards for the nonlinear FEA analysis is to use at least 10 load increments (also known as time steps) to ensure proper results. The steps are part of typical nonlinear algorithms such as the Newton-Raphson method explained earlier.

Additionally, when analyzing the results of the nonlinear FEA, fibre failure, delamination between sandwich core and laminate, and peeling force at adhesive bonds should be checked since these failure modes can arise from the large out-of-plane deformation from buckling [5].

Finally, each of these blade standards mention to put special attention on the definition of the boundary conditions since they are known to greatly affect the results.

### 2.4.2 Buckling in Full-Scale Tests

Full-scale static testing of wind turbine blades has been performed in many research studies to investigate common failure modes, and they have provided great insights on the buckling failure of these structures. These studies are particularly helpful for the present thesis because they include both numerical and experimental work and thus valuable information can be obtained about how the results matched and which techniques were successful and which needed more work. The DTU Risø laboratory has recently tested three 34m SSP blades to static failure for a national study (Figure 2.9). A few relevant papers came out of this large study, namely Eder et al. [3], Haselbach and Branner [23], and Haselbach et al. [21]. An interesting and relatively new device called a fiber optical strain gauge was used to measure the longitudinal and transversal surface strains along the trailing edge of the whole blade and revealed buckling waves quite early in the loading process, more so than in the simulation. The failure modes observed were consistent and matched well with the numerical simulation. In all cases, the blade started forming highly nonlinear buckling waves at the trailing edge between 50-60% of the ultimate failure load. This was followed by core shear failure which reduced the stiffness in the sandwich panel and therefore led to more pronounced buckling waves. A wide variety of failure modes then appeared at the trailing edge (such as adhesive debonding as seen in Figure 2.10a) depending on the location along the blade, and this ultimately led to complete blade collapse [3] [23]. Overall, the simulation correctly predicted the blade response before failure and also correctly predicted that the failure mechanism would be core shear failure [23].

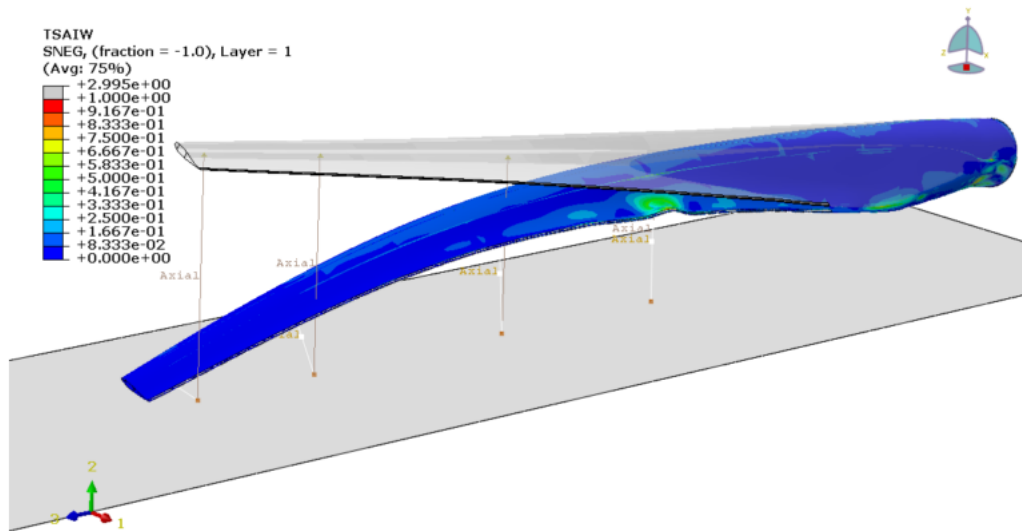


**Figure 2.9:** Model of the full-scale test experiment performed at DTU where the blade is loaded in combined flapwise and edgewise loading (-30 degrees). [3]

While the numerical and experimental work matched quite well, Haselbach and Braner [23] go in more details about the slight differences observed. They mention that while the position of the buckling wave agreed well at low load level, the buckling wave predicted from the numerical simulation moved towards the blade tip at high loads, while the opposite happened in the experiment. Additionally, the buckling wave magnitude observed in the experiment was lower than expected. The buckling of the trailing edge created a local kink on the pressure side at about 0.58 meters from the trailing edge (Figure 2.10b). This damage reduced the stiffness in the section and is said to be the reason for the difference in buckling wave amplitude. The numerical model did not include what is known as progressive damage and failure theory and so the stiffness degradation from the failed composite sandwich could not be captured. The authors mention that including stiffness degradation in the model by using Hashin's progressive damage and failure theory improved the numerical results. They further state that while it is computationally expensive, they recommend using this modelling approach in other designs to predict failure [23]. Furthermore, they state that running geometrical nonlinear simulation is paramount in revealing the trailing edge deformation and corresponding series of events because simplified linear elastic simulations will not show the full picture [23]. The progressive damage observed in this study is in line with what has been observed in similar studies such as in [24] and [25]. In these two studies the critical buckling load triggered delamination at the inflection of the buckling wave and it lead to progressive collapse of the wind turbine blade.



**Figure 2.10:** (a) Ultimate failure from debonding induced by local buckling waves [3]. (b) Trailing edge deformation before attaining the ultimate load. A kink appeared on the top surface (pressure side) [23]

Haselbach et al. [21] say that almost all the simulations were run using the Newton-Raphson solver in Abaqus with the exception of very high loads where the implicit dynamic solver was chosen instead. This was done in order to overcome convergence problems stemming from large nonlinear wave formations which made it difficult for the standard solver to reach equilibrium [21].

This study also has a different outlook on the use of imperfections in comparison with the industry standards. Eder et al. [3] mention that no imperfections were added to the model because imperfections coming from a linear eigenvalue buckling analysis can lead to arbitrary results [3]. Moreover, the researchers add that eigenmodes calculated early on during the loading process might turn out to be very different from the ones occurring near failure. This technique might also lead to wrong results of failure mode and load. Haselbach and Branner [23] also mention that buckling results are so sensitive to imperfections that a small imperfection of 1 mm was enough to move the buckling wave such that both numerical and experimental results matched perfectly [23]. Another important finding on the implementation of imperfections comes from the work of Jørgensen et al [24]. In their study, they concluded that the geometrical imperfections do not affect the buckling shape, but that the imperfection magnitude is linearly dependent with local strain measured at the peak of the buckling wave.

### 2.4.3 Buckling in Sub-Components

Sub-component testing is quite new to the wind turbine industry and no experimental work on compression of blade sections are known to be available in literature. However, a few numerical studies have been done on compression of blade sections. Investigating these studies is quite helpful for the present thesis specifically in order to understand how the boundary conditions and loading are typically implemented during compression analysis of blade sections.

Relevant studies include the work by Eder and Bitsche [26], Eder et al. [27], Haselbach et al. [28] and Gaudern and Symons [20]. Eder and Bitsche [26], and Haselbach et al. [28]

used blade sections from the DTU 10 MW reference turbine model. These sections were 11 m and 8.65 m long, respectively, and were taken at a radial distance approximately midway through the full length of the blade. On the other hand, Eder et al. [27] and Gaudern and Symons [20] used a particular cross-section and extruded it to a length of 20 m. Taper and twist was therefore assumed to be negligible.

The boundary conditions were defined in all these studies by using kinematic coupling constraints. This modeling technique links the nodes of the cross-section to a master node, thereby creating a connection analogous to a rigid plate (Figure 2.11a). The boundary conditions are then applied only to the master node and the ends move like a rigid body. According to [27], this ensures that the area of interest will not be affected by stress states coming from the applied boundary conditions.

The four studies also agree in that one of the cross-section edge is fully constrained. This means that all three displacement degrees of freedom and all three rotational degrees of freedoms are fixed. The alternate method is to use a simply-supported boundary condition which restricts displacement but allows rotation. Both [28] and [20] suggest that simply-supported boundary conditions are better suited for buckling analysis of either flat or curved panels, a methodology that is often used to represent the blade panels in the initial design phase.

While the load was applied at the other cross-section edge on the master node in each studies, the type of compressive load applied differed slightly. Eder and Bitsche [26] applied a pure bending moment incrementally at 210 degrees from the global x axis of their model, corresponding to a combined flapwise and edgewise bending [26]. This induced a predominantly compressive strain on the suction side shell. A snapshot of their model which includes both their buckling result and the loading axis is shown in Figure 2.11b. Haselbach et al. [28] produced a similar outcome but by instead apply three moments of different magnitude instead of changing the axis angle at which one resultant moment is applied. Note that an important difference is the inclusion of a slight torsional moment in addition to the bending moments. Thus, the three moments,  $M_x = -16.4e6 \text{ Nm}$ ,  $M_y = 2.4e6 \text{ Nm}$  and  $M_z = 0.32e6 \text{ Nm}$  were applied at the master node located at the cross-section center, such that it would be a realistic design load under normal operation (e.g dominated by flapwise bending) [28]. The other two studies considered more than one load case. In Eder et al. [27] the applied cross-sectional load came from the aerolastic simulation of the National Renewable Energy Laboratory (NREL) 5MW turbine using the aeroelastic simulation software HAWC2. The maximum absolute value from the time history was used for 5 different load cases applied at the master node located at the shear center. The loads considered were a) concentrated load in the chord direction (edgewise shear) b) concentrated load perpendicular to chord direction (flapwise shear), d) pure edgewise bending moment d) pure flapwise bending moment and e) torsional moment [27]. Meanwhile, Gaudern and Symons [20] applied three different load cases. The first one was a pure flapwise moment loaded at the master node specifically located at the leading edge tip. This gave a uniform moment and thus uniform compression on side of the blade surface panel, over the blade length. The second load case was a concentrated force in the flapwise direction again applied at the leading edge tip. This generated a linearly-varying moment. Finally, a uniformly-distributed load was applied on the whole length of the blade to give a quadratic moment distribution, aimed to mimic storm loading in parked conditions. The load distribution used was found to significantly

affect the buckling results [20].

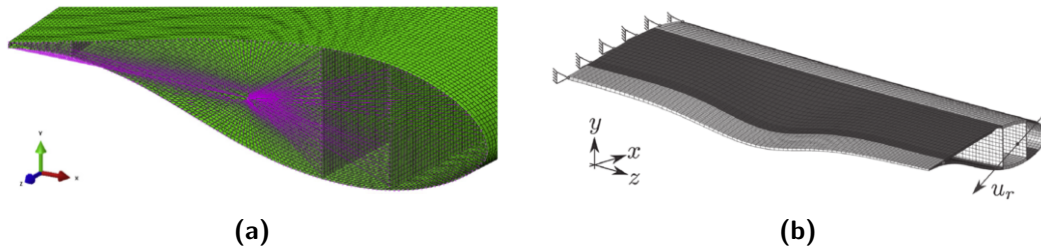


**Figure 2.11:** (a) Kinematic coupling constraint from [28] (b) Blade section model from [26] demonstrating local buckling wave along with the boundary conditions applied. The arrow shows the axis about which the pure bending moment was applied.

In terms of the type of analysis performed, Eder and Bitsche [26] followed the buckling analysis guidelines from the standards in which a linear eigenvalue buckling analysis is performed and the eigenmode is then added as imperfection to a nonlinear static analysis. The imperfection was scaled such that its maximum height was 5 mm [26]. They used a dynamic analysis (with inertia effects) with implicit time integration instead of the standard Newton-Raphson method to prevent convergence issues. However, they mention that the loads were applied so slowly that inertia effects had negligible influence on the results and hence the same results would have been obtained from standard static procedure [26]. Gaudern and Symons only performed a linear eigenvalue buckling analysis, and outputted the first mode only [20], while Haselbach et al. only performed a quasi-static nonlinear analysis using the Abaqus/explicit solver with a time integration [28]. This was chosen for its efficiency in solving large models and its suitability for the particular model containing cohesive elements which are elements used in fracture analysis. Finally, Eder et al. [27] performed an entirely different analysis based on fracture mechanics.

## 2.5 Buckling Analysis of Aerospace Structures

By far the most widely extensive source of information on buckling experiment and analysis of sub-components comes from the aerospace industry. The most common sub-component structures tested in this industry are stiffened panels, cylinders (tubes) or beams (channels). These have been traditionally made out of steel or aluminum but recent focus has been put on composite materials for their superior properties like high specific strength and stiffness. The most direct benefit in investigating these studies for the current thesis is to get an overview of not only numerical but also experimental methods and outcomes on buckling analysis of sub-components. Specific information sought that were not available from the literature search on buckling of full-scale blades and of blade sub-components are for example, how the boundary conditions have been applied and what approaches have been done to resolve boundary effects if any, what measuring devices are typically used and finally which results are typically measured and compared with the numerical results. Over 30 research papers were analyzed.

The predominant method in applying the boundary conditions to the sub-component has been found to be with the use of grips or specifically designed fixtures [29] [30] [31] [32] [33]

[34] [35]. This imposes fixed boundary conditions. In a few of these studies, the ends are strengthened for a certain distance on the structure such as the grips in [32] designed to prevent local stress concentrations and the panel end tabs used in [33] (See Figure 2.12a). Moreover, a similar outcome has been done by an interesting capping system designed and used in [34] for a buckling analysis of columns (Figure 2.12b). The column ends were put in an unsaturated polyester resin which has the advantage to harden rapidly, have high strength and has high energy absorption. A similar resin is used in [36]. Overall, the studies demonstrated that boundary effects has not been seen to be problematic. The experiments carried out successfully with the buckling waves occurring away from the boundaries. It is believed that the main reason for this outcome is due to the sub-component structures having a relatively simple geometry and being highly symmetric.

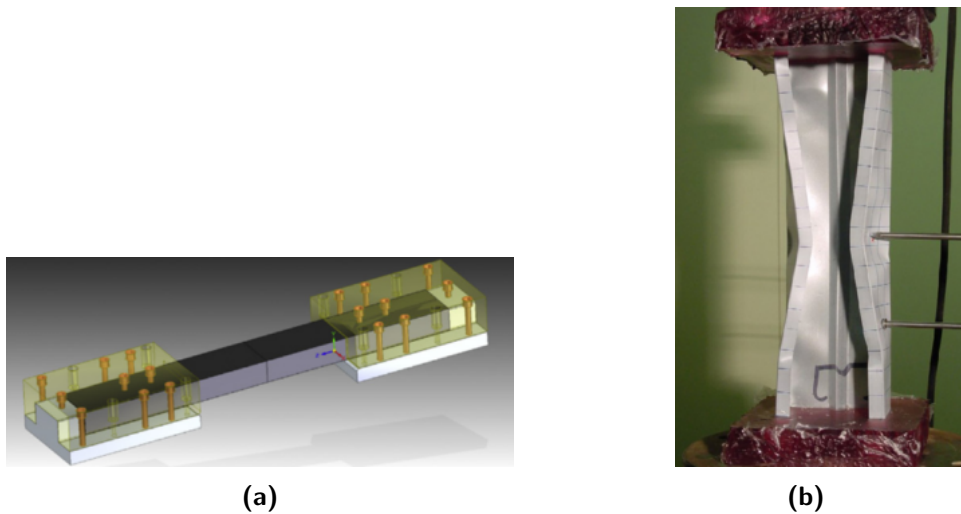


**Figure 2.12:** (a) Grips designed and manufactured in [32] (b) Capping made out of unsaturated polyester resin [34].

The typical measuring devices used for the buckling analysis of sub-components are (as seen in the above references): 3D optical measurement system, like Digital Image Correlation (DIC), which are used to measure out-of-plane displacement fields and therefore buckling shapes. Thorough explanation of how DIC works can be found in [35]; local strain gauges, which are placed in regions of interest (buckling wave) as predicted from the numerical simulations; ultrasonic scans, which are often performed to get the initial imperfections and then imported in the numerical model; and a load cell, to measure the load history.

The most common results that are measured and used for validation with numerical simulations are: out-of-plane displacement and longitudinal strain fields from DIC, in a color map format. This makes it easy to compare with the numerical results. It is often shown at the buckling load; local strain in selected regions where high strain is predicted. It is mainly used to verify loading and for validation purposes; load vs. axial displacement graph (i.e end shortening); and buckling load.

It is also found that the common procedure for the numerical simulation is to perform a linear eigenvalue buckling analysis and output a linear combination of eigenmodes dis-

placements in a nonlinear static analysis, like was explained in the wind turbine standards. The study also revealed the occasional use of the Riks method which is an alternate nonlinear solver available in Abaqus.

## 2.6 Final Remarks

The knowledge gathered from this literature review provides a great starting point on how to perform the numerical analysis, but also key practical aspects to look for on the experimental side of the project. This knowledge will be directly applied to the thesis project on how to perform the numerical modeling of the trailing edge section in order to then investigate how to best solve the boundary effects and accurate load introduction on the sub-component. The research project will clearly add to this body of knowledge since a study including both numerical and experimental compression testing of a cut-out trailing edge section of a wind turbine blade has not been done before.

The recommended analysis type for the research project, according to the standards and past studies, is a linear eigenvalue buckling analysis followed by a nonlinear static analysis. According to the study, the Riks method is preferred over the Newton-Raphson for the nonlinear analysis. The literature suggests to be very careful with how imperfections are included and so a short study on imperfections will be carried out. Moreover, it is important to understand that due to the asymmetry present in the blade sections, the addition of imperfections is not required for the simulation to run successfully. The other analysis type such as the implicit dynamic solver will also be investigated. This can help confirm that the results are not too sensitive from the analysis type chosen. It is clear that Hashin's progressive damage and failure theory can radically improve the results and so the use of this analysis will be considered. Kinematic coupling constraints also appear to be quite a common approach in defining the boundary conditions and this method will be considered as well. The current blade section modelled is different from many of these studies on plates and big takeaway is to use fixed boundary conditions for the blade structure as opposed to simple-supports.

In terms of the loading types, it is interesting to see that many researchers have different takes on what are realistic loading situations. The research project only considers pure edgewise bending for simplicity reason but it would be interesting to carry the experiment further by loading the blade section in a combined flapwise and edgewise bending, such as to potentially mimic the loading seen by the blade during operation more closely.

Finally, another big finding was how boundary effects was not found to be quite a large problem as initially believed on the survey of buckling analysis in aerospace structures. It is likely to be due to the fact that these structures have a simple geometry and are perfectly symmetric. Therefore, cutting the blade section such that it becomes more symmetric could be effective in mitigating the boundary condition effects. The use of resin to strengthen the ends of the structure was also quite interesting and its suitability for the thesis project will be assessed.

## 2.7 Research Questions, Objective and Sub-Goals

The research questions for this project are divided into a main research question followed by multiple sub-questions which will provide answers that will help answering the main question. The research questions are as follows:

Main research question: *What is the best solution or set of solutions for moving the buckling wave towards the center of trailing edge sub-component specimens so as to solve boundary effect problems while keeping a load distribution that is representative of what is seen in the trailing edge region of full-scale blade when this region is under compression.*

Research sub-questions:

1. Which modeling methods and settings are recommended for successfully simulating the buckling test?
2. How well can the sub-component set-up mimic the load distribution acting on the trailing edge region of full-scale blades? What arrangement should be taken to ensure a good match?
3. How does the buckling response vary between blade sections from different radial locations?
4. What makes the buckling wave occur near the section boundary? Or in a more general sense, what are the main factors that determine where the buckling wave will be located?

The objective of the research project is to make a recommendation on how to improve sub-component testing methods used to determine the buckling behavior at the trailing edge by analyzing different solutions with the help of numerical and experimental methods. More precisely, the aim is to mitigate boundary condition effects during static compression loading such that the loading of the blade piece from testing correctly mimics the condition seen by the blade in full-size testing and in the field (i.e blade failure should not start at the boundaries). Sub-goals falling under this objective are:

1. Gain background knowledge on relevant subjects like testing procedures, certification, sub-component testing, trailing edge failure, buckling, and boundary condition effects and solutions (Chapter 2).
2. Learn to use the finite-element software Abaqus with focus on buckling analysis, and simulation of fibre-reinforced composites.
3. Become familiar with the full-scale blade model.
4. Using Abaqus, create a sub-component model of the section that was first tested (namely between 26 m and 29 m of the full-blade) from the full-scale model. Model the test-set up and perform a buckling analysis on the cut-out specimen. Compare the results with the experimental test to validate the numerical model (Chapter 3).
5. Simulate the full-scale blade such that the trailing edge is under compressive loading to get an idea of the strain distribution in this region (Chapter 4).

6. Implement this loading condition on the three blade sections that DTU has (Chapter 5) and perform buckling tests using the model and methods previously devised (Chapter 6). See how the results vary between the sections.
7. Try to understand what makes the wave buckle in specific locations (Chapter 7).
8. Use this knowledge to implement different solutions to shift the buckling wave towards the center of the blade section. Try to maintain a strain distribution that resembles the one seen in full-scale tests. Evaluate which solutions are most promising and provide a recommendation (Chapter 8).
9. If time allows:
  - (a) Apply the solution(s) to actual sub-component tests using the DTU test rig.
  - (b) Evaluate the results and see how well the numerical results match the experimental results.
  - (c) Assess whether a solution or a combination of solutions successfully solve(s) the b.c. problem.



# Validation of Numerical Model with Previous Experiment

Before investigating the outcome of different solutions in addressing the boundary effect problems in the sub-component test, it is first necessary to create a numerical model representing the sub-component test. It is also very important to validate the model in order to ensure that its results closely represent what is seen in practice. Fortunately, as mentioned at the end of Section 2.1, a test rig was built at DTU and a first sub-component test was performed. The experiment can therefore be replicated numerically in order to validate the model. Once the numerical model is validated, different studies can be done on this model to predict solutions that can later be applied to future experiments.

The chapter starts by covering important details of the first experiment that was conducted and describes the test set-up thoroughly. The numerical model assumptions and different modelling approaches are subsequently covered. The results are then presented and analyzed. The chapter ends with two short studies that were performed. The first one is about analyzing the effect of implementing geometrical imperfections in the model while the second one looks at the effect of changing the angle that the blade is loaded in the set-up.

### 3.1 Test Specifications

While Section 2.1 described the general test procedure, this section deals with specific information regarding the test setup.

The blade section tested originates from one of the three 34 m SSP blades that were tested to failure by DTU. The particular section comes from a region of the blade relatively close to the tip, as shown in Figure 3.1, far from where the blades collapsed, which was at around 14 m down the blade from the root [3]). While no damage of the blade piece is apparent from visual inspection, it is still important to note that it is in a "used" state to start with. The blade section is said to be 3 m long, ranging from blade radius of approximately 26 m

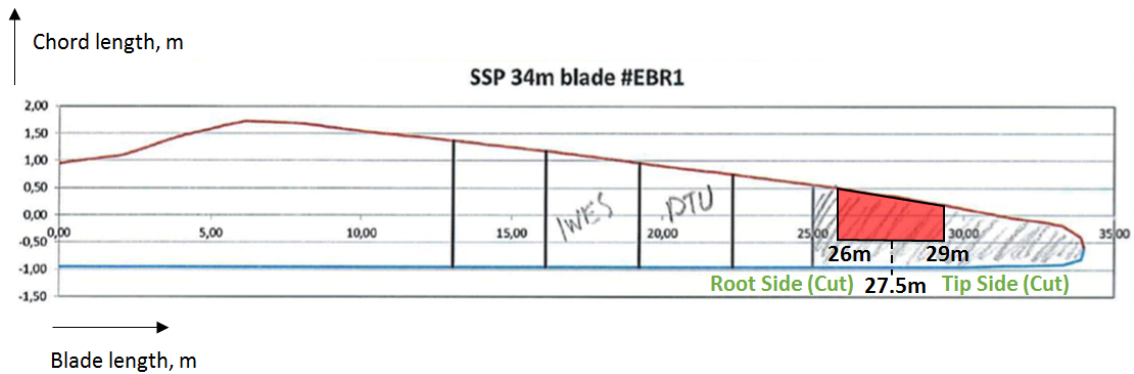


**Figure 3.1:** Profile of the SSP 34 m blade. The blade section used in the first experiment is highlighted in red.

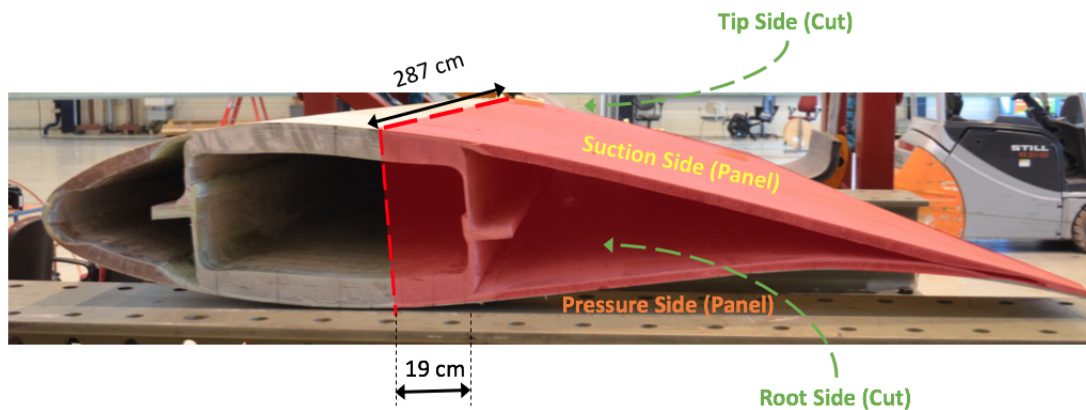


**Figure 3.2:** Cross-section of the SSP 34 m blade. The blade section used in the first experiment is highlighted in red.

to 29 m and includes the first shear web (See Figure 3.2). This section will be referred to as the 27.5 section.

The blade section was hand cut and so cutting errors have to be considered as a source of error. Manual measurement of the blade confirms that the blade is slightly shorter than 3 m, at 287 cm. Furthermore, measurements showed that the cut is located 19 cm past the shear web on the root side and 17.5 cm on the tip side.

The test rig was built according to the technical drawings shown in Figure 3.3. The plates are forced towards each other by means of a spindle, 2 m above the hinges (Figure 3.4a). Since the blade section was cut slightly shorter than anticipated, extra wood plies were placed between the blade and the steel columns. This left a distance of 12.5 cm between the steel columns (right above the hinges) and the blade edges (Figure 3.4c). Wooden plies were placed around the trailing edge to ensure that the piece would not move sideways (Figure 3.4d). A dent can also be seen in the back wooden ply from when the blade was loaded in compression. Figure 3.4d also shows that the blade section was oriented such that its trailing edge tip is aligned with the load (i.e. at the center of the column). Two steel pieces were placed at the bottom middle section on both sides of the blade sub-component to limit large sideways displacement. The blade was also laid on

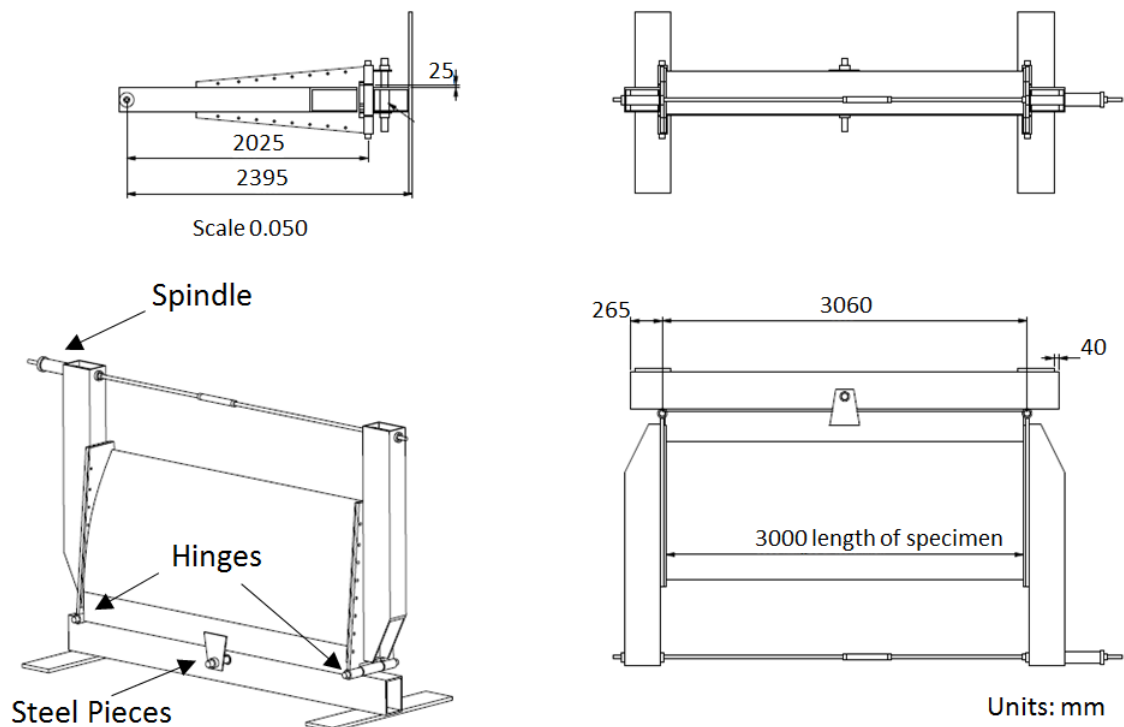


**Figure 3.3:** Detailed drawings of the test rig built at DTU. Drawn by Peter Berring from DTU Wind Energy.

top of wooden blocks. This was helpful in orienting the blade at the proper angle. The steel pieces and wood blocks can be seen in Figure 3.4a.

When the blade was loaded a pronounced local buckling wave developed near the edge of the section on the tip side (i.e the side with the smaller cross-section) as shown in Figure 3.5. A crack started developing at the boundary on the tip side and grew to the size shown in Figure 3.4b. The location of the crack is 10 cm below the trailing edge, which is right below the adhesive bondline. This region turns out to be the thinnest part of the cross-section and so it makes sense that a crack would form there. It also makes sense that the buckling and crack formed on the tip side as opposed to the root side because the cross-sectional area of the tip side is smaller and so the load is more concentrated in this region. The stress is therefore higher in this local region. Another alternate way to think about it is the fact that the internal resisting bending moment of the blade on the tip side is lower than on the root side due to the smaller cross-sectional and so it fails first given an equal externally applied moment.

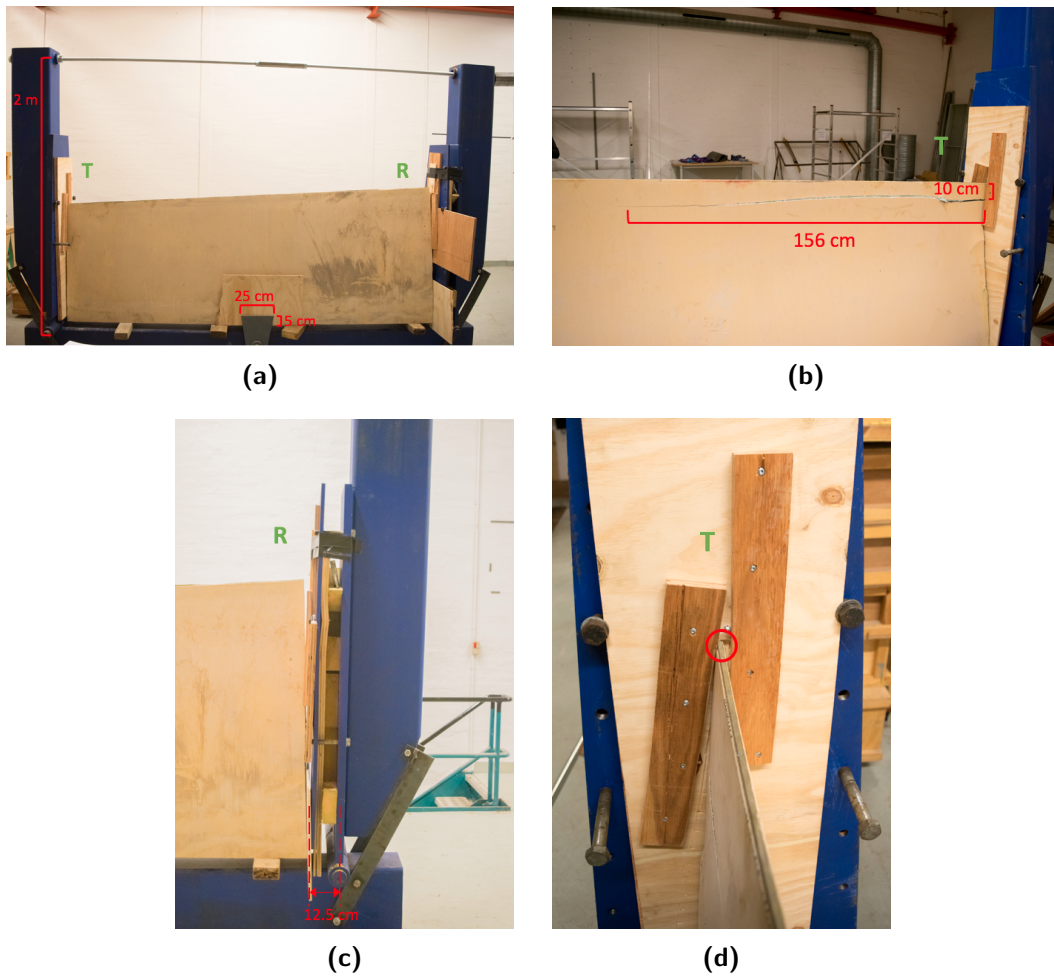


**Figure 3.4:** a) Complete test rig. b) Crack that initiated at the boundary of the pressure side. c) Gap between blade end and hinge. d) Support near the blade tip and dent created during compression (circled). Note: T stands for tip side and R for root side.



**Figure 3.5:** Figure 2.3b included here for convenience. Buckling and failure of the trailing edge during the first test. [3]

Unfortunately, no data was recorded during the preliminary test. Devices to record buckling load, load vs displacement history and out-of-plane displacement which are typical data recorded for buckling experiment were not installed. Mostly quantitative data can be compared with the results from the numerical model. More precisely, the approximate shape, size and location of the buckling wave as inferred from Figure 3.5, and the crack location from Figure 3.4b.

## 3.2 Modelling Approach

The numerical work was done using the finite-element software Abaqus 6.14. This software was chosen because it is the primary software used by the research group and because a full scale-model of the blade had already been created with it. The general idea is to start with the full-scale blade model and cut away unwanted regions so that what remains is the desired blade section.

### 3.2.1 Full-Scale Blade Model

A full-scale model of an SSP 34 m blade was provided by the authors of [23]. Please note that the modeling decisions taken in making the full-scale blade model described in this section (Section 3.2.1) were made by the creator of the blade model, not from the author of the thesis report. All other sections of the thesis report features modeling decisions made by the author of the present thesis report. More in-depth information about this blade model can be found in [23].

The panel and box girder is made of  $6.7e4$  8-node doubly curved thick shell elements with reduced integration (Abaqus type S8R). This element type is used because it models quite well the composite details found in the blade. In order to model the adhesive sections, 4 layers of  $2.75e5$  8-node linear brick (solid) incompatible mode elements (Abaqus type C3D8I). This was shown to give better results compared with modeling the adhesive with shell elements. These element types are explained in more details in Section 3.2.5. The composite shell elements and the adhesive solid elements were joined via tie-constraints. These are so-called multi-point constraints (MPC) where the translational motion is constrained at each slave nodes (solid elements) and a moment will be applied to the relevant nodes on the master surface (shell elements) because of the existing offset between the reference surface of the shell and the solid elements. According to the Abaqus manual, the surface-based constraint will behave correctly under rigid body rotation regardless of the amount of offset [37]. The blade also features surface-to-surface interaction between the pressure side and suction side panels in order to prevent penetration of the two surfaces during large deformation.

The material properties and the composite lay-up were defined for their respective sections throughout the blade (see Figure 3.6). Information on material properties, composite layups, and thicknesses is confidential and so it cannot be included in this report.

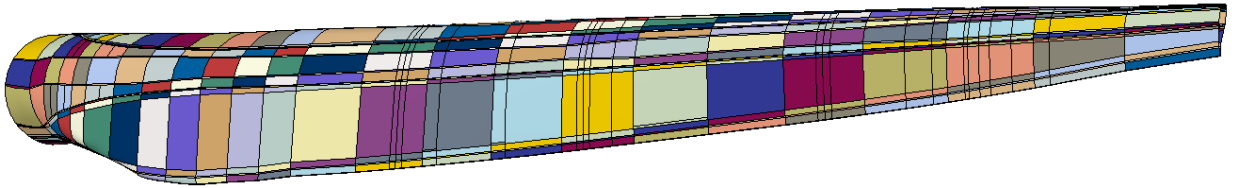


**Figure 3.6:** Full-scale blade model with color-coded composite sections.

The model has been shown to be very representative of the real blade. According to [23], global displacements were measured at four radial locations along the blade during a full-scale static test under combined flapwise and edgewise loading (see Figure 2.9) and the most pronounced deviation between numerical and experimental results, at any load up to failure, was less than 4%. It also correctly predicted that the failure mechanism would be core shear failure [23].

### 3.2.2 Blade Section

Even though the cut-out section of the blade ended up being slightly shorter than 3 m in length, at 2.87 m, and that it was only known to be cut at approximately 26 m to 29 m radius, it was decided that the section between exactly 26 m and 29 m would be chosen to be modelled, making it exactly 3 m long. It was decided to move forward in this way to keep the model simple and because the later blade sections tested would most likely be cut more carefully such that it is 3 m in length and thus it would be important to stay consistent. As mentioned in the previous section, the length between the shear web closest to the trailing edge and the cut was measured, using a measuring tape, to be 17.5 cm on the tip side and 19 cm on the root side. For simplification purposes, the blade model was cut 18 cm away from the shear web along its whole length. Figure 3.7a shows

the blade section as seen on the full-scale model, Figure 3.7b displays the section only (the thickness of the shell elements is not displayed), while Figure 3.7c shows the trailing edge section with the composite shell elements shown with their representative thickness (in blue) and the solid adhesive elements (in green). Note that the thickest shell elements represent a composite sandwich construction with a core in the center as opposed to the skin only.

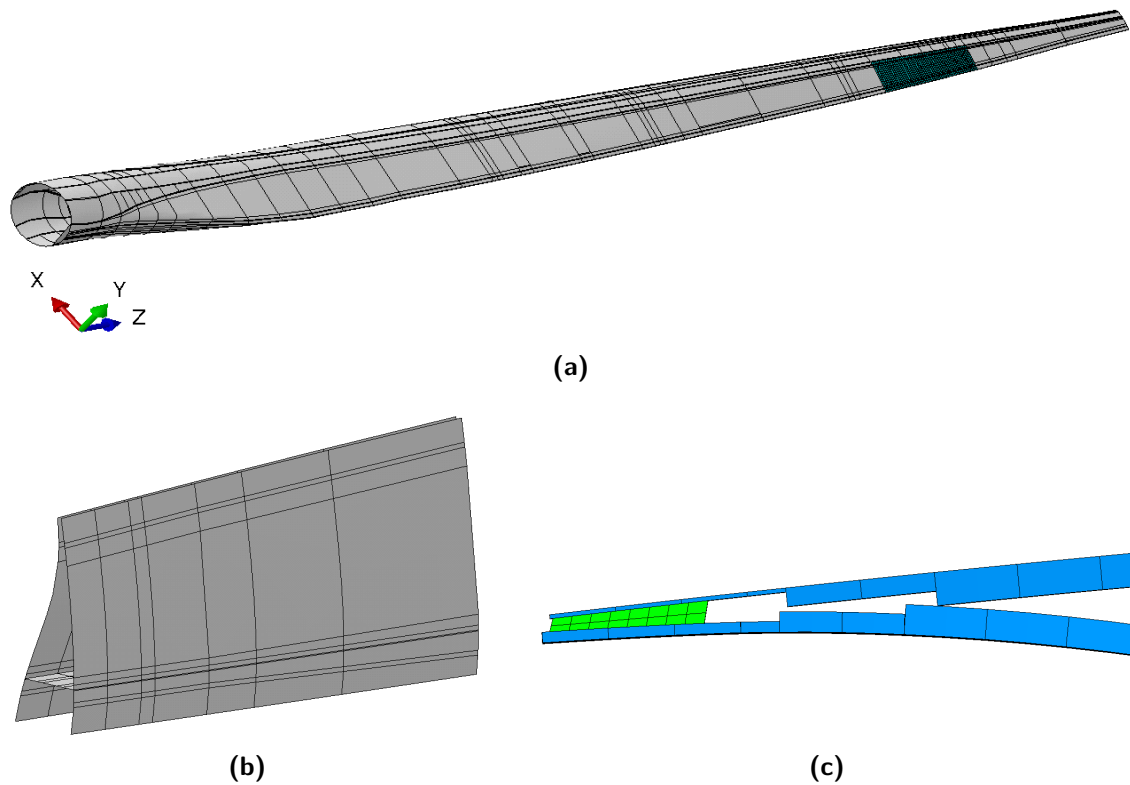


**Figure 3.7:** a) Full-blade model showing the blade section shown in blue. b) The blade section made of shell elements (thickness not shown). c) Trailing edge showing the composite shell elements in blue and the solid adhesive elements in green.

### 3.2.3 Plates and Assembly

The two steel columns were modeled with 3D solid elements and assumed to be infinitely stiff (the actual Young's modulus entered was  $1.0E18$ ). The columns, which we will refer to as plates in the model, are 2 m tall, 0.8 m wide and 0.2 m thick. The thickness and width differs from the real column since it is not of importance for the simulation. What is necessary is the width to be larger than the blade piece width and the plate to be extremely stiff to account for the column thickness.

The plates were placed on both ends of the blade as shown in Figure 3.8a. The bottom center of the blade cross-section was aligned with the bottom center of the plates, it was then rotated such that the trailing edge is positioned at the center of the plate (Figure 3.8c) and then translate upward slightly so that no blade piece extends below the plate (Figure 3.8b). This assembly closely follows the test set-up. One important difference, however,

is the lack of extra material between the hinge line and the blade section as was shown in Figure 3.4c. The combination of the longer blade modeled (3 m instead of 2.87 m) and the relatively small distance that it is compared to the lengths of the whole set-up means that this difference can be assumed to be negligible. The percent difference between the two lengths is only 4.4% to be exact, from the calculation  $100 * (3 - 2.87) / ((3 + 2.87) / 2)$ .

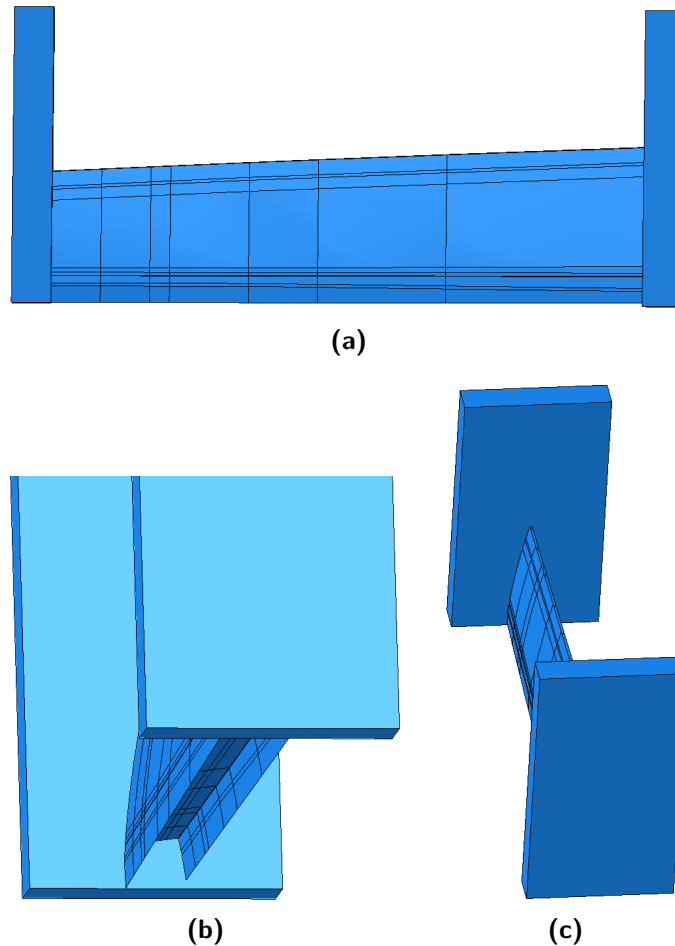


**Figure 3.8:** a) Side view of the assembly. b) Bottom section of the assembly. c) Top view of the assembly.

The nodes along the cross sections of both blade edges were joined to the plates via tie constraints, therefore fixing the blade section to the plates (Figure 3.9). This assumption considers that the interface between the blade section and the wooden planks is quite strong and stable, therefore preventing any sliding. As mentioned earlier, the blade even left a dent in the wooden planks set on the column surface (Figure 3.4d) and so this assumption is quite reasonable since no sliding occurred.

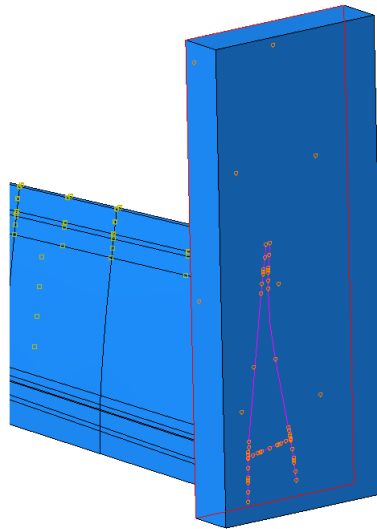


**Figure 3.9:** Tie constraints defined between the blade end (in purple) and the plate surface (outlined in red).

While the original full-blade model had tie constraints joining the glue solid elements to the composite shell elements, cutting the blade section automatically removed these constraints and so they had to be redefined. They were defined in the same way as was done by the creator of the full-blade model. The tie constraints rigidly connects the nodes of the top sections of the blade to the nodes of the glue (as shown in Figure 3.10a on the pressure side) with a position tolerance of 5 cm in order to account for the gap due to the shell thickness. Tie constraints are also placed between the bottom and top glue parts, with 0.01 position tolerance (Figure 3.10b).

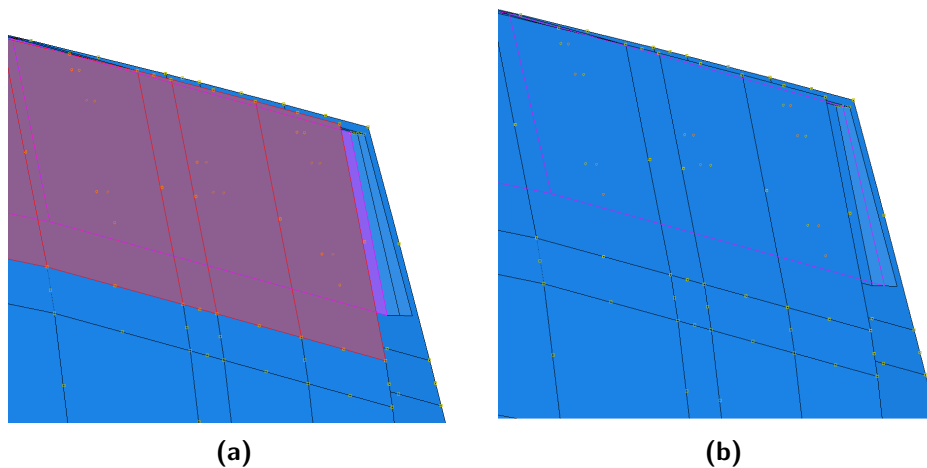


**Figure 3.10:** a) Figure showing the surfaces selected for fixing the pressure side panel (in red) to the glue (in purple), via tie constraints, accounting for the offset. b) Tie constraints joining the bottom and top glue parts (outlined in purple).

The surface-to-surface interaction that is implemented between the the pressure side and suction side panels also had to be specified again after the blade was cut (Figure 3.11).

While interactions properties are also typically defined (such as contact conditions), defining this property is not needed in order for the interaction to prevent penetration of the panels. Not redefining this interaction after cutting the blade can lead to completely erroneous results (as was found from the author of the thesis report) and so care must be taken to verify that it is in fact included in the model.

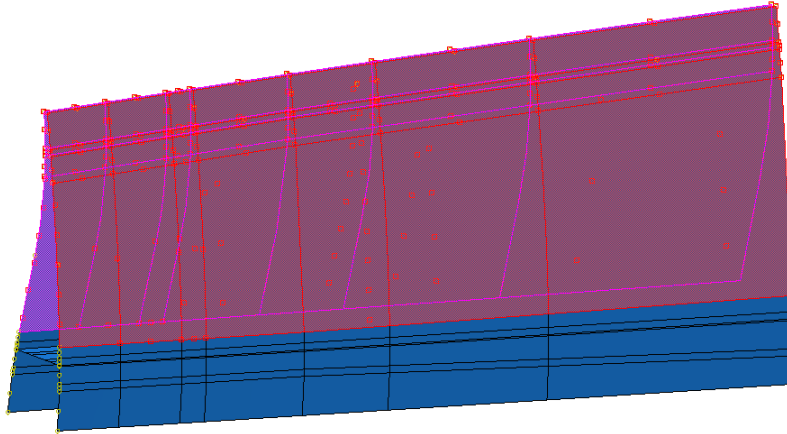


**Figure 3.11:** Surface-to-surface interactions defined between the pressure side and suction side panels to prevent penetration. The panel thickness is also accounted for by default.

### 3.2.4 Boundary Conditions

The boundary conditions defined on the model are shown in Figure 4.3. Concentrated loads were placed at the top center of the plates, where the steel bar is located in the test set-up. The plates are only allowed to rotate about the y-axis direction in order to represent the hinge at this location. Vertical motion of the blade is restricted along the two bottom edges and sideways motion is restricted at the middle point of these edges. This was done to prevent rigid body motion but is also quite representative of the test set up since the steel plates limited sideways motion and the wood blocks limited vertical motion.

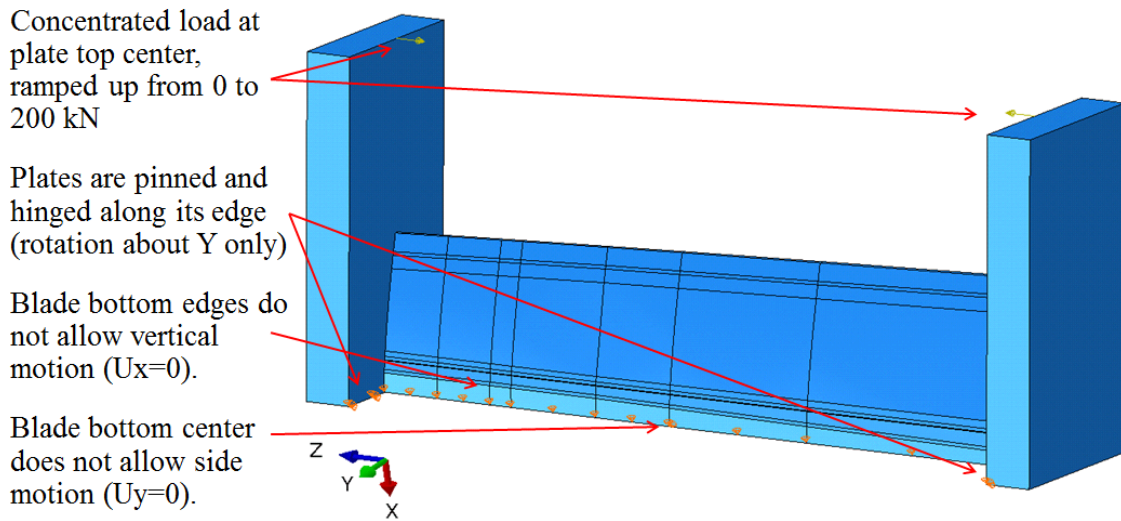


Figure 3.12: Boundary conditions applied to the model.

### 3.2.5 Elements and Meshes

The composite sections of the blade are made of shell elements, more precisely the element type called S8R from Abaqus terminology which is an 8 node doubly curved thick shell element with reduced integration. Reduced integration means that less Gaussian points are used in the integration done inside the element and this has the effect of reducing the stiffness of the element. This can improve the approximation of real-life behavior since full integration always over-estimates the stiffness matrix. This second-order interpolation element type was chosen by the authors of [23] because it is very suitable for the analysis of composite shells and because it takes into account transverse shear flexibility. This can be important for the modelling of the sandwich construction used in the wind turbine blade because the sandwich core is made of softer material.

It was decided from the authors of [23] that the adhesive sections of the blade would be composed of solid elements of type C3D8I which are 8 node linear brick elements with incompatible modes. Incompatible mode elements are enhanced elements which uses the incompatible model to capture bending more accurately and are therefore quite effective when large bending is present [38]. This element also has shear locking and hourglass control.

Finally, the plates were modeled with solid elements of type C3D8I. The simple reason was to stay consistent with the solid element type chosen for the adhesive. The element type chosen is not important for the plates because the results in the plates are not of interest and because the plates are modeled as being stiff so no strain is expected throughout.

The original mesh of the full-blade has a characteristic element size of 5 cm for the composite shell elements and of 1 cm for the adhesive solid elements. This mesh density was said to be suitable for this large model and for the scope of the analysis. The modeling of only a short section of the blade allows the possibility of increasing the mesh density while keeping a reasonable number of total elements.

**Table 3.1:** Details of the five meshes created. The number of elements and nodes shown comprises the composite and adhesive elements. These statistics are with shell elements of type S8R.

Characteristic Element Size - Shell [cm]	Number of Elements	Number of Nodes
5	7,680	19,693
4	9,225	24,380
3	12,225	33,460
2	21,064	60,147
1	67,200	199,053

Hence, a short mesh convergence study was carried out to make sure that the results were not overly dependent on the mesh details. A total of five mesh were created for the model, with different levels of discretization as seen in Table 3.1. The discretization level was modified by changing the approximate characteristic length of the composite shell elements, starting from the characteristic element length of the full-blade model. The characteristic length of the adhesive solid elements was kept at 1 cm for this analysis since it is more simple to analyze the results from changing one parameter only and because the adhesive section is relatively small. The adhesive contains 4,800 elements and 10,836 nodes. The number of elements shown in Table 3.1 are for the blade section only (i.e composite and adhesive) since the plates are simply there to introduce the loads and are not part of the buckling analysis. The mesh of the plates were also left relatively coarse at an approximate characteristic element size of 5 cm because discretizing it further will increase solving time and not change the results since the plates are assumed infinitely stiff. A quick test was done with a very small meshes sizes and it confirmed this point. Each plate is composed of 2,560 elements and 3,485 nodes.

### 3.2.6 Analysis Types

From what was learned in the literature study, three important analysis methods that should be attempted for this buckling problem. These are the linear eigenvalue buckling analysis, the nonlinear static analysis and the dynamic implicit analysis.

For the linear eigenvalue buckling analysis, the first 10 eigenvalues and eigenmodes were requested, the max number of iterations was set to 10,000 and the number of vectors was set to 50.

For the nonlinear static analysis, both the Newton-Raphson and Riks methods were used to verify that the results were consistent using different numerical algorithms. For both methods, the nonlinear capability of the solver was turned on, the time period was set to 1 s, the max number of increments was set to 10,000, the initial increment size to 0.1 s, the minimum increment size to 1E-05 s and the maximum increment size to 0.1 s.

For the dynamic implicit analysis, the nonlinear capability of the solver was turned on, the time period was set to 10 s, the max number of increments to 10,000, the initial increment size to 0.1 s, the minimum increment size to 1E-5 s and the maximum increment size to 0.1 s. Additionally, the loading was set to a load amplitude increasing linearly from 0 to

200 kN over 10 seconds, in order to simulate a quasi-static condition in which the load is applied slowly instead of instantaneously.

### 3.3 Results

#### 3.3.1 Results of Mesh Refinement Study

The mesh refinement study was done by following the guidelines from the standards of Section 2.4.1. A linear eigenvalue buckling analysis was performed on the five meshes and the buckling load of the first mode was retrieved. Figure 3.13a shows the results vs. characteristic element size of the shell elements while Figure 3.13b shows the results vs. number of elements in the blade section. Also shown in the plots are the results from using the element type S4, which is a linear four-noded general purpose shell element. The results confirm that the S8R element type is superior to the S4 element since convergence can be reached with much fewer elements using this element type. Using a second-order element with 8 nodes has the advantage to represent curved geometries better.

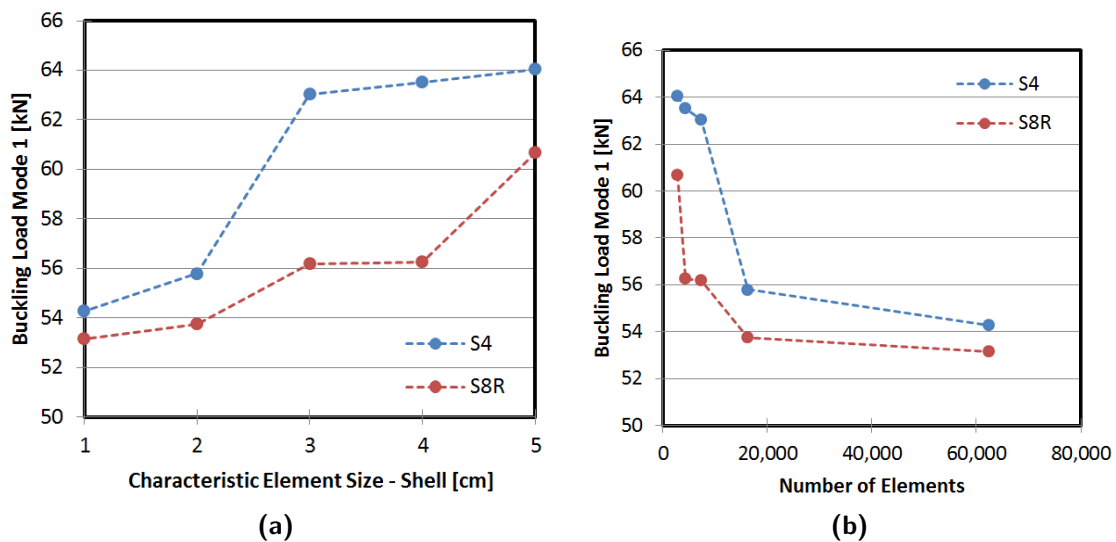


**Figure 3.13:** a) Buckling load of mode 1 from linear eigenvalue analysis vs. characteristic element size of the shell elements. b) Buckling load of mode 1 from linear eigenvalue analysis vs. number of elements in the blade section.

The results show that the mesh with the shell elements having characteristic lengths of 4 cm with S8R elements has sufficiently converged from the rule of thumb specifying that convergence is reached when the buckling load does not change by more than 5% when the number of element is doubled. It therefore appears that the 4 cm characteristic is sufficient. This convergence study up until now assumes that the results from the linear eigenvalue buckling analysis are correct. It was decided that the buckling load would also be calculated from a different analysis type to reaffirm that the results have in fact converged with a mesh size of 4 cm.

As will later be discussed, the dynamic implicit solver was quite effective in modelling the buckling of the blade section. From the results of this analysis, the displacement history in the z-direction was extracted at the end node on the tip side of the blade, as shown in Figure 3.14. The load-displacement curves were then created for the different mesh densities, displayed in Figure 3.15. Figure 3.15a shows a clear drop in stiffness at around 70 kN which coincides with the buckling of the blade section. This is higher than the prediction from the linear eigenvalue buckling analysis, therefore showing the difference in results between the different analysis. When zooming in on the region of interest (Figure 3.15b), the difference in results between the different mesh densities become more apparent. The curve for the 5 cm characteristic length appears slightly off from the other curves, while the others match quite well. The simulation using the finest mesh is also seen to end sooner than the others, probably due to instability issues. The buckling load appears to lie between 68 and 70 kN. Overall, this analysis shows that using the mesh with approximate characteristic length of the shell elements of 4 cm fares quite well, and further confirms that the mesh has converged sufficiently at this mesh density. This mesh is therefore selected and is used for the remainder of the chapter.

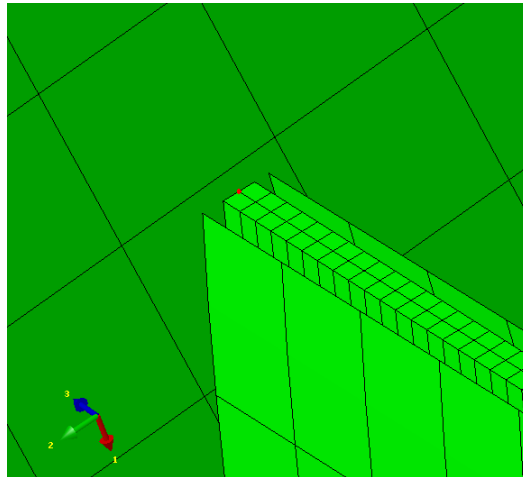


**Figure 3.14:** Location of node (in red) at which displacement in the z-direction (aka 3-direction) is calculated for the load-displacement diagram.

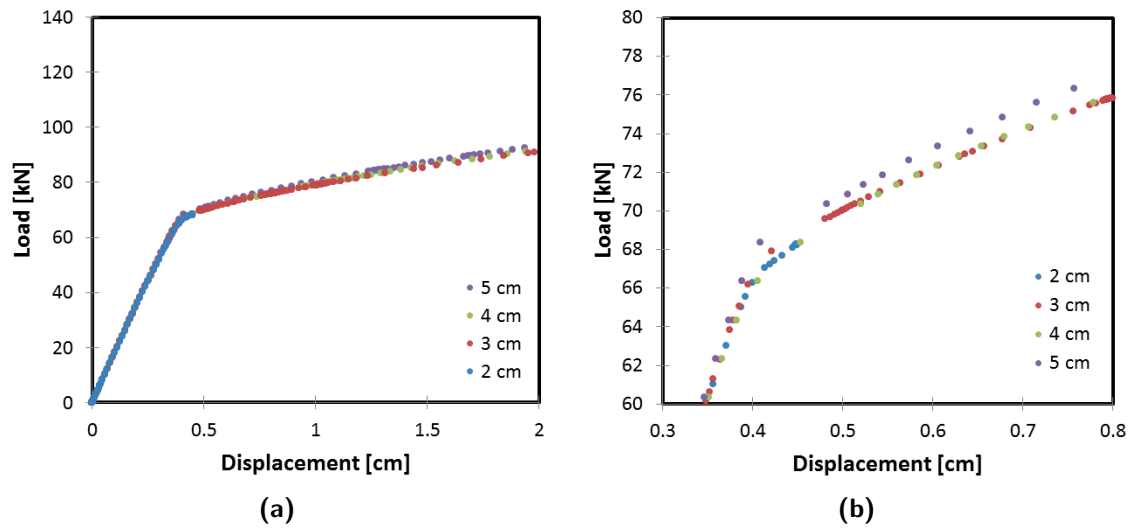


**Figure 3.15:** a) Load-displacement diagram from the displacement of the end node on the tip side, for different mesh densities. b) Close-up around the buckling region.

While the mesh refinement study appears straightforward, it is important to clarify one important weakness of the methodology employed. That is, even though the element size is smaller, the model's accuracy is still limited by the number of sections that are used. Figure 3.7c, clearly illustrates this concept. If the model is to become much more precise, then more sections should be used such that the composite thickness more closely follows the actual distribution in the blade. In other words, since it is simply taking an average thickness over a certain area, reducing the area per section would overall help achieve a more accurate thickness profile. Refining the sections is very time consuming and much more work than needed for this preliminary assessment and so it was decided that this strategy would not be pursued. The results to compare with the experiment are mostly qualitative after all and so this level of detail is not necessary.

### 3.3.2 Linear Eigenvalue Buckling Analysis Results

The lowest eigenmode gives a buckling load of 56.3 kN, and this is therefore the critical buckling load (i.e the load of the first bifurcation point) according to this analysis type. The associated displacement field is shown in Figure 3.16a and was automatically scaled by the software such that the maximum displacement is 1 m. The buckling wave is located on the tip side and suction side of the blade section, like was seen in the experiment (see Figure 3.5). The second mode might also be of interest since its buckling load is quite close to mode 1. The buckling load of mode 2 is 60.6 kN and its mode shape is seen in Figure 3.16b. The next 8 eigenmodes outputted were shown as spikes and so they are clearly affected by some form of numerical error (see Figure 3.16c).

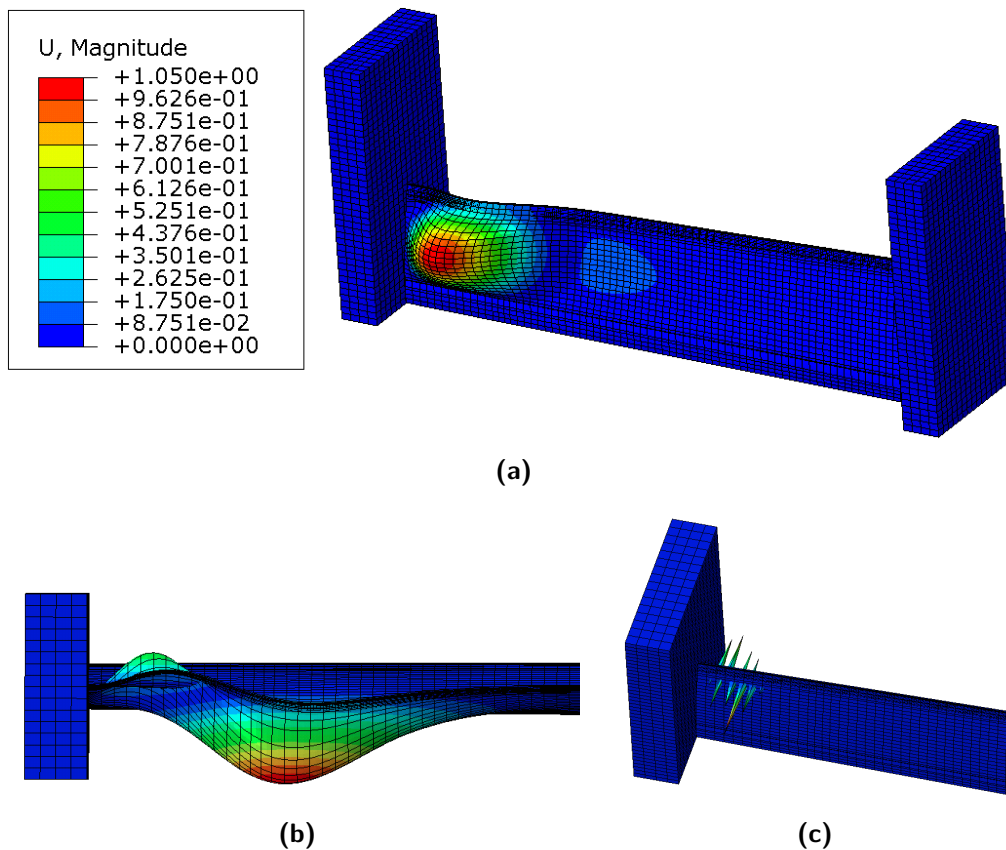


**Figure 3.16:** a) Mode 1 displacement field from linear buckling analysis. b) Mode 2 displacement field from linear buckling analysis. c) Example of spikes observed for the displacement field results of Mode 3 to Mode 10. Mode 5 is shown here. The legend is applicable to all three figures.

### 3.3.3 Nonlinear Analysis Results

Three nonlinear analyses were performed, nonlinear static analyses under Newton-Raphson and Riks formulation and nonlinear dynamic implicit analysis under a quasi-static state. For the dynamic analysis, kinetic energy was found to be much lower than strain energy and so the simulation results do show the quasi-static condition.

Load-displacement graphs of all three analyses were created using the displacement of the node from Figure 3.14 and the results are shown in Figure 3.17. Note that since the Riks method updates both the load and displacement at each increment, it is not as straightforward to calculate the load at any given increment. To still obtain useful results, the maximum displacement of the node (at the last recorded time step) was recorded and the load at this time step was assumed to be in line with the other two methods.

The load-displacement diagram reveals that the Riks analysis crashes much earlier from equilibrium divergence than the other two analysis, in fact right before buckling occurs. The nonlinear static analysis covers a considerably longer time history while the dynamic implicit analysis is able to retain stability in the solution far longer. There is a good match

in load-displacement history between at least the nonlinear static with Newton-Raphson and nonlinear dynamic implicit analysis.

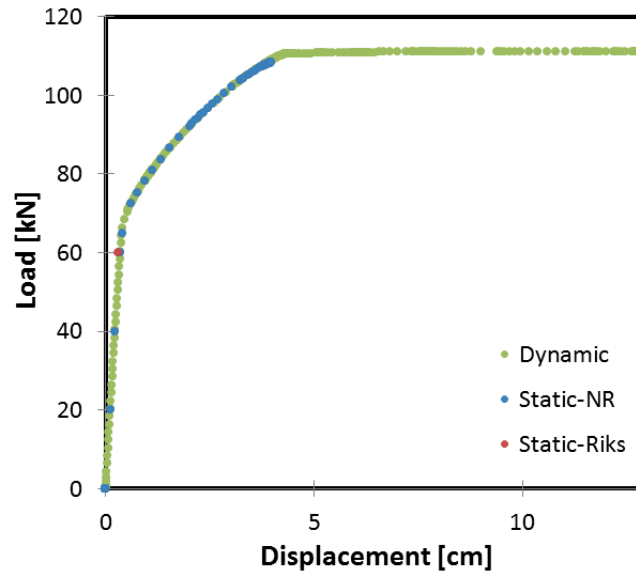


**Figure 3.17:** Location of node at which displacement in the z-direction (aka 3-direction) is calculated for the load-displacement diagram.

The displacement field at the last recorded load step of each analysis is seen in Figure 3.18. The solution from the Riks analysis clearly did not fully develop before divergence. The displacement field from Newton-Raphson and dynamic analysis are quite similar, with the deformation being even more pronounced with the dynamic analysis. Of course, the last two displacement fields are not expected to be real because material failure would likely occur before then. This is verified shortly. The buckling wave direction and location is consistent between the different analysis, being located on the tip side and the wave being towards the pressure side, opposite to the linear buckling analysis and the experiment.

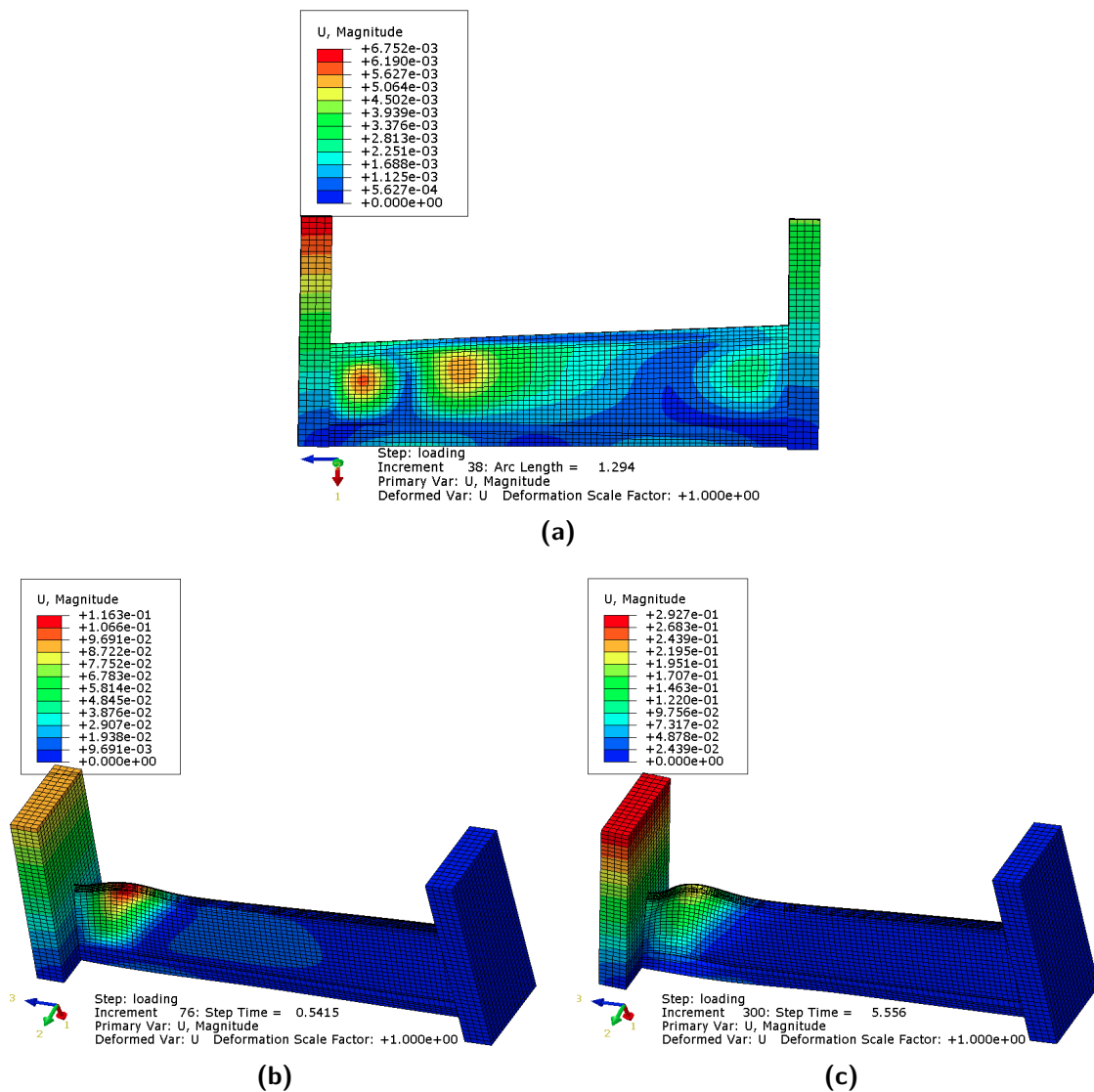


**Figure 3.18:** Displacement field of last recorded load step. a) From static analysis using Riks method. b) From static analysis using Newton-Raphson method. c) From dynamic implicit analysis using.

Finally, the displacement field at a load of 72.45 kN, which is right after buckling occurs, is displayed in Figure 3.19 from the Newton-Raphson and dynamic analysis. The displacement field is almost identical and so along with the matching load history, it can be inferred that the solution history is the same between the two methods. The dynamic implicit solver however has the advantage of being more robust and it also by default outputs results at many more load steps. This analysis type is found to be the most convenient for this modeling problem and is the preferred solution strategy for the remainder of the thesis project.

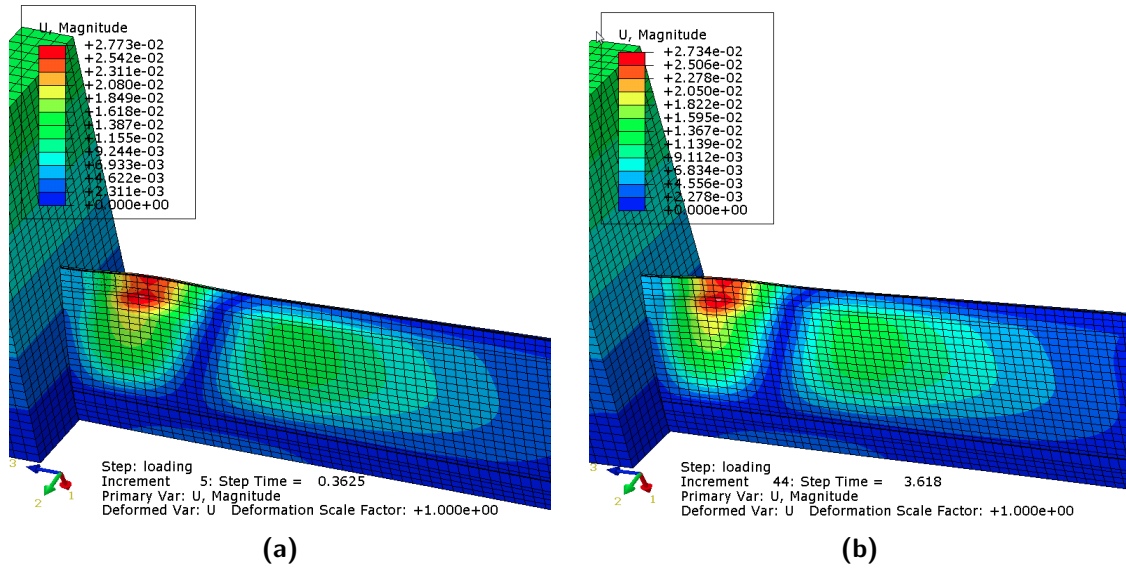


**Figure 3.19:** a) Displacement field from static analysis using Newton-Raphson method at a load of 72.5 kN. b) Displacement field from dynamic implicit analysis at a load of 72.4 kN

Another important analysis which can be done is to look into composite material failure. Analyzing failure for composite materials is much more involved than for metals. For example, a laminate that is acted under a certain longitudinal strain (therefore making each individual lamina deform by the same amount since they are essentially "glued" together) will have its different plies see different stresses because they each have different stiffness (which can come from using different materials or from their fibers being angled differently) and each different ply will also have different maximum stress limits (i.e strength). When analyzing failure in a composite laminate, we typically try to determine the first ply that will fail because it is the start of progressive failure and there is uncertainty as to how much extra load it can take, if at all. Therefore, the comparison of the stress or strain state of the on-axis lamina is compared to its strengths to assess whether it will fail and this is done by the use of failure criteria. While most experimental strength measurements are based on uniaxial stress states, the use of failure criteria allows the consideration of multiaxial state of stress, which is more representative of the stress states found in structures. There exist many failure criteria, each having their own strengths and weaknesses. Four well known failure criteria for composite materials are the Maximum stress, Maximum Strain, Tsai-Hill and Tsai-Wu.

The Tsai-Wu failure criterion is especially widely used because it has the advantage over the Maximum Stress and Maximum Strain criterion to consider biaxial stress states. While the Tsai-Hill failure criterion also considers biaxial stress states, the Tsai-Wu criterion has the additional advantage to account for the difference between tensile and compressive strengths [39]. It is also mathematically simple because it follows normal tensor transformation equations and it is easy to incorporate in a computer software. The Tsai-Wu failure criterion requires that:

$$F_1\sigma_1 + F_2\sigma_2 + F_{11}\sigma_1^2 + F_{22}\sigma_2^2 + F_{66}\tau_{12}^2 + 2F_{12}\sigma_1\sigma_2 < 1 \quad (3.1)$$

where,

$$\begin{aligned}
 F_1 &= \frac{1}{\hat{\sigma}_{1t}} - \frac{1}{\hat{\sigma}_{1c}} \\
 F_2 &= \frac{1}{\hat{\sigma}_{2t}} - \frac{1}{\hat{\sigma}_{2c}} \\
 F_{11} &= \frac{1}{\hat{\sigma}_{1t}\hat{\sigma}_{1c}} \\
 F_{22} &= \frac{1}{\hat{\sigma}_{2t}\hat{\sigma}_{2c}} \\
 F_{66} &= \frac{1}{\hat{\tau}_{12}^2}
 \end{aligned}$$

and where,

$$\begin{aligned}
 \hat{\sigma}_{1t} &= \text{Longitudinal tensile strength} \\
 \hat{\sigma}_{1c} &= \text{Longitudinal compressive strength} \\
 \hat{\sigma}_{2t} &= \text{Transverse tensile strength} \\
 \hat{\sigma}_{2c} &= \text{Transverse compressive strength} \\
 \hat{\tau}_{12} &= \text{In-plane shear strength}
 \end{aligned}$$

The strength values were given by the manufacturer of the SSP 34 m blade for each lamina type and they were inputted in the Abaqus model.

The parameter,  $F_{12}$ , requires a combined stress, or biaxial load case to be applied to the material. This test is difficult to perform experimentally, and so the need of this parameter is a main disadvantage of the Tsai-Wu formulation. If the equibiaxial stress at failure,  $\sigma_{biax}$ , is found from an experimental test on the lamina and is entered in Abaqus, then,

$$F_{12} = \frac{1}{2\sigma_{biax}^2} \left[ 1 - \left( \frac{1}{\hat{\sigma}_{1t}} + \frac{1}{\hat{\sigma}_{1c}} + \frac{1}{\hat{\sigma}_{2t}} + \frac{1}{\hat{\sigma}_{2c}} \right) \sigma_{biax} + \left( \frac{1}{\hat{\sigma}_{1t}\hat{\sigma}_{1c}} + \frac{1}{\hat{\sigma}_{2t}\hat{\sigma}_{2c}} \right) \sigma_{biax}^2 \right] \quad (3.2)$$

otherwise,

$$F_{12} = f^* \sqrt{F_{11}F_{22}} \quad (3.3)$$

where,  $-1 \leq f^* \leq 1$ . By default, Abaqus defines  $f^*$  to be equal to zero [40]. The equibiaxial stress at failure was not provided and the default settings from Abaqus were used. For most cases, the  $F_{12}$  coefficient is not critical and it is often simply approximated [39]. More extensive information on composite failure theory can be found in [39].

The Tsai-Wu field showing the failure envelope through all plies in the laminate is illustrated in Figure 3.20. This means that the maximum absolute Tsai-Wu across all plies is shown in the diagram. The limit on the contour plot was set to 1 and so failure is expected

for regions show in grey. Failure is seen to occur right after buckling, at a load of 72.4 kN, on the pressure side of the blade. A stress concentration is seen at the top boundary. This shows that the boundary on this end of the blade creates high local stress which likely results in failure in the region. Failure is also expected right below the adhesive section. These two failed regions are consistent with the location of where the crack started forming and propagated during the first experiment. Figure 3.20, shows the critical ply to be ply-5 and that ply-5 is the innermost ply in the laminate and is made of the material YE900. The main driver for this failure is found to be high transverse compressive stress, as shown in Figure 3.22a. The maximum transverse compressive stress at this load level is  $-1.248 \times 10^8$  Pa which is very close to the transverse compressive strength of this lamina which is  $-1.271 \times 10^8$  Pa. The reason why failure is said to occur even though the stress limit has not been reached is simply due to the nature of what a stress criterion like the Tsai-Wu criterion signifies. It considers the combination of stress from multiple direction all together. The results simply show that the main contribution to this failure is the transverse compressive stress.

Another predicted failure mechanism is core shear failure. Figure 3.22b, shows the out-plane shear stress on ply-4 (which is the core for most of the section apart from the trailing edge tip). The shear strength of the core is  $1.1 \times 10^6$  Pa and this was implemented as limits in the colored diagram. The region in grey (apart from the trailing edge tip, since other material is used there as a 4th ply), shows the failed region under core shear. This failure occurs at a load of 70.4 kN. Core shear failure was determined to be the primary failure mechanism on the full-scale blade buckling tests performed by DTU on this SSP 34 m blade and so it is good to see that the sub-component testing also predicts this same failure mode. One last note is that failure from ply-5 and from the core is expected to occur simultaneously right after the buckling wave forms. This is because in practice, manufacturing uncertainty can be expected to make these failures occur at the same load or time.

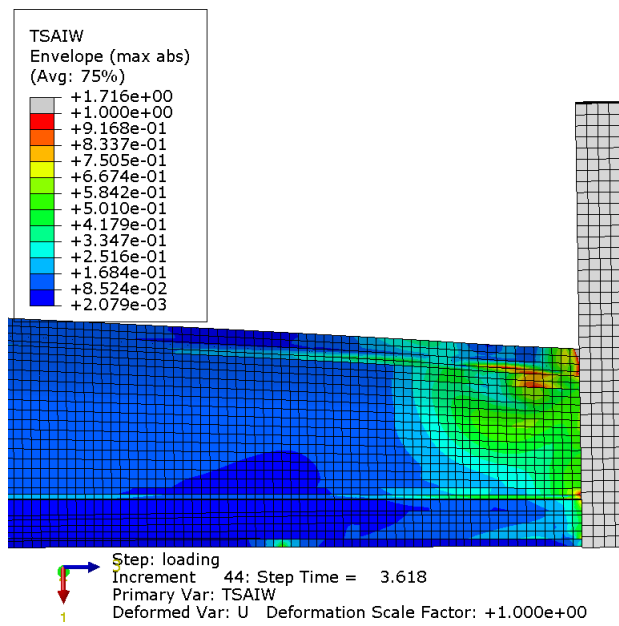


**Figure 3.20:** Tsai-Wu failure criterion field at load of 70.9 kN. Failed regions are shown in grey.

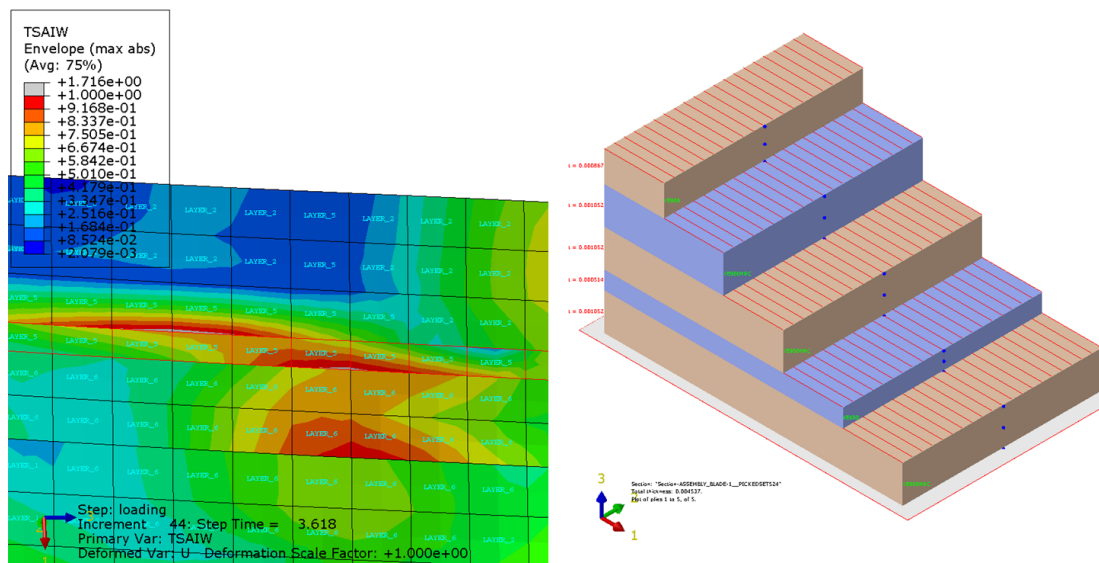


**Figure 3.21:** On the left, Tsai-Wu criterion field with annotation of which ply fail first (ply-5). On the right, laminate in the failed region showing the material and orientation of the failed ply (ply-5). The reference plane where the ply numbering starts is shown in grey.

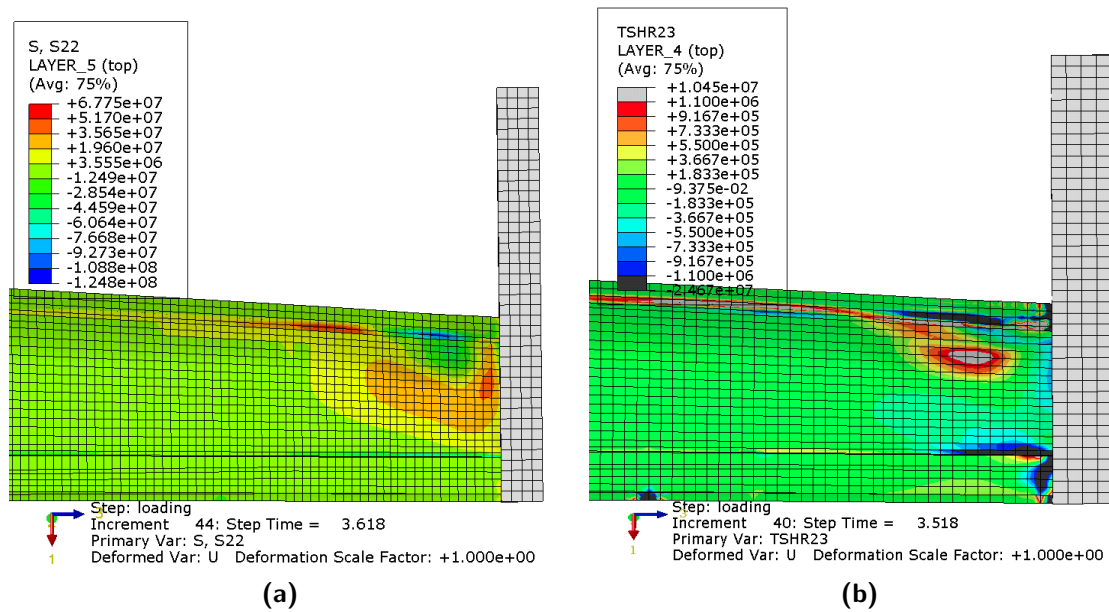


**Figure 3.22:** a) Transverse stress in ply 5 at material failure load. b) Out of plane shear stress demonstrating core shear failure at similar failure load.

### 3.4 Side Study #1: Effect of Imperfections

As was learned from the literature study, imperfections are part of every structure and can significantly affect the buckling analysis results. Even though this specific structure is asymmetric and therefore does not require imperfections to successfully run the simulation, it is wise to do a short imperfection study to verify its effect on the results.

**Method:** The method employed follows quite closely the guidelines from Section 2.4.1. The first eigenmode shape (e.g the buckling wave of Figure 3.16a) was included as an imperfection in the nonlinear analysis using the dynamic solver. Since the displacement was scaled in the eigenvalue analysis such that the maximum amplitude is 1 m, the displacement field had to be multiplied by a new scaling factor in order to obtain the imperfection magnitude. Since the maximum amplitude is 1 m then the scaling factor is simply the value of imperfection at the apex of the wave, in meters. There are two rule of thumbs that can be used to estimate the imperfection magnitude that should be applied. The first one is the guideline from GL which is that the imperfection magnitude should be 1/400 of the wavelength of the buckling wave [22]. The wavelength was measured in the model to be 0.75 m and so the imperfection magnitude (and therefore also the scaling factor to use) is 0.001875. The other rule of thumb says that the imperfection magnitude should be 10% of the shell thickness [41]. The shell thickness of the main section of the blade where the buckle occurs is 0.012104 m and so the recommended imperfection magnitude and scaling factor is 0.0012104. Both of these values are surprisingly close and it makes it quite clear that an imperfection of around 0.001 m should be used. It was decided that imperfections of 0.01 m, 0.001 m and 0.0001 m would be attempted.

**Results:** The imperfection magnitude of 0.01 m was large enough to keep the buckling wave on the same side as the buckling wave from the eigenvalue buckling analysis (see

Figure 3.23a). This was not the case for the smaller imperfections implemented, as Figure 3.23b and Figure 3.23c shows with imperfection magnitude of 0.001 m and 0.0001 m, respectively. Additionally, the displacement field was compared with the case of no imperfections added (Figure 3.23d), at the same load level (arbitrarily chosen), and the results show that adding the imperfections of 0.001 m and 0.0001 m have next to no effect on the response. This therefore shows that the buckling wave direction is not very sensitive to imperfections and that only an excessively large imperfection of 0.1 m, which is 10 times the recommended imperfection to be applied, affected the results meaningfully. The pronounced asymmetry of the blade section therefore provides significant stability and the response is not readily affected by slight imperfections.

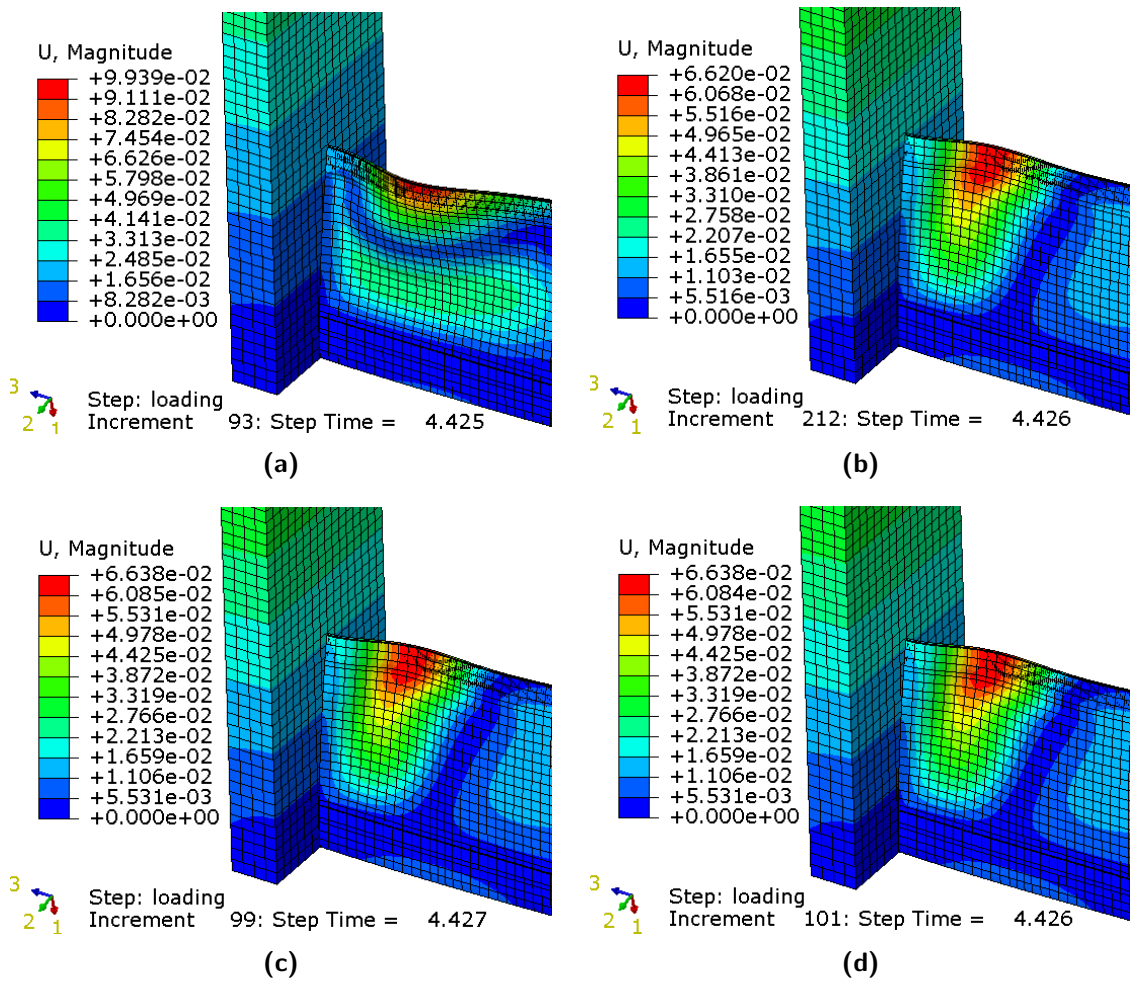


**Figure 3.23:** Displacement field (in m) at load level 88.52 kN after an initial imperfection with the shape of the first buckling mode with a factor (and imperfection magnitude) of a) 0.01 m b) 0.001 m c) 0.0001 m d) No imperfections.

### 3.5 Side study #2: Effect of Blade Angle

The angle at which the blade is loaded was investigated in a short study to see whether it would change the buckling load and the corresponding displacement field.

Method: The blade was rotated about the bottom center of the plates by angles of 20 degrees towards the pressure side (Figure 3.24a), 20 degrees towards the suction side (Figure 3.24b). The angle is defined as being between a vertical line lying in the center of the front surface of the plate and between a line passing through the trailing edge tip and the center point of the piece bottom two corners. For simplicity, the blade was not displaced upwards and so some parts of the blade extends slightly below the plates.

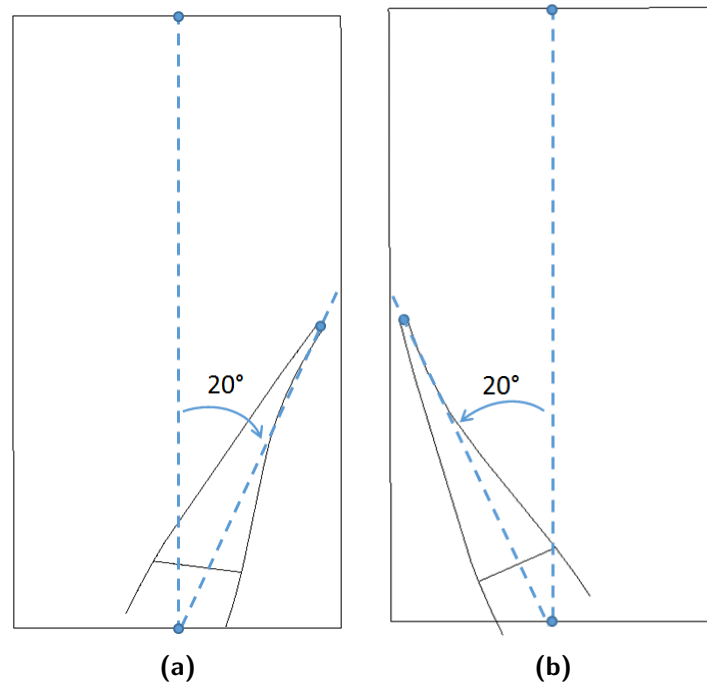


**Figure 3.24:** a) Rotation of 20 degrees towards the pressure side. b) Rotation of 20 degrees towards the suction side.

Results: A comparison of the displacement field is shown in Figure 3.25 between the section which has not be rotated, the section rotated 20 degrees towards the pressure side and the section rotated 20 degrees towards the suction side. This comparison is done at the same load level of 73.9 kN, which is slightly after buckling occurs. The results show that rotating the blade by this amount does not change the buckling wave location or direction. However, the buckling wave magnitude is found to be higher for the blade sections that have been rotated. It is also interesting to see that the displacement field is almost identical between the rotated sections.

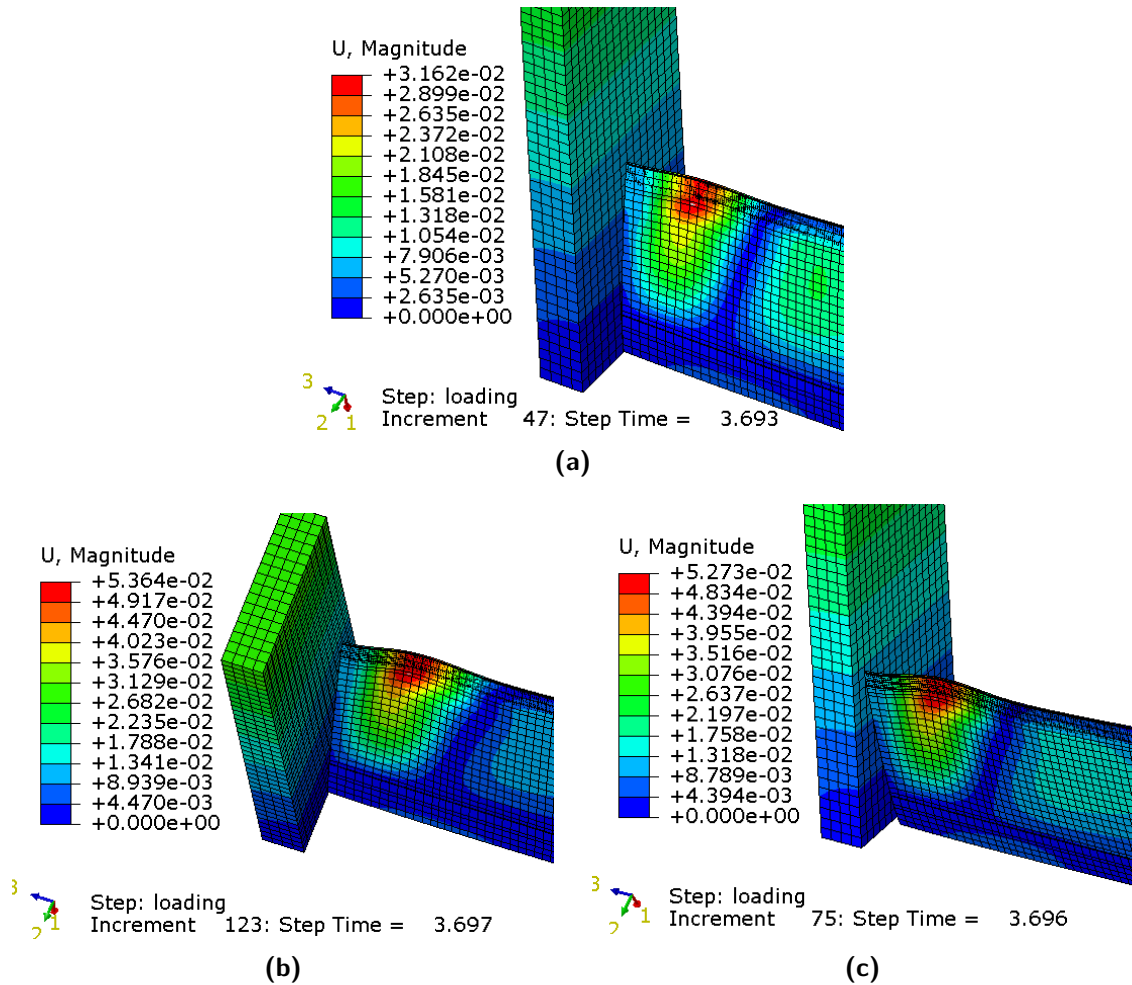


**Figure 3.25:** Displacement field (in m) at load level 73.9 kN for a) Default blade arrangement with tip in the center (i.e no applied rotation) b) Rotation of 20 degrees towards the pressure side c) Rotation of 20 degrees towards the suction side.

Load-displacement curves were generated in the same way as was explained in Section 3.3.1. Buckling occurs from a sudden large displacement with little or no increase in load. To determine exactly when buckling occurs, the slope between each successive points on the load-displacement graph was calculated. The largest sudden negative difference in slope from a time step of 0, was chosen as the point when buckling occurs (shown in by the orange dot in Figure 3.26). The load applied on the plates at this moment in time is the buckling load, and it was calculated to be 68 kN for the default section with tip lying in the plate center, 60 kN for the blade rotated towards the suction side and 59 kN for the blade rotated towards the pressure side. The lower buckling load from the rotated sections was the expected result because the tip of these sections lie at a location on the plate and so there is less internal resisting bending moment from the lower "moment arm" (vertical distance from the hinge line to the blade tip. Finally, the results again show that there is not much difference in rotating the blade towards one side or the other, by the same amount, as the results end up closely matching between the two configurations.

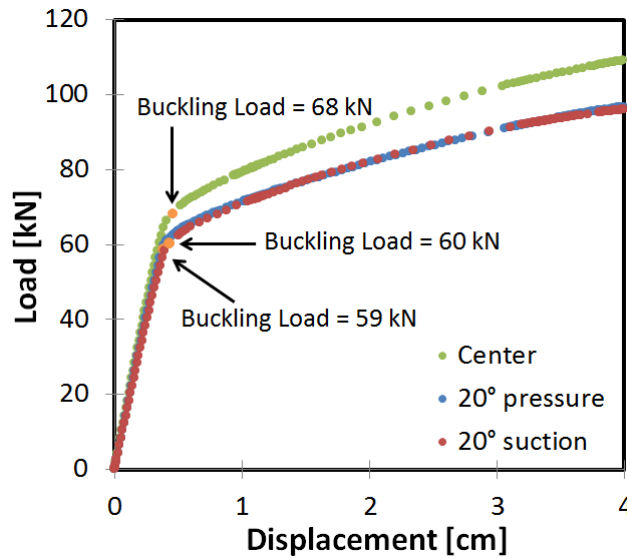


**Figure 3.26:** Load-displacement diagram for the default blade arrangement with tip in the center (i.e no applied rotation), rotated blade 20 degrees towards the pressure side and rotated blade 20 degrees towards the suction side. In this order, the buckling load was found to be 68 kN, 59 kN and 60 kN.

### 3.6 Analysis and Discussion

Generally good agreement was observed between the numerical results and the experimental results. The buckling wave location in the numerical model matches very well with what was seen in the experiment. The buckling wave appears very close to the end of the blade section on the tip side. The Tsai-Wu failure criterion predicts failure to occur on the pressure side of the blade, slightly below the adhesive bondline and at the boundary. This agrees very well with the experiment because it corresponds with where the crack initiated and propagated.

While the buckling wave in the eigenvalue buckling analysis was in the same direction as the experiment, namely towards the suction side, the buckling wave was in the opposite direction in the nonlinear static and dynamic analysis.

The convergence study showed that a characteristic length of 4 cm should be used for the shell elements in order for the mesh to have sufficient accuracy while ensuring the model to not be too computationally expensive. The dynamic implicit analysis was also found to perform better than the other nonlinear analysis types. While the linear eigenvalue buckling analysis was helpful for the convergence study, the complexity of the blade section favors the use of a nonlinear analysis such as the dynamic implicit analysis in quasi-static state. Other findings include the insensitivity of mesh density in the plates, the high sensitivity of element type chosen in the blade section (S8R fares much better than than the default S4 element), the insensitivity of the buckling location and shape from small blade rotation, and the fact that the imperfections implemented need a very high magnitude, at least 10 times greater than the common rule of thumbs, in order to have an impact on the results of this model.

Overall, the model appears to be good enough to be used in further investigations, namely to move the buckling wave closer to the center of the blade section.

# Simulation of Full-Scale Blade Model under LTT Loading

One important requirement of sub-component testing is to ensure that the local loading condition of the area under investigation is equivalent to what is seen in the actual blade structure (See DNV-GL guidelines in Section 2.1). Because sub-component testing of the trailing edge is aimed as a partial substitute to full-scale testing, the loading introduced on the sub-component section should therefore resemble the loading seen by the same region during full-scale testing. According to [12], the blades are typically tested under two flapwise and two edgewise load cases (see Figure 4.1). The particular load case relevant to the current study of trailing edge buckling is the leading towards trailing edge (LTT) load case since it is the load case that exhibits the highest level of compression loading at the trailing edge. In this chapter, a finite-element simulation of the full-scale blade model acting under LTT loading is performed. This simulation allows the comparison between the longitudinal strain of the full-scale model, at any cross-sections, with the longitudinal strain results from the sub-component simulation to verify that the loading condition of the sub-component is equivalent to the loading condition of the full-scale test under the LTT load case. This comparison is done in Chapter 5.

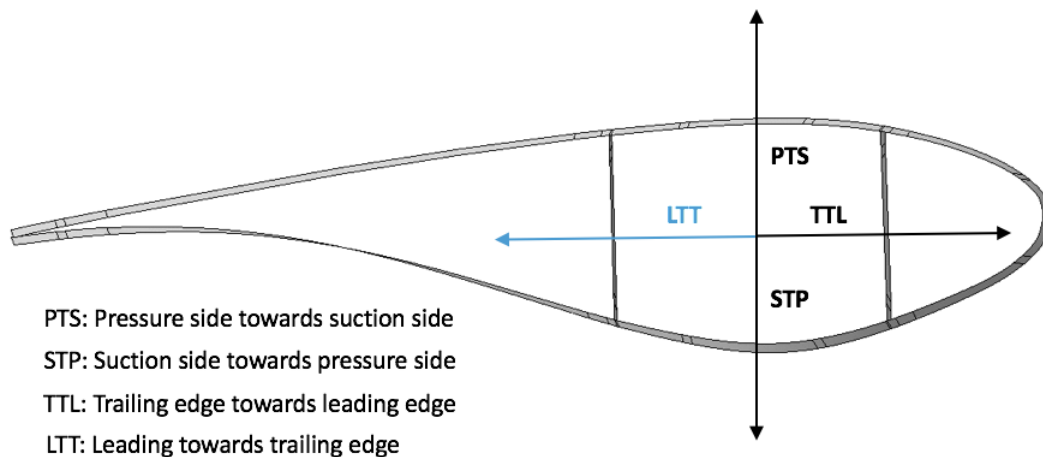


**Figure 4.1:** Load case types and directions. The load case relevant to this study, the LTT, is highlighted in blue.

## 4.1 Simulation Setup

The same full-scale blade model presented in Section 3.2 was used for this simulation.

The blade root was modeled as fixed, such as to follow the directions specified by the IEC standard for full-scale testing of wind turbine blades. A node constrained in all degrees of freedom was inserted at the root center and joined to the nodes making up the root via a kinematic coupling constraint. Fully fixed boundary condition was then applied on this node to effectively fix the whole blade root. The kinematic coupling constraint at the root is shown in yellow in Figure 4.2 while the fully fixed boundary condition is shown in Figure 4.3.

To apply the loads, nodes at the elastic center of 5 cross-sections along the blade were inserted with fully constrained degrees of freedom and then joined to the blade skin via a uniform structural distribution coupling. This is shown for one of the nodes by the orange lines in Figure 4.2. The applied load locations and final magnitudes are shown in Table 4.1. All loads are linearly increasing with time in the simulation and they point towards the trailing edge, more precisely the -x direction of the global blade coordinate defined at the root, as shown by the yellow arrows in Figure 4.3. The location and final magnitudes of the applied loads come from the LTT design load case provided by the manufacturer of this blade. Finally, the structural distribution coupling represent the actuator locations for the applied load.

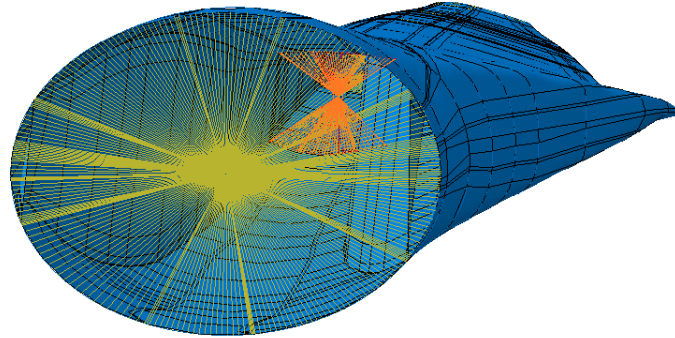


**Figure 4.2:** The kinematic coupling constraint used to link the central node to the root node is shown in yellow while the uniform structural distribution coupling constraint connecting the central node at  $z=13.12\text{m}$  to the blade skin is shown in orange.

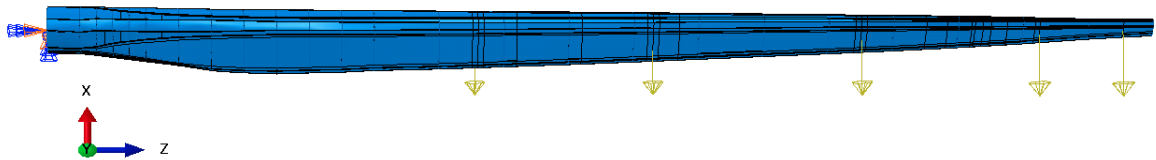


**Figure 4.3:** The boundary conditions applied to the model. The central node at the root is fully constrained while five point loads are applied on nodes located at cross-section centers.

**Table 4.1:** Applied point loads for LTT load case.

Point Load #	Distance from root (z coord.) [m]	Magnitude [N]
1	13.12	32,010
2	18.60	25,340
3	25.04	28,640
4	30.51	11,430
5	33.09	2,890

Finally, a nonlinear static analysis was performed following the Newton-Raphson method.

## 4.2 Method for Obtaining Longitudinal Strain

The longitudinal strain is the result primarily sought for from this simulation. This is because from this load case, the longitudinal strain is much higher in magnitude than transverse strain and so it is less prone to subtle deviations coming from slight out of plane displacement. The longitudinal strain on the skin can easily be compared between full-scale and sub-component specimens at selected cross-sections. The method used to obtain the longitudinal strain was quite involved and so the steps employed are carefully explained in this section.

A path was first created by individually selecting the nodes at a particular cross-section. The path starts from the trailing edge node on the suction, goes all around the cross-section and ends on the trailing edge node on the pressure side, as shown in Figure 4.4 for  $z=14$  m. It was decided that enough nodes would be included in the path by only selecting the nodes at the element corners as opposed to also selecting the nodes at the mid-edges. The node ID's from the selected nodes were automatically put in a list by Abaqus. Then, since the input file generated by Abaqus lists all nodes in the model on individual rows, and each row contains the node ID, the global x, global y and global z coordinate of that node, the global coordinates of the nodes on the path were simply found by scanning through (using the VLOOKUP function in Excel) the input file of the simulation for the desired node ID's and extracting their global coordinates.

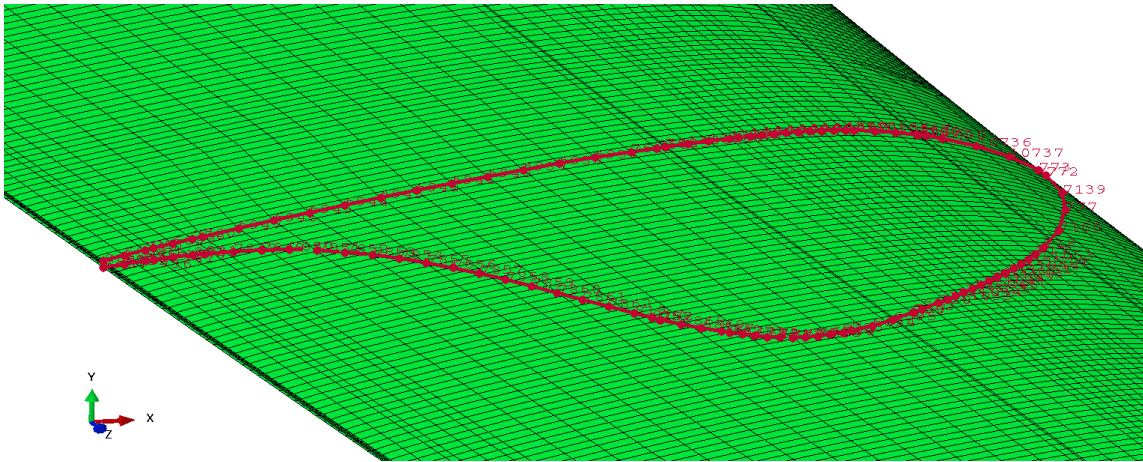


**Figure 4.4:** Path at  $z=14$  m.

The longitudinal strain on the outside surface of the cross-section was selected to be extracted for all nodes along the path. More specifically, this is the strain for the integration point located at the bottom of ply 1, in the 1-direction. Figures 4.5 and 4.6 can help show exactly why this specific strain was chosen. Figure 4.5 shows that the cross-section is composed of many different sections each having its own composite properties. For all these sections, the (positive) material direction 3 consistently points towards the inside of the cross-section, as shown by the red material axis in Figure 4.6 (left). As shown from the composite stack up of the indicated section, the reference plane is on the outside surface of the cross-section. This is clear from matching the corresponding material axis 3. Ply 1 is therefore on the outside surface of the cross-section and the bottom integration point is the outermost location where strain is computed. The strain in the 1-direction is computed since it corresponds to the longitudinal strain. The specific strain chosen is not so important as long as the same strain is extracted for the sub-component. One advantage of choosing the outermost strain, however, is that selecting layer-1 bottom is consistently the outermost strain across all sections and so it prevents any potential mismatch. Finally, the strain at load level 20% of the full magnitude was chosen to be extracted for comparison with the strain distribution from the sub-component. This is chosen because the assessment of the load distribution between full-scale and sub-component is better done at low load levels (in the linear response) in order to prevent any geometric nonlinear effects.

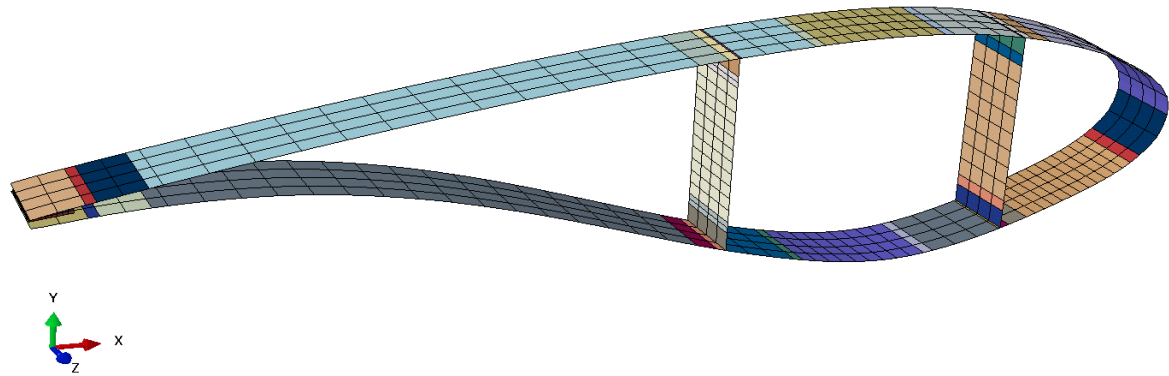


**Figure 4.5:** Cross-section between  $z=14$  m and  $z=14.2$  m colored by sections (each having different layup and materials defined).

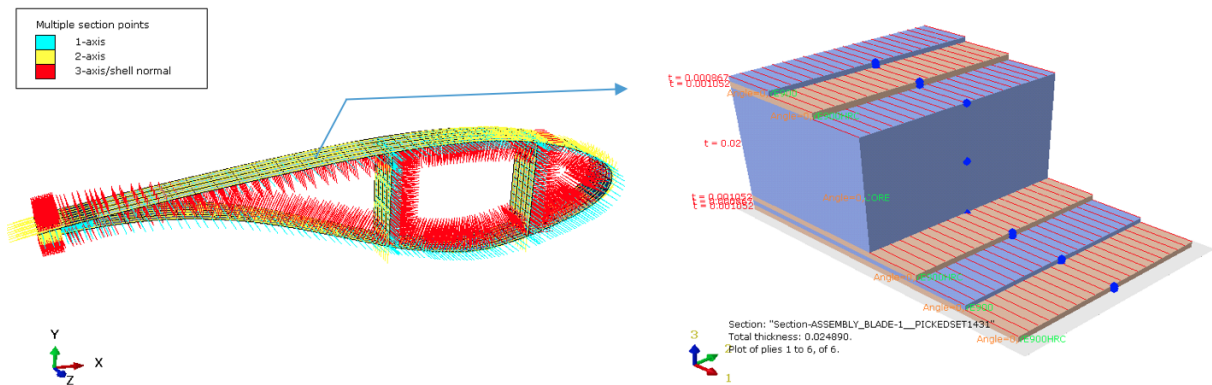


**Figure 4.6:** On the left, cross-section between  $z=14$  m and  $z=14.2$  m showing the material axis definition. On the right, the lay-up for the top section as shown from the arrow. The reference plane is shown by the grey surface and the blue points are the integration points (3 per ply).

It is worth mentioning how strain is computed at the nodes following the path. It is well known that in the finite-element method, displacement is computed at each node while strain is computed at Gaussian points within the element. The strains found at the nodes making up the path are therefore extrapolated from the values at the Gaussian points. This situation is slightly more complex when a node falls at the intersection of two or more sections (with different composite properties and therefore stiffness values). By default, Abaqus extrapolates the strains to a central node that intersects two or more sections, separately, as shown in Figure 4.7a [42]. It therefore takes the average across elements but only if they fall under the same section. This results in two or more different strains values for the central node in this example. When the option called “Use Section Boundaries” is turned off (see Figure 4.7b), Abaqus also takes the average across different sections and so it can be thought of as taking the average of those multiple strain values at the central node. This gives one final strain result at that node.

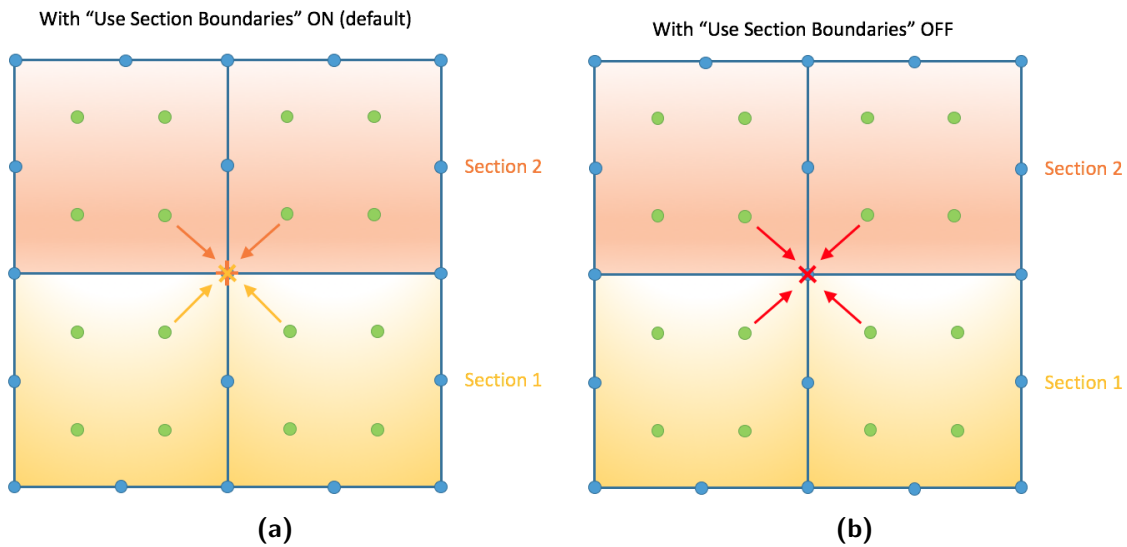


**Figure 4.7:** a) Four 8-noded elements in which two elements are from one section while the other two are from another section. The nodes are represented by the blue dots while the Gaussian points are represented by the Green dots. a) The default case in which the strains are extrapolated to the central node separately in both sections, giving two different strain values at the central node. b) The case in which the option section boundary is turned off. This allows the strain value of the central node to be averaged between the strains computed at Gaussian points from different sections, therefore resulting in one strain value at the central node.

Whether the Section Boundary is turned on or off can have quite a large outcome on the raw results extracted from Abaqus. For example, Figure 4.8 shows the difference in strain results with this option turned on or off. This is taken at  $Z=14\text{ m}$  which is an example of a worst case scenario since nodes on the path are surrounded by elements of 4 different sections (Figure 4.9).

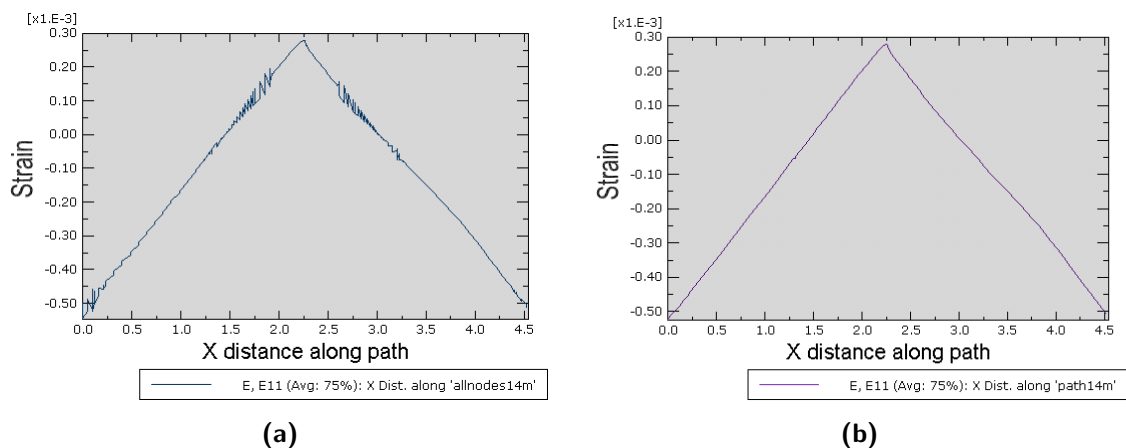


**Figure 4.8:** a) Longitudinal strain at 20% load along the path at  $z=14\text{ m}$  vs.  $x$ -location, with section boundary turned ON. b) Longitudinal strain at 20% load along the path at  $z=14\text{ m}$  vs.  $x$ -location, with section boundary turned OFF.

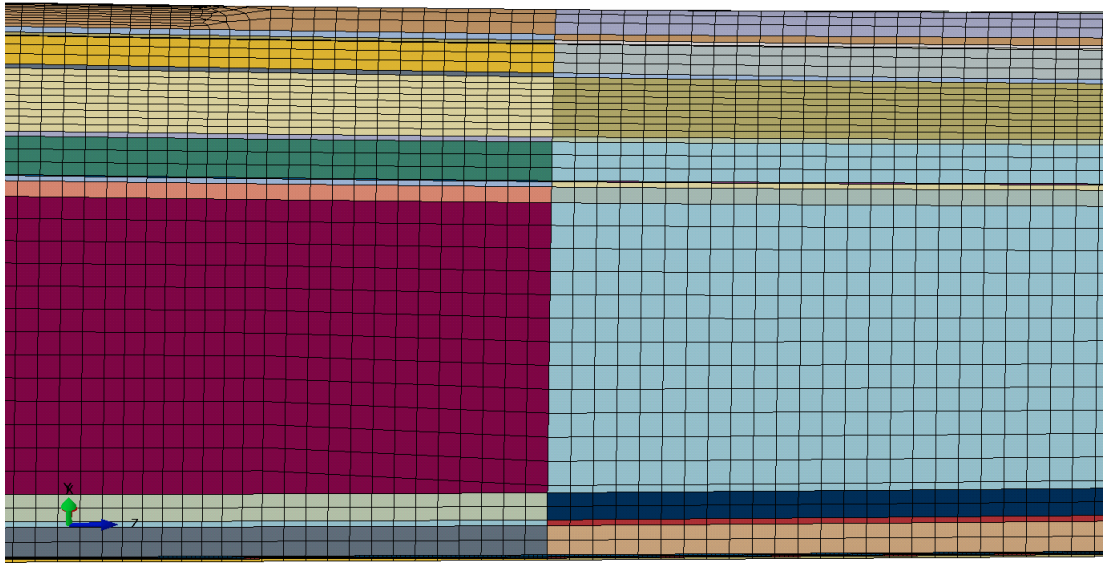


**Figure 4.9:** Pressure side of the blade showing the different sections. Each sections has its own layup and material defined. The transition shown in the z direction occurs at  $z=14$  m.

While turning the “Section Boundary” option OFF appears like an adequate method to obtain averaged strain results, the strains were also manually averaged to verify that Abaqus processed the results as expected. For the cross-sections that do not appear right in between two different sections in the z-direction, so cases other than the situation at  $z=14$  m for example, the two strains obtained at single nodes were manually averaged. When the cross-section does happen to be at the intersection of different sections along the blade length, then the strains were found at paths 0.05 m before and 0.05 m after the intended cross-section, and the results were then averaged to find the strains between the two paths (and this is done after averaging the averaging the two strain results appearing at some of the single nodes in each individual path). For example, the strains were found at  $z=13.95$  m and at  $z=14.05$  m, and when two strains were given at a particular node then these were first averaged. The strains at on those two paths were then averaged in order to find the strains at  $z=14$  m.

## 4.3 Results

### 4.3.1 Global Deformation and Longitudinal Strain Field.

The deformation field under 100% load is shown in Figure 4.10 while its associated longitudinal strain on the outermost ply is shown in Figure 4.11. Both figures also display the undeformed shape, in grey. The deformation field looks quite reasonable. The strain is in tension at the leading edge and in compression on the trailing edge, with the highest magnitude being close to the root, as expected.

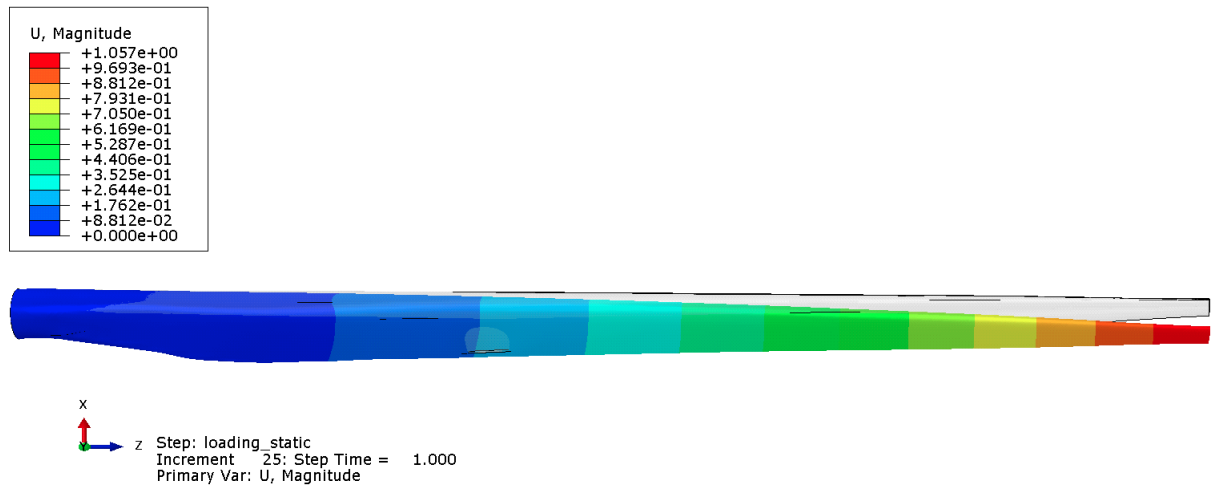


**Figure 4.10:** Deformation field under 100% LTT loading. The undeformed blade is shown in grey.

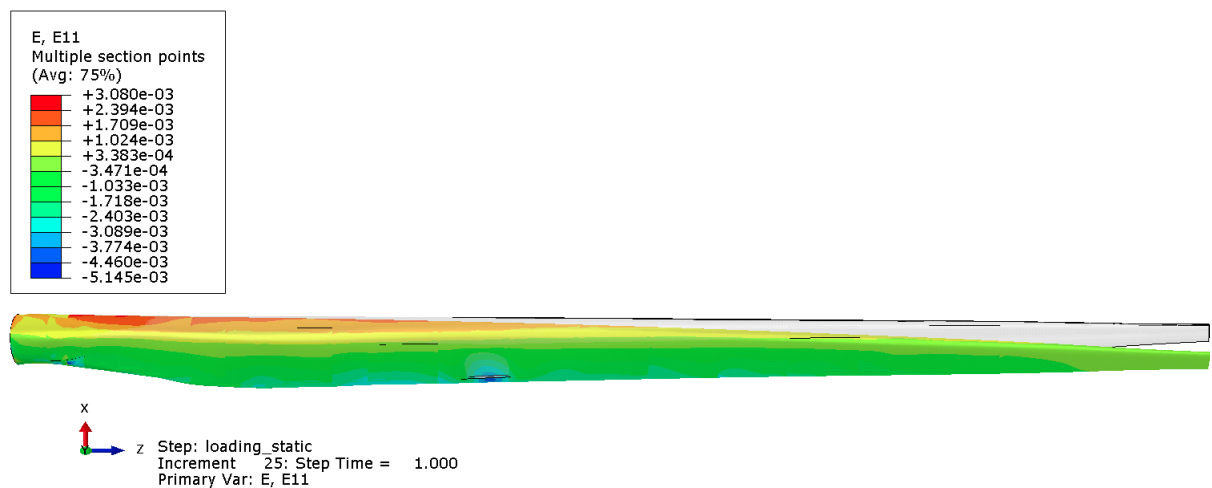


**Figure 4.11:** The longitudinal strain field (E11) on the outermost ply and outermost integration point (Ply-1 bottom) under 100% LTT loading. The undeformed blade is shown in grey.

### 4.3.2 Results Between Automatic and Manual Averaging of Strain

As mentioned in Section 4.2, the longitudinal strain values at nodes intersecting one or more sections was either averaged automatically within Abaqus by turning off the Section Boundary option or the more than one strain values extracted at those nodes were manually averaged. The results from both methods are compared at cross-sections 14 m, 18 m and 24 m in Figure 4.12, Figure 4.13 and Figure 4.14, respectively. The results show that there is an extremely good match in strains between the two methods at  $z=14$  m. However, the results between the two methods at  $z=18$  m and  $z=24$  m appear to differ slightly at the trailing edge. A few points from the automatic method appears to be slightly off. For example, there appears to be a discontinuity on Figure 4.13, near the

trailing edge because when following the path starting at the trailing edge on the suction side, the strain goes down and up again (see 3rd data point). This very unexpected dip suggests that the automatic averaging by Abaqus seems less robust than manual averaging. It is worth pointing out that these three cross-sections happen to be between different sections in the z-directions (as was represented in Figure 4.9), hence it can be seen as a worst case scenario since the averaging is done over the most strain results. A comparison done at three cross-sections that do not fall between two sections in the z-direction actually showed a perfect match between the two methods up to 5 significant figures. One likely cause for the difference in strain results between the two methods at 14 m, 18 m and 24 m is that for those sections, the strains were manually averaged from paths 5 cm before and after this cross-section and so the averaging was done over different nodes for these cross-sections while Abaqus automatically averages the strain from the Gaussian points that fall right around the intended cross-section. For other paths that do not fall at the intersection of different sections in the z-direction, the strains that are manually averaged only come from the Gaussian points around the desired points, hence this is probably the reason why the match is much better.

In conclusion, the automatic averaging method (from surrounding Gaussian points) performs more poorly than manually averaging (from surrounding nodes) in instance where the nodes fall between 4 different sections. No difference can be seen when nodes fall between 2 sections only because, in this case, the manual averaging also only considers nearby Gaussian points and so the method is essentially the same. Since the results of this section are from paths in which certain nodes fall between 4 different sections, the manually averaged strain results are used for the remaining of the section. It is still important to note how small the differences are in retrospect. The worst case difference is at around 1.5% difference and so choosing the strains from one method over the other do not drastically change the upcoming analyses.

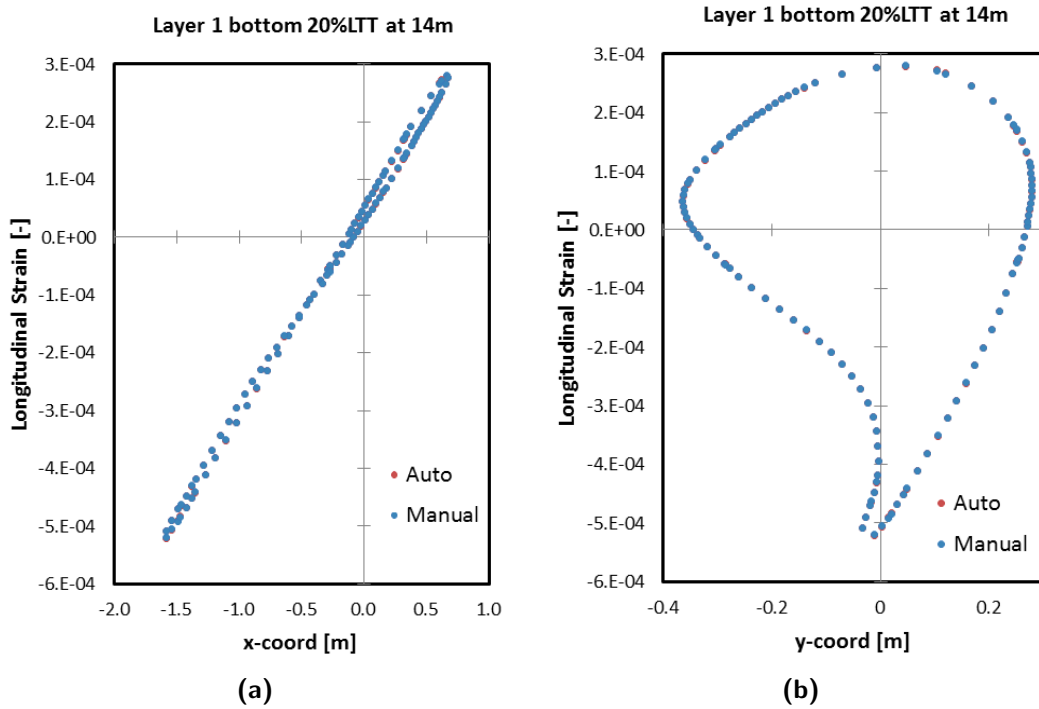


**Figure 4.12:** a) Longitudinal strain at 20% load along the path at  $z=14$  m vs.  $x$ -coordinate.  
b) Longitudinal strain at 20% load along the path at  $z=14$  m vs.  $y$ -coordinate.

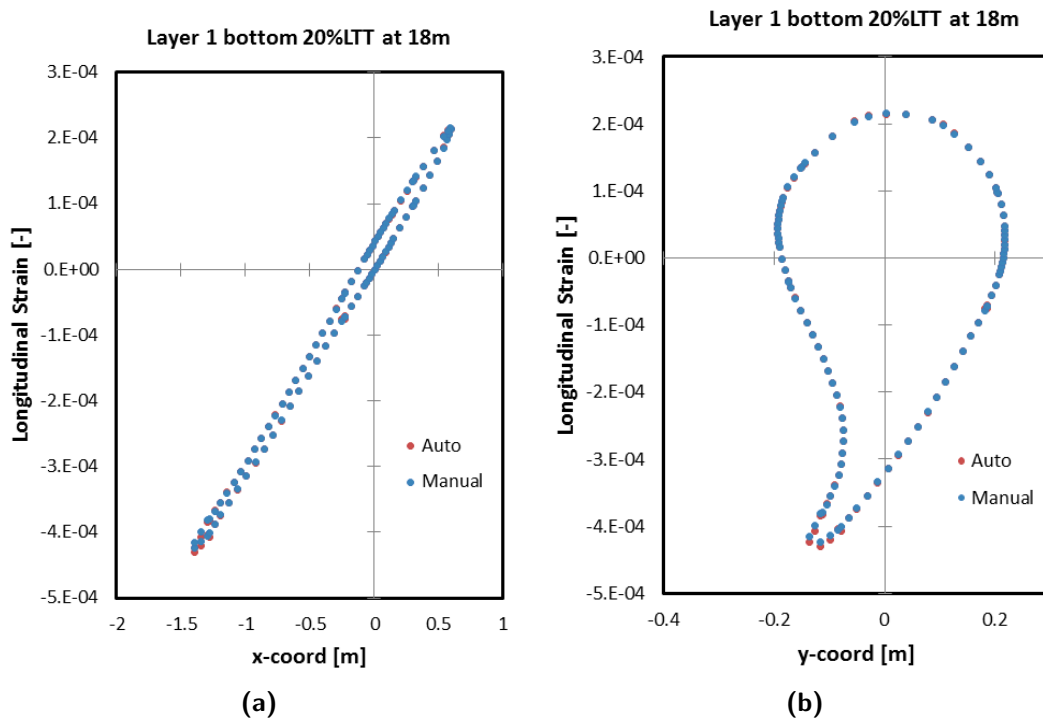


**Figure 4.13:** a) Longitudinal strain at 20% load along the path at  $z=18$  m vs.  $x$ -coordinate.  
b) Longitudinal strain at 20% load along the path at  $z=18$  m vs.  $y$ -coordinate.

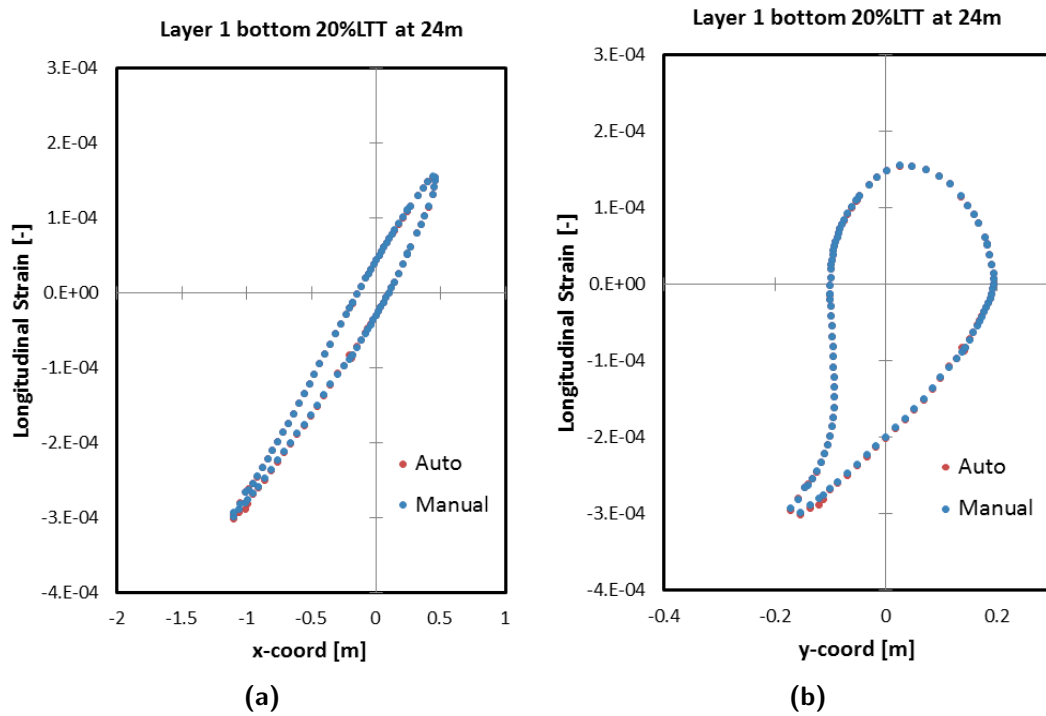


**Figure 4.14:** a) Longitudinal strain at 20% load along the path at  $z=24$  m vs.  $x$ -coordinate.  
 b) Longitudinal strain at 20% load along the path at  $z=24$  m vs.  $y$ -coordinate.

### 4.3.3 Longitudinal Strain vs. Z-Location

Figure 4.15, demonstrates the strains results at the three cross-sections analyzed in a single plot. Two important behaviors can be assessed from this figure. First, there is a clear decrease in strain magnitude as the cross-sections is taken farther out to the tip. This is in agreement with the strain contour plot shown in Figure 4.11 and what is expected from this load case. Second, there is a clear transition from a purely edgewise load case to a combined edgewise and flapwise load case as the cross-section is taken closer to the blade tip. This can be clearly seen in plot b) where the chordline becomes oriented away from the  $y$ -axis and also in plot a) from the ovalisation that occurs for the smaller cross-sections. The ovalisation effectively shows that the strains on the pressure side and suction sides are different, therefore indicating that a flapwise bending moment is also exerted on the section. The observation of combined loading can be attributed to exerting the external forces on the blade purely in the  $-x$  global direction on a blade that has a small amount of twist. This has the consequence of pointing the trailing edge increasingly away from the  $-x$  global direction from root to tip.

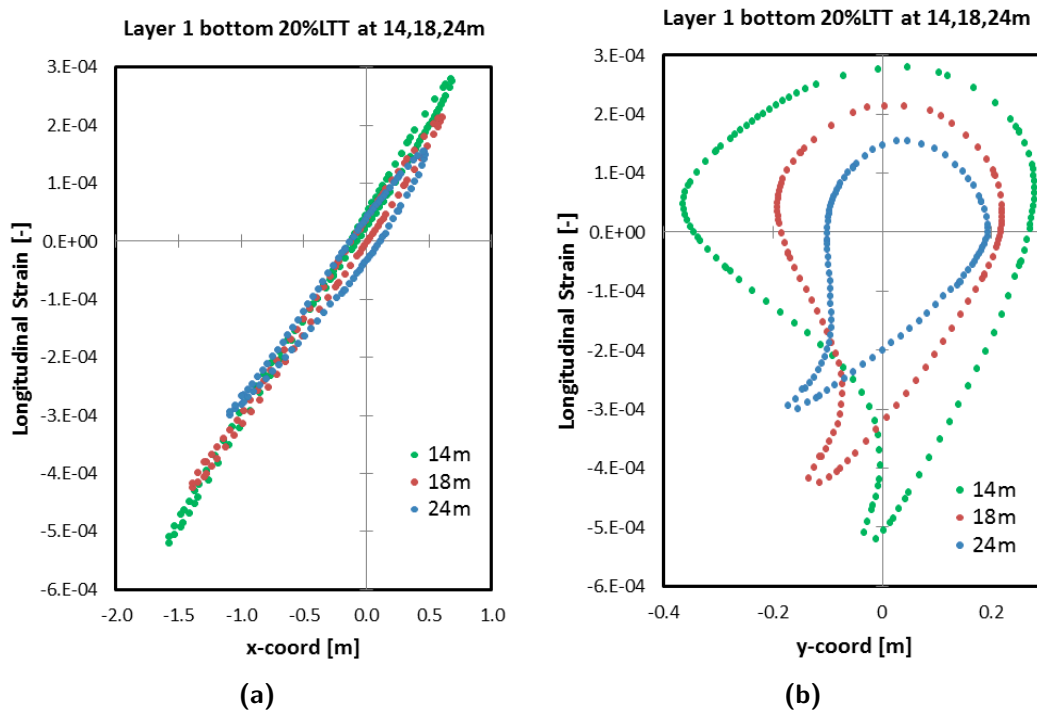


**Figure 4.15:** a) Manually averaged longitudinal strain at 20% load along the paths at  $z=14$  m,  $z=18$  m,  $z=24$  m vs. x-coordinate. b) Manually averaged longitudinal strain at 20% load along the paths at  $z=14$  m,  $z=18$  m,  $z=24$  m vs. y-coordinate.

#### 4.3.4 Longitudinal Strain vs. Load Levels

The analysis in this section considers the strain output under 20% of the full LTT load in order to prevent any nonlinear effects such as buckling or the Brazier Effect for example. Figure 4.16 shows a comparison of the longitudinal strain at  $z=14$  m between 20% load and 100% load. The strain magnitude is seen to be much greater under 100% load, however, it is difficult to assess the difference in distribution. For better comparison, the strain magnitude of the 100% loading was scaled down by a factor of 5. The outcome is portrayed in Figure 4.17. The strain distribution is seen to be slightly out of shape under 100% loading, especially at the trailing edge on the suction side where a small kink is located. This observation demonstrates that using a smaller load like 20% LTT is a more sound approach than using a higher load in order to factor out any nonlinear effect in the upcoming comparison of load distribution with the sub-component approach.

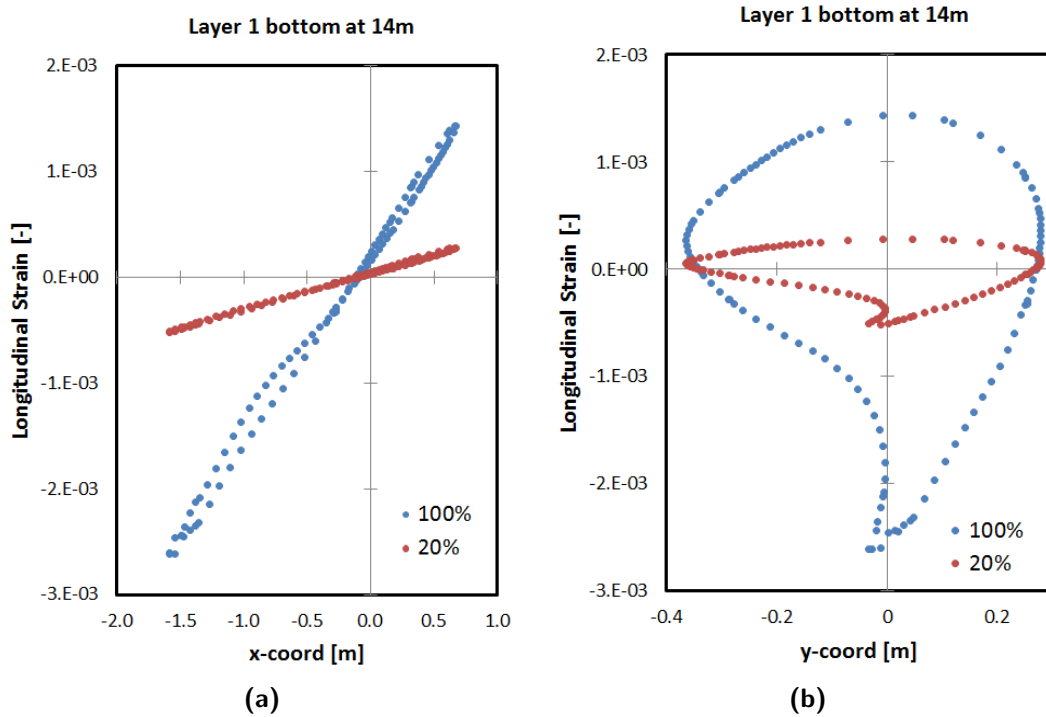


**Figure 4.16:** a) Automatically averaged longitudinal strain along the path at cross-section  $z=14$  m, under 20% and 100% LTT loading vs.  $x$ -coordinate. b) Automatically averaged longitudinal strain along the path at cross-section  $z=14$  m, under 20% and 100% LTT loading vs.  $y$ -coordinate.

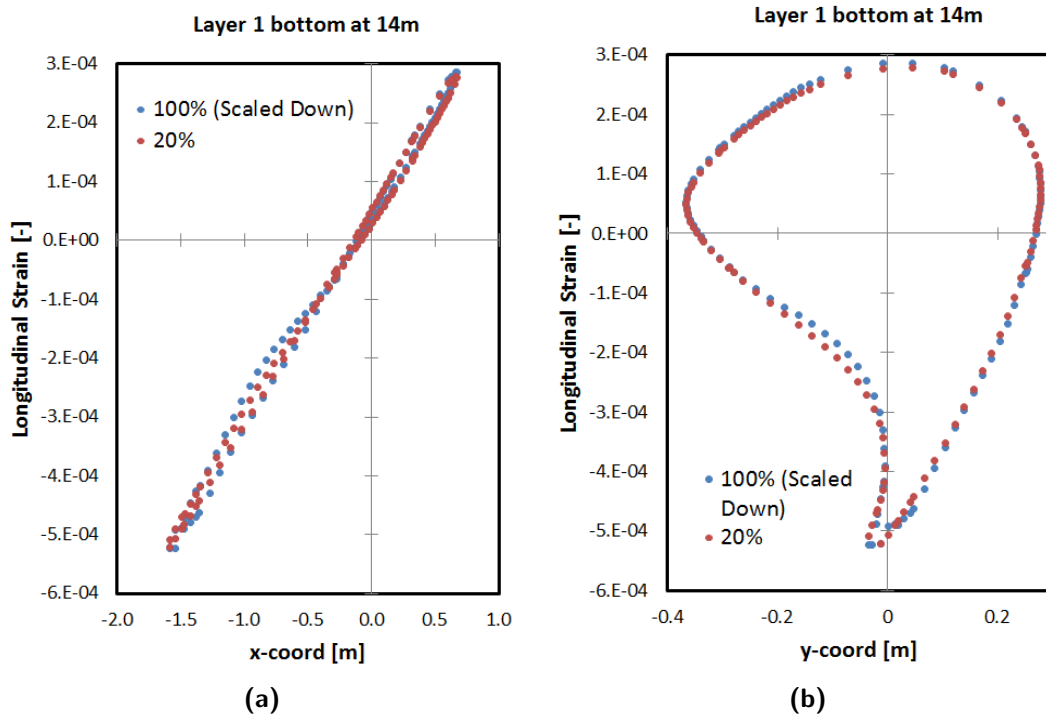


**Figure 4.17:** a) Automatically averaged longitudinal strain along the path at cross-section  $z=14$  m, under 20% and scaled-down 100% LTT loading vs.  $x$ -coordinate. b) Automatically averaged longitudinal strain along the path at cross-section  $z=14$  m, under 20% and scaled-down 100% LTT loading vs.  $y$ -coordinate.

#### 4.3.5 Verification of Results With a Different Model

The strain results were compared with the results obtained by another model of the same blade. This model was created by a researcher from IWES Fraunhofer, Malo Rosemeier, with the finite-element package ANSYS. The comparison was made at cross-sections of  $z=14$  m,  $z=18$  m and  $z=24$  m and can be seen in Figure 4.18, Figure 4.19 and Figure 4.20, respectively. Note that the results from ANSYS come from a fully linear simulation and the results shown are simply the strain results under 100% load divided by 5. The results are seen to match very well. The small differences are likely due to minor differences in the modeling of the blade. Hence, this comparison provides an increased assurance that the results are not affected by significant simulation mistake by the author the present work or from any weaknesses in the Abaqus model.

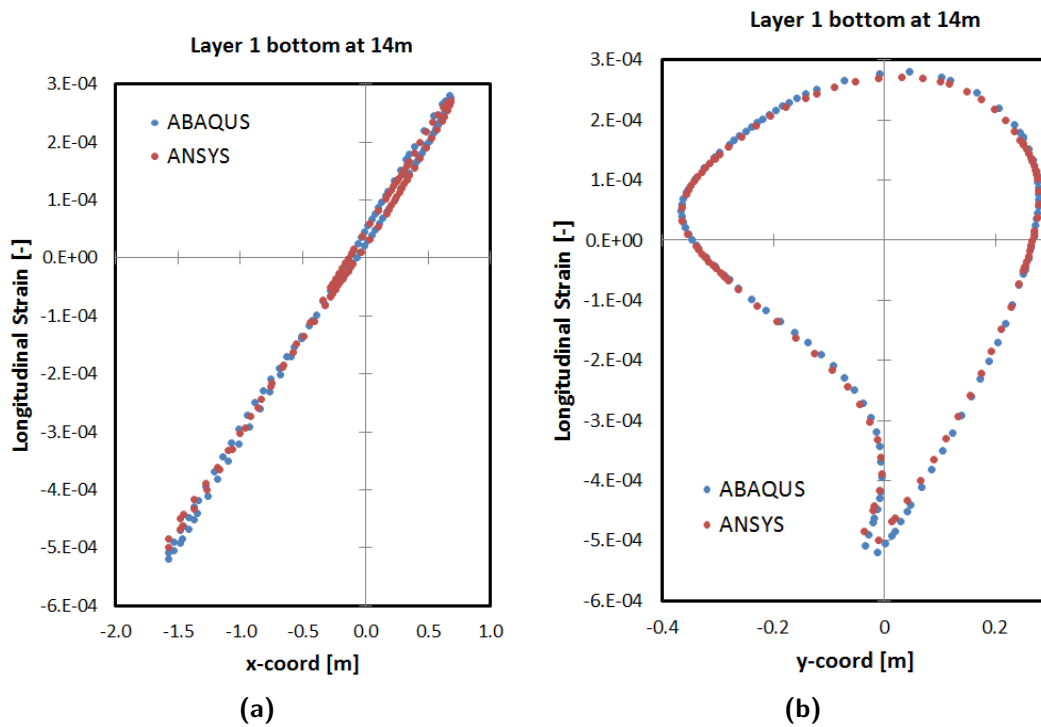


**Figure 4.18:** a) Automatically averaged longitudinal strain along the path at cross-section  $z=14$  m, under 20% LTT load, from ANSYS and ABAQUS vs.  $x$ -coordinate. b) Automatically averaged longitudinal strain along the path at cross-section  $z=14$  m, under 20% LTT load, from ANSYS and ABAQUS vs.  $y$ -coordinate.

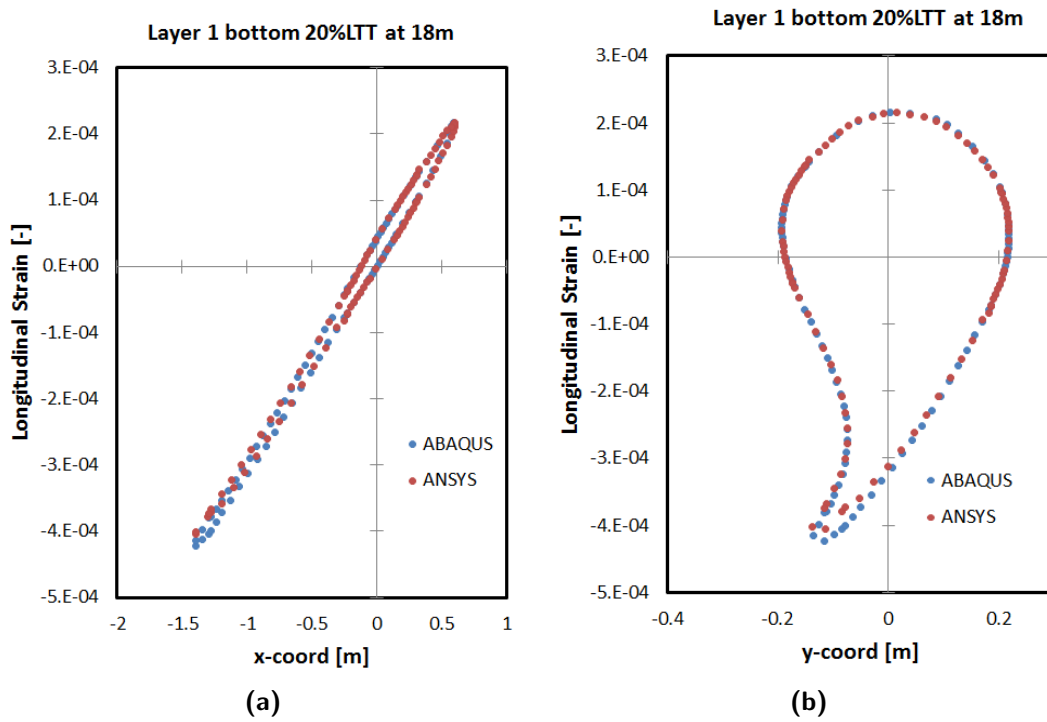


**Figure 4.19:** a) Automatically averaged longitudinal strain along the path at cross-section  $z=18$  m, under 20% LTT load, from ANSYS and ABAQUS vs.  $x$ -coordinate. b) Automatically averaged longitudinal strain along the path at cross-section  $z=18$  m, under 20% LTT load, from ANSYS and ABAQUS vs.  $y$ -coordinate.

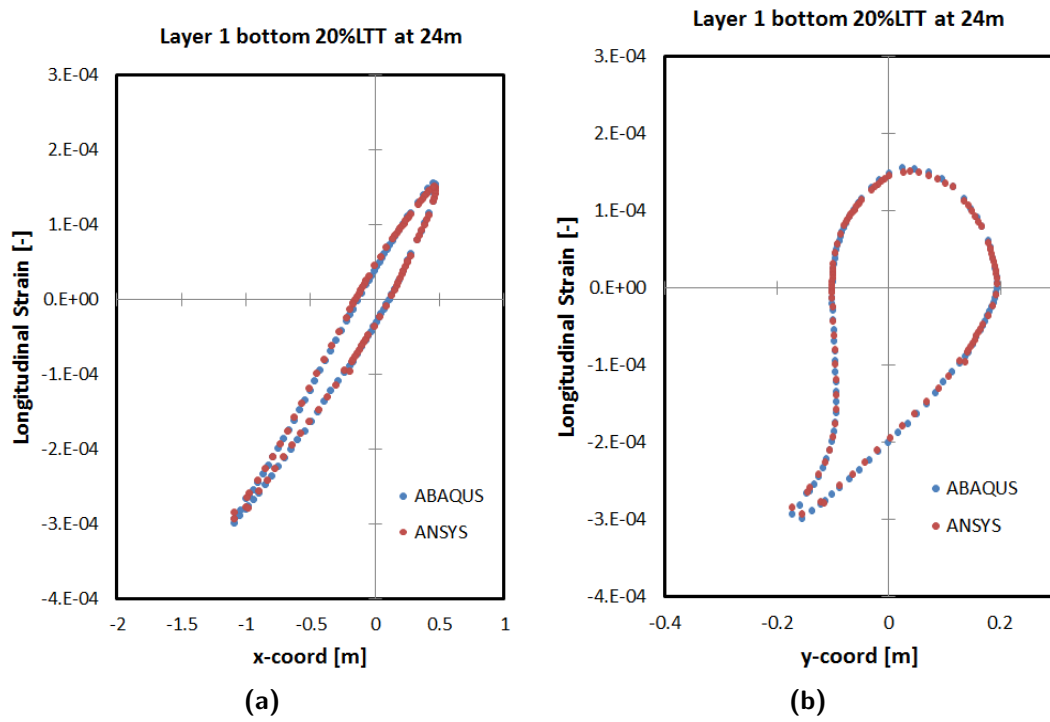


**Figure 4.20:** a) Automatically averaged longitudinal strain along the path at cross-section  $z=24$  m, under 20% LTT load, from ANSYS and ABAQUS vs. x-coordinate. b) Automatically averaged longitudinal strain along the path at cross-section  $z=24$  m, under 20% LTT load, from ANSYS and ABAQUS vs. y-coordinate.



# Comparison of Local Loading Between Full-Scale and Sub-Component

In this chapter, the sub-component modelling methodology from Chapter 3 is applied to three blade sections that are to be tested experimentally with the sub-component test rig at DTU. The longitudinal strain on the cross-section located at the middle of the specimen is compared with the longitudinal strain field at the same cross-section on the full-scale blade, as was demonstrated in Chapter 4. This is to verify that the load introduction in the sub-component is similar to what is seen in the full-scale model.

## 5.1 Description of the Blade Sections

DTU obtained blade sections of 3 m in length from SSP 34m blades at three locations along the blade to be tested experimentally in its sub-component test rig. These locations, as displayed in Figure 5.1, are from 13 to 16 meters, 19.25 to 22.25 meters and 17.9 to 20.9 meters. For convenience, these sections will be referred to in the remaining of the report by their mid cross-section location of 14.5 m, 19.4 m and 20.75 m. These are also the locations where strain will be compared between full-scale and sub-component. Unlike the specimen presented in Chapter 3, these specimens have not been cut in the transversal direction yet. The optimal location of the cut within the cross-section needs to be determined, see Figure 5.2.

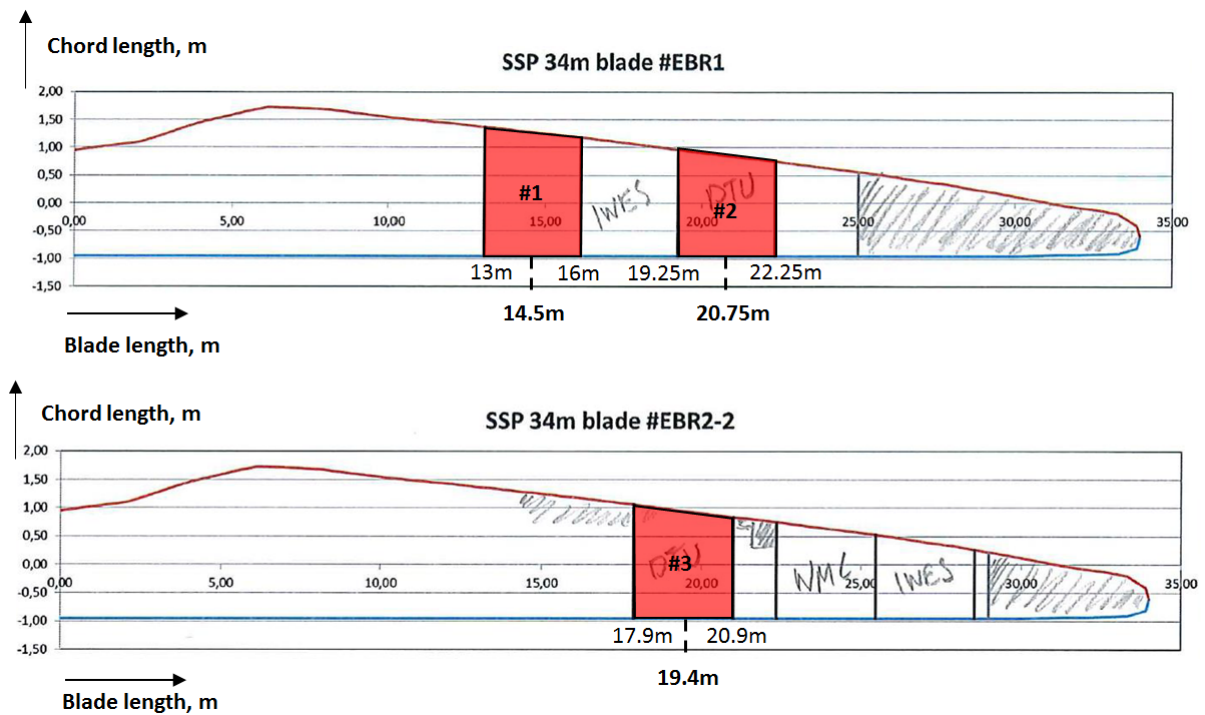


Figure 5.1: The 3 blade sections to be tested experimentally and numerically.

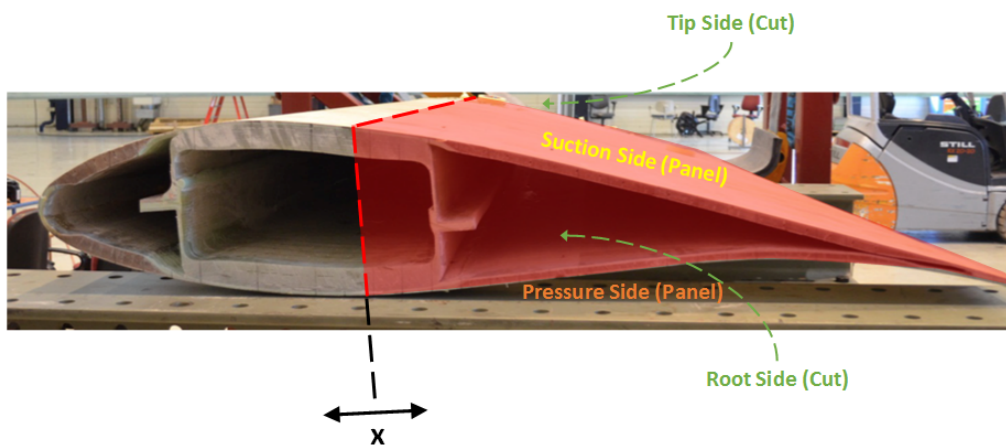


Figure 5.2: Example of one of the blade sections. The transverse cut location needs to be decided.

## 5.2 Methodology of the Transverse Cut

The test rig built by DTU is meant to apply compressive loads only because it is more simple than apply both compressive and tensile loads on a cross-section boundary. The compressive load starts from zero at the hinge line and grows linearly up to the top of the plate. The idea then is to cut the specimen in such a way that its expected zero

strain axis from full-scale LTT loading aligns with the bottom of the test set-up where the compressive strain is zero.

In order to predict where the zero strain axis lies for these sections, the longitudinal strain was extracted at cross-sections located at  $z=14.5$  m, 19.4 m and 20.75 m in the full-scale model under LTT loading, following the same methodology explained in Section 4.2. Both manual averaging and automatic averaging of the strains were done. The results were found to be almost identical, matching up to 4 significant figures. Figure 5.3, Figure 5.4, and Figure 5.5 shows the longitudinal strain from automatic averaging vs.  $x$  and  $y$  coordinates at  $z=14.5$  m, 19.4 m and 20.75 m. The strain vs.  $x$  coordinate plots shows where in the cross-section the strain becomes zero, and the closest data point to this zero strain location is indicated in red, on both pressure and suction sides. The coordinates of those (red) nodes are shown in Table 5.1. The coordinates were then rounded to the nearest centimeter for practicality reasons since the blades will be manually cut.

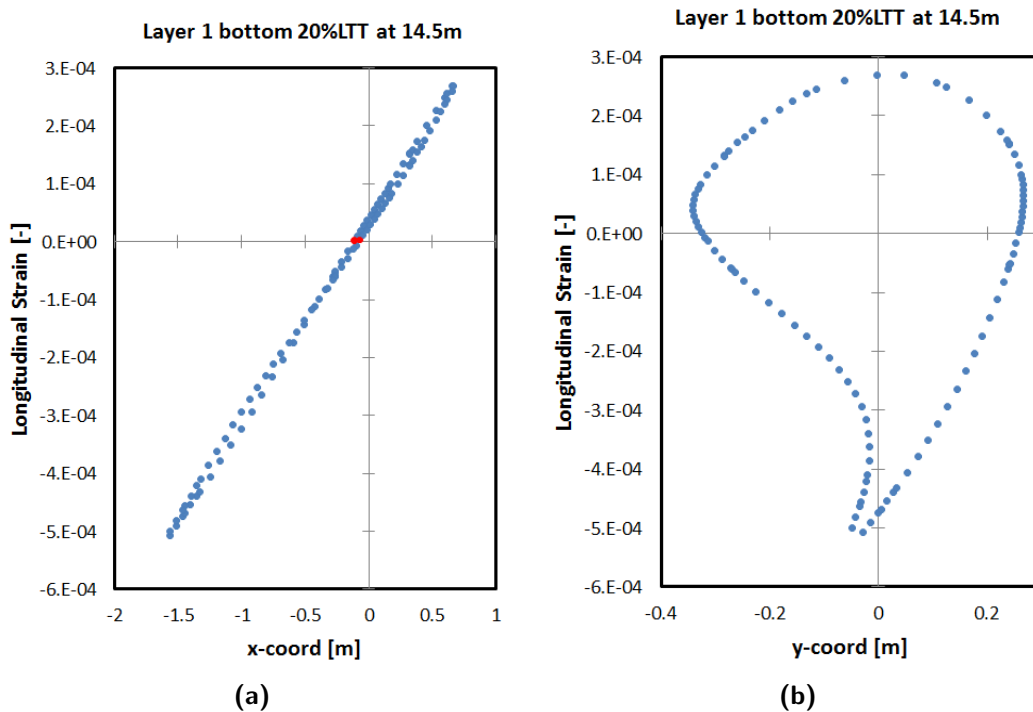


**Figure 5.3:** a) Longitudinal strain at 20% load along the path at  $z=14.5$  m vs.  $x$ -coordinate. The closest points to zero strain on the pressure and suction sides are shown in red. b) Longitudinal strain at 20% load along the path at  $z=14.5$  m vs.  $y$ -coordinate.

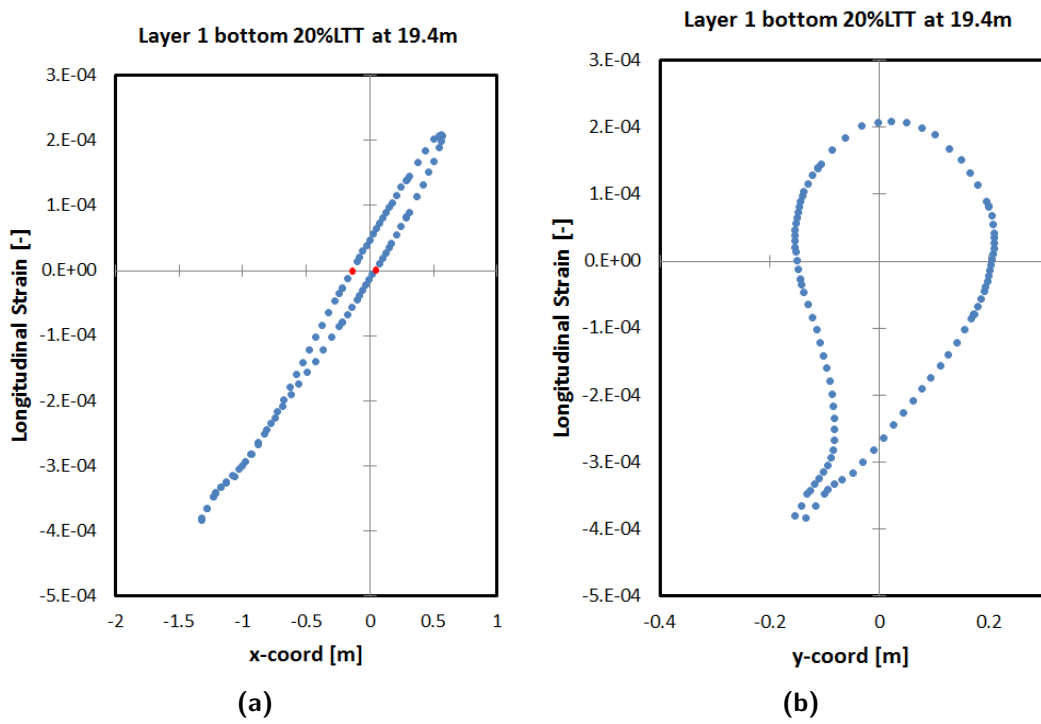


**Figure 5.4:** a) Longitudinal strain at 20% load along the path at  $z=19.4$  m vs.  $x$ -coordinate. The closest points to zero strain on the pressure and suction sides are shown in red. b) Longitudinal strain at 20% load along the path at  $z=19.4$  m vs.  $y$ -coordinate.

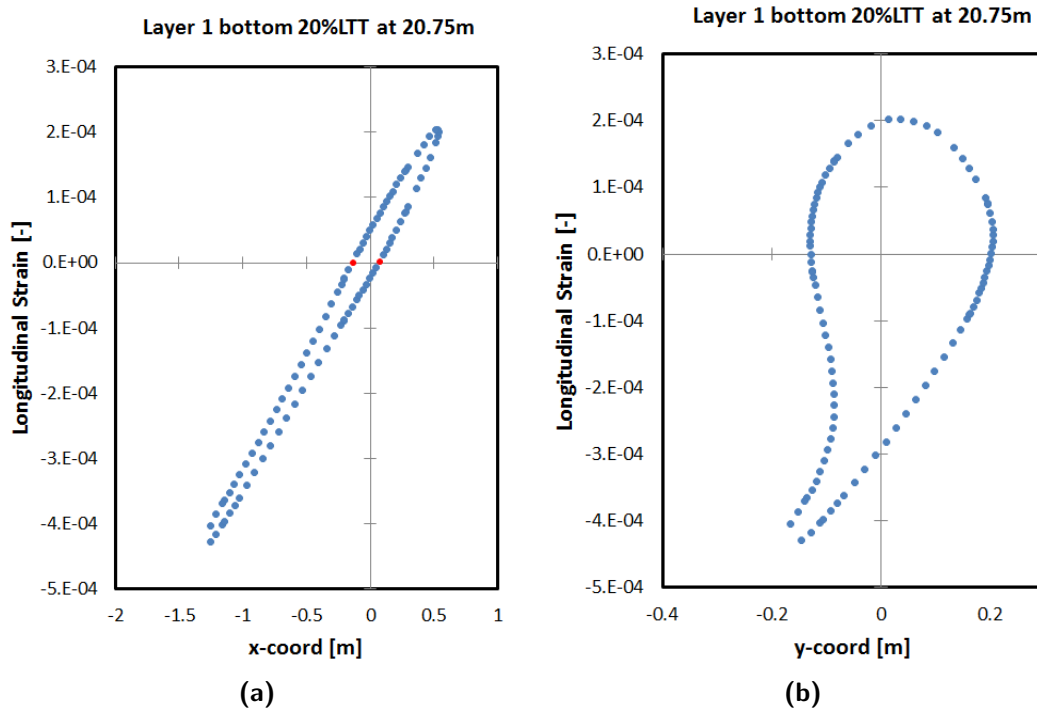


**Figure 5.5:** a) Longitudinal strain at 20% load along the path at  $z=20.75$  m vs. x-coordinate. The closest points to zero strain on the pressure and suction sides are shown in red. b) Longitudinal strain at 20% load along the path at  $z=20.75$  m vs. y-coordinate.

**Table 5.1:** Coordinate of the closest points to strain of zero and rounded values later used in the model.

Section	Pressure Side		Suction Side	
	x-coordinate [cm]; longitudinal strain [-]			
	Real	Approximation	Real	Approximation
14.5	-11.16; $2.23E-06$	-11; 0	-7.10; $2.98E-06$	-7; 0
19.4	-13.10; $-3.52E-07$	-13; 0	4.70; $8.37E-07$	5; 0
20.75	-13.55; $3.69E-07$	-13.5; 0	7.36; $1.48E-06$	7; 0

The blade section models were cut at their respective (rounded) x-coordinate specified in Table 5.1 on the pressure and suction sides through the whole length of the specimen. The cut specimens can be seen in Figure 5.6, Figure 5.7 and Figure 5.8. One big assumption from this method is that it assumes that the computed zero strain location in the middle of the section also hold true along the whole length of the sub-component section. The appropriateness of this assumption was verified by computing the zero strain x-location at  $z=13$  m and  $z=16$  m. The difference was found to be very minor, being less than 1 cm, and is not very significant compared to the accuracy at which the specimens can be cut.

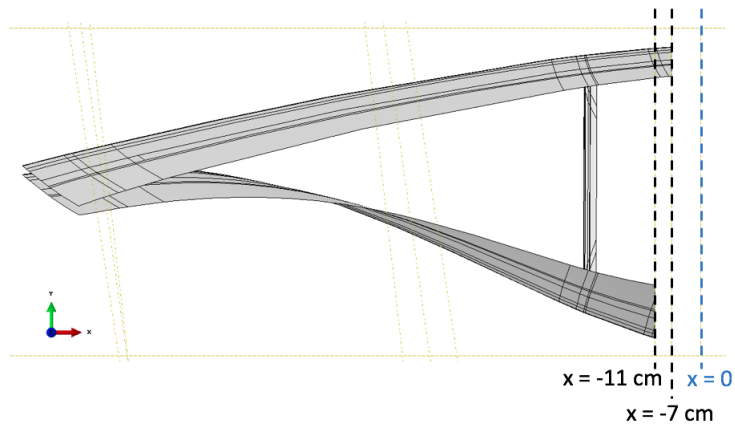


Figure 5.6: Cut 14.5 m section.

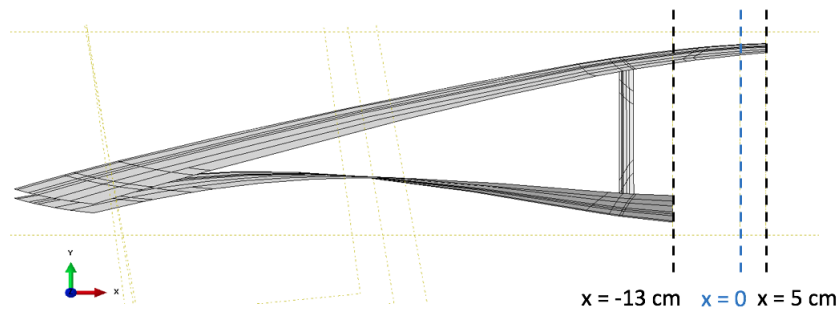


Figure 5.7: Cut 19.4 m section.

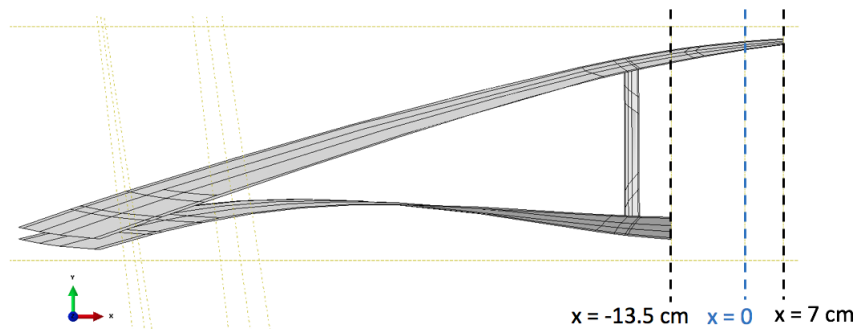


Figure 5.8: Cut 20.75 m section.

### 5.3 Simulation Set-Up

The analysis followed the same modelling approach as explained in Section 3.2, with the exception of the following details:

1. A choice had to be made regarding the characteristic length to use for the shell elements of the sub-component sections. The question is whether it is better to use

a characteristic element size of 4 cm since the mesh convergence study in Chapter 3 showed this element size to give converged results, or if it is better to use a characteristic length of 5 cm so that the strain comparison is done with the full-scale and sub-component models having the same mesh density. The analysis was done using both mesh densities to see how it would affect the results and it turns out that the strain results match up to 3 significant figures. The reason why the results match here but differed slightly in the mesh convergence study is probably because the strains are extracted at a very light load, much lower than the buckling load used in the convergence study. Hence, it was found that it does not matter whether 4 cm or 5 cm characteristic length is used for the strain comparison analysis but it does matter for buckling analyses. Since in this chapter, using 4 or 5 cm does change the results, shell elements having characteristic lengths of 5 cm were chosen in order for the sub-component and full scale models to have the same mesh density.

2. The plate characteristic lengths were kept at 5 cm to be on the same scale as the blade mesh density such as to minimize any interface problems that could arise from having low and high mesh density parts in contact with each other. To reduce computation time, an attempt was made at using rigid shell elements as opposed to 3D hexahedron solid elements in the plates. However, it led to many solver errors or even unwanted displacement at the bottom of the plate. The simulation had to move on and so the 3D solid elements were kept.
3. The way the blade was cut in relation to the already present partitions made it impossible to mesh the whole part with only quadrilateral elements. The Abaqus mesh settings were changed such that it can use triangular elements when necessary.
4. Due to how the blade sections are cut, aligning the plates with the transversal cut leads to the plates not being parallel to each other. This was fixed by making one of the plate be parallel to the other plate. The compromise is that a slight portion of the blade goes past the bottom of the plates. As shown in Figure 5.9, the difference is extremely small however and such small rotation should not affect the results in any significant way since it is much smaller than the angle used in the study of Section 3.5.
5. The plate width was adjusted in order to fully capture the blade sections closer to the tip. A larger width is necessary due to the blade sections being significantly slanted which is a direct causation of how it was cut (See Figure 5.9). The plate widths are 0.8 m, 1.2 m and 1.4 m for the 14.5, 19.4 and 20.75 sections, respectively. Changing the plate width has no direct consequence on the model other than increasing the number of elements in the plate, therefore resulting in slightly longer solving time.
6. The boundary condition at the bottom of the blade sections restricting the x and y motion were removed. A first simulation attempt did include these boundary conditions but it was found to severely affect the strain distribution in the middle section of the specimen near the cut. Hence, it affected the strain comparison negatively and it was deemed unnecessary to keep them. An improved version of the DTU test rig will not feature any contact other than the two large plates inducing the bending moment and so it is adequate to remove these boundary conditions.

7. The applied maximum load on the plates were set to 400 kN for the 14.5 section and 200 kN for both the 19.4 and 20.75 sections. The specific value chosen does not matter so much as long as it is greater than the failure load of the specimen by some margin to capture the full load-displacement history. The same maximum loads are used for the strain comparison analysis and buckling analyses of these sections.

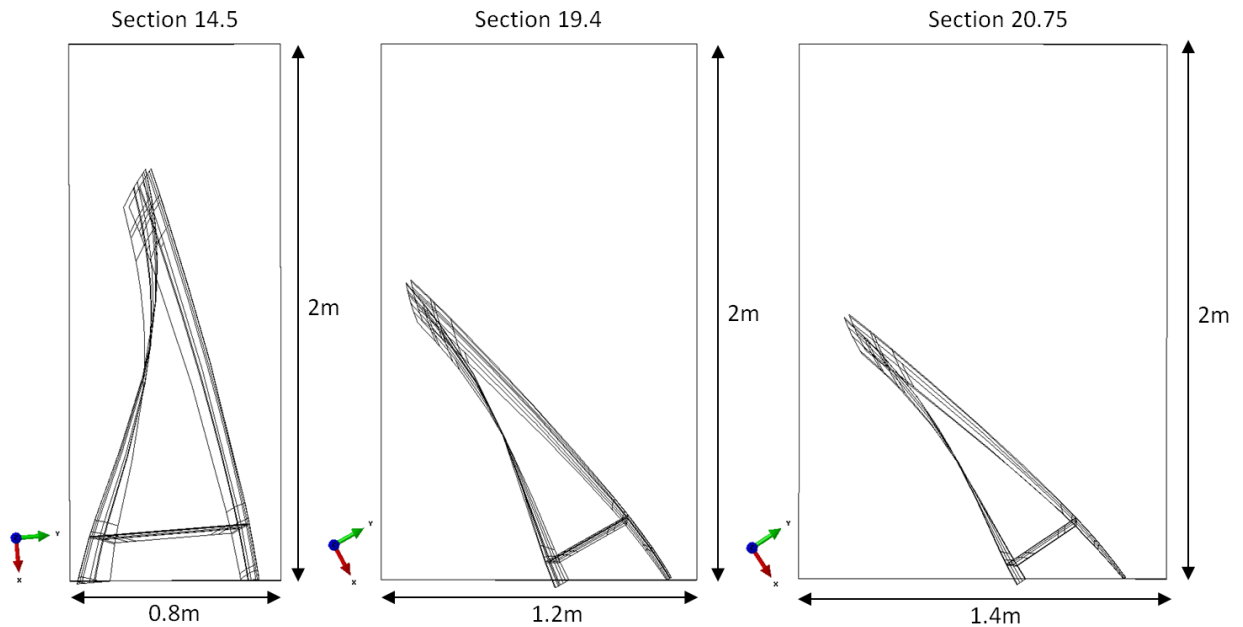


**Figure 5.9:** X-Y view (i.e. side view) of the blade section positioning in-between the two plates.

The mesh properties of the three sections are shown in Table 5.2. The element type STRI65 is a 6-noded triangular shell element and is automatically used by Abaqus as it sees fit in order to obtain a satisfactory mesh.

**Table 5.2:** Mesh details of the 3 blade section assemblies for the strain comparison analysis.

Section	Part	Element Type	Char. Element Size [m]	# Elements	# Nodes
14.5	Composite	S8R	0.05	4,956	15,159
		STR165	0.05	2	
	Glue	C3D8I	0.01	4,800	10,836
		C3D8I	0.05	5,120	6,970
	<b>Total:</b>			14,878	32,965
19.4	Composite	S8R	0.05	4,278	13,099
	Glue	C3D8I	0.01	4,800	10,836
	Plates	C3D8I	0.05	7,680	10,250
	<b>Total:</b>			16,758	34,185
20.75	Composite	S8R	0.05	4,020	12,315
	Glue	C3D8I	0.01	4,800	10,836
	Plates	C3D8I	0.05	8,960	11,890
	<b>Total:</b>			17,780	35,041

The nonlinear static analysis following the Newton-Raphson method was used to compute the strains in this chapter. Since the results are taken at such low load increment, the robustness of the dynamic solver is not needed. The solving time and results file size are therefore minimized. The settings for nonlinear static analysis is the same as presented in Section 3.2.

## 5.4 Results

The longitudinal strain results of the sub-component was extracted on a path located in the center of the specimen. This was done in the same way as the extraction of the longitudinal strain of the full-scale blade (Section 4.2). With the aim of comparing the strain distribution between the full-scale blade and the sub-component, the strain from the sub-component should be extracted at a load level that will yield strain results of the same magnitude as with the full-scale blade magnitude. This load level is not known in advance and so the following method was created and used to approximate this load:

1. Extract the strain at two load percentages of the full load, one that yields strain results with higher magnitude than the strain from the full-scale blade at 20% loading and the other with lower magnitude. Since strain is extracted at every 10% of the full load, the two load levels should follow (i.e 20% and 30%). Use the automatic averaging from Abaqus.
2. Define a scaling factor that makes the average strain between the two trailing edge points (one at the pressure side tip, the other on the suction side tip) be equal between the full-scale and sub-component. It can be expressed in equation form as:

$$\text{Scaling Factor} = \frac{\left[\frac{1}{2}(E_{11,sstip} + E_{11,pstip})\right]_{\text{Sub-Component}}}{\left[\frac{1}{2}(E_{11,sstip} + E_{11,pstip})\right]_{\text{Full-Scale}}} \quad (5.1)$$

3. By using Equation 5.1, find the scaling factors from the lower load level and the higher load level on the sub-component.

4. Multiply the longitudinal strain from each load level by their respective safety factors.

It turns out that for the three sections, the load level percentages 10% and 20% should be used. For the 14.5 section, the maximum applied load is 400 kN and so the two load levels to use are 40 kN and 80 kN. For the other two sections, the maximum applied load on the plates are 200 kN and so the strain is extracted at load levels of 20 kN and 40 kN.

The longitudinal strain from the sub-component were also matched with the strains from the full-scale blade under 10% LTT load, in order to see whether the match is better at a lower load level.

A comparison of the scaled longitudinal strain results for the 14.5 section and full-scale blade is shown in Figure 5.10 for 10% LTT load and in Figure 5.11 for 20% LTT load. The results show that scaling from the lower or high load level turns out not to influence the results. This suggests that the response of the sub-component structure under these low load levels is highly linear. The match is almost identical at 10% and 20% LTT load for this section. The fit is generally quite close, with the strain magnitudes being slightly lower than the strain on the full-scale blade on the pressure side and slightly higher on the suction side. It is interesting to note that the sub-component sees some slight tension at the zero strain axis from the bending of the specimen.

In order to quantify the strain difference, a spline curve fit was applied through the strain data from both sub-component and full-scale. The strain difference in this analysis was decided to be computed for 20% LTT and for the sub-component strain at 80 kN. The difference between the results from 10% LTT and 20% LTT, and 40 kN and 80 kN is so small that it does not matter which is chosen. The fit through the data point is shown in Figure 5.12a for the 14.5 section where longitudinal strain is plotted against distance along the path starting on the suction side tip and ending on the pressure side tip. The strain was then extracted at 2 cm intervals on both curve fits, as shown in Figure 5.12b. This then allows the comparison of the strain results at identical distances along the path. The absolute difference is shown in Figure 5.13a. A negative absolute difference means that the sub-component strain is more negative (therefore more compressive) than the full-scale strain. The location along the path where no comparison can be made is left blank. The relative difference was then calculated using the formula

$$\text{Rel. diff. [\%]} = \frac{E_{11,sub} - E_{11,full}}{E_{11,full}} \quad (5.2)$$

along the path. This gives the curve shown in Figure 5.13b for the 14.5 section. This formulation has the weakness of having the relative difference go up dramatically when the denominator is very small, meaning that the strain values are very small. To mitigate this problem, the relative difference was calculated once more in what we call the adjusted relative difference from the formula:

$$\text{Adj. Rel. diff. [\%]} = \frac{E_{11,sub} - E_{11,full}}{[E_{11,full}]_{\text{high}}} \quad (5.3)$$

where  $[E_{11,full}]_{high}$  is a high magnitude strain value that is used for the relative difference calculation along the the whole path. For the 14.5 section, the most compressive strain along the path was used (i.e at 0.28 m). This means that the relative difference at 0.28 m is the same on both the original and the adjusted relative different diagram. A positive relative difference means that the sub-component strain has higher magnitude than full-scale strain. Figure 5.13c shows that the relative strain difference along the path for the 14.5 section stays below 6.5% suggesting a very good match.

### 14.5 Section

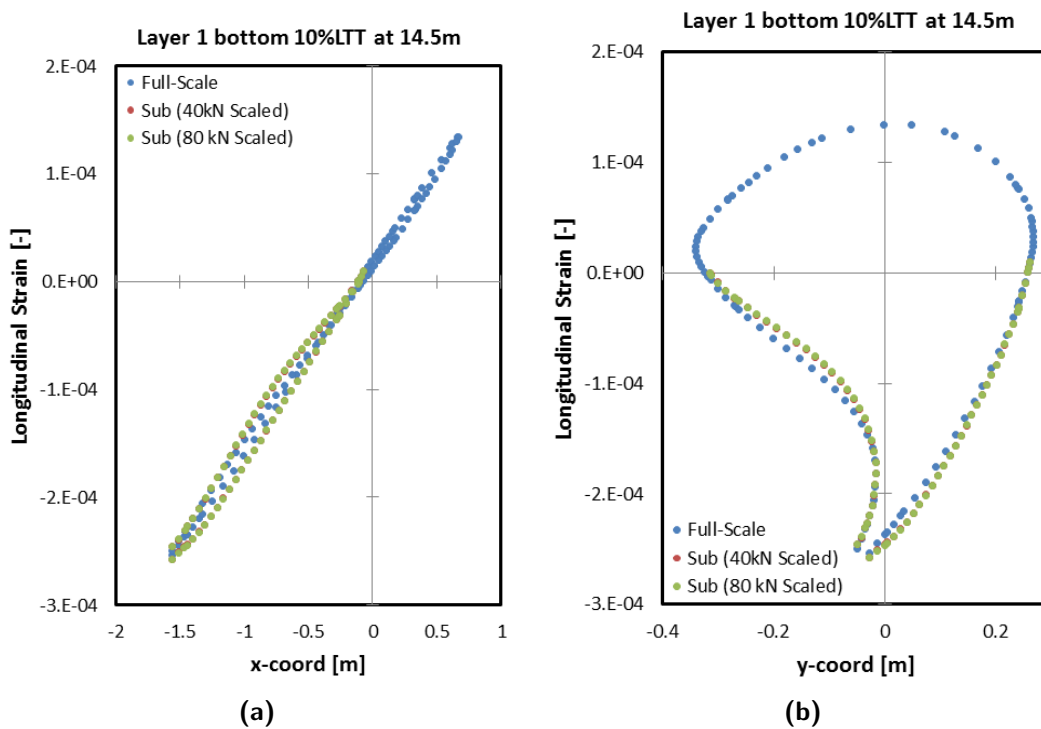


**Figure 5.10:** a) Longitudinal strain at 10% load along the path at  $z=14.5$  m vs. x-coordinate for full-scale blade and sub-component section, the latter scaled from both 40 kN and 80 kN. b) Same strain results vs. y-coordinate.

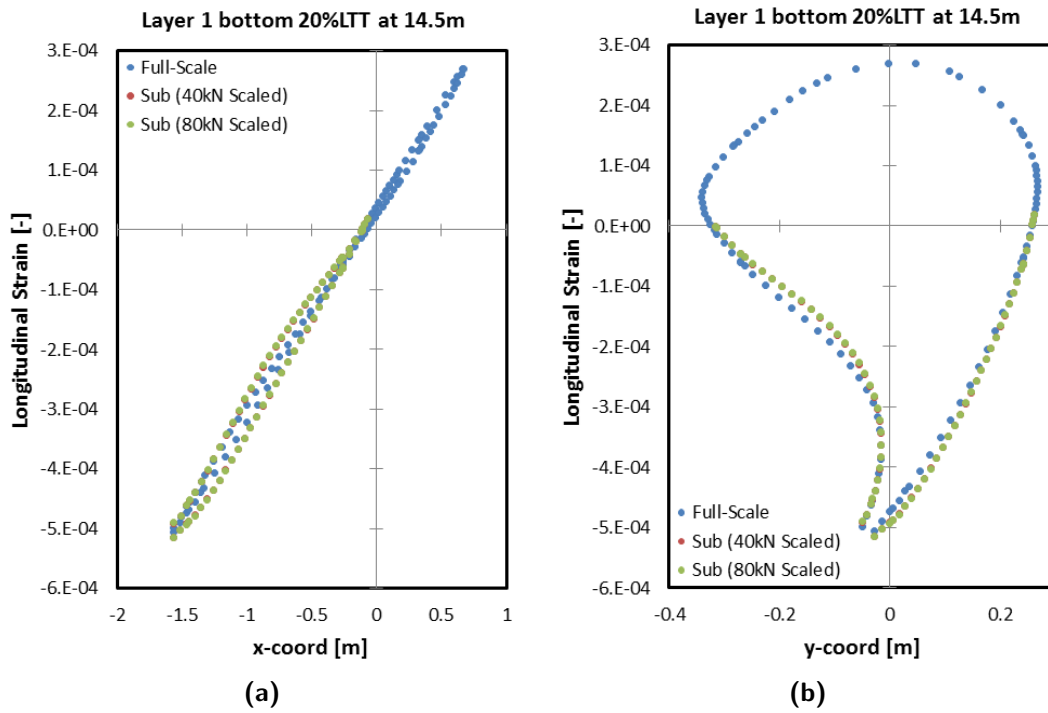


Figure 5.11: a) Longitudinal strain at 20% load along the path at  $z=14.5\text{m}$  vs. x-coordinate for full-scale blade and sub-component section, the latter scaled from both 40 kN and 80 kN. b) Same strain results vs. y-coordinate.

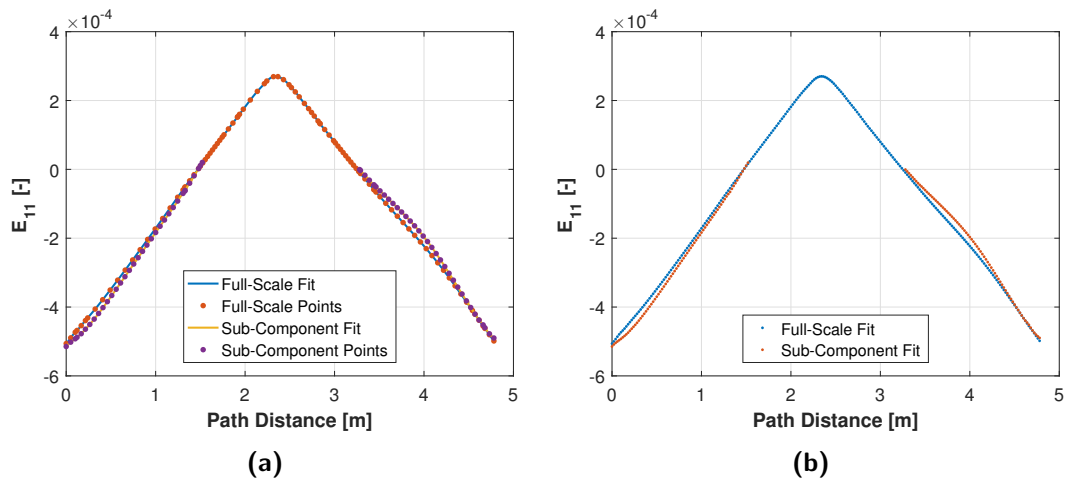
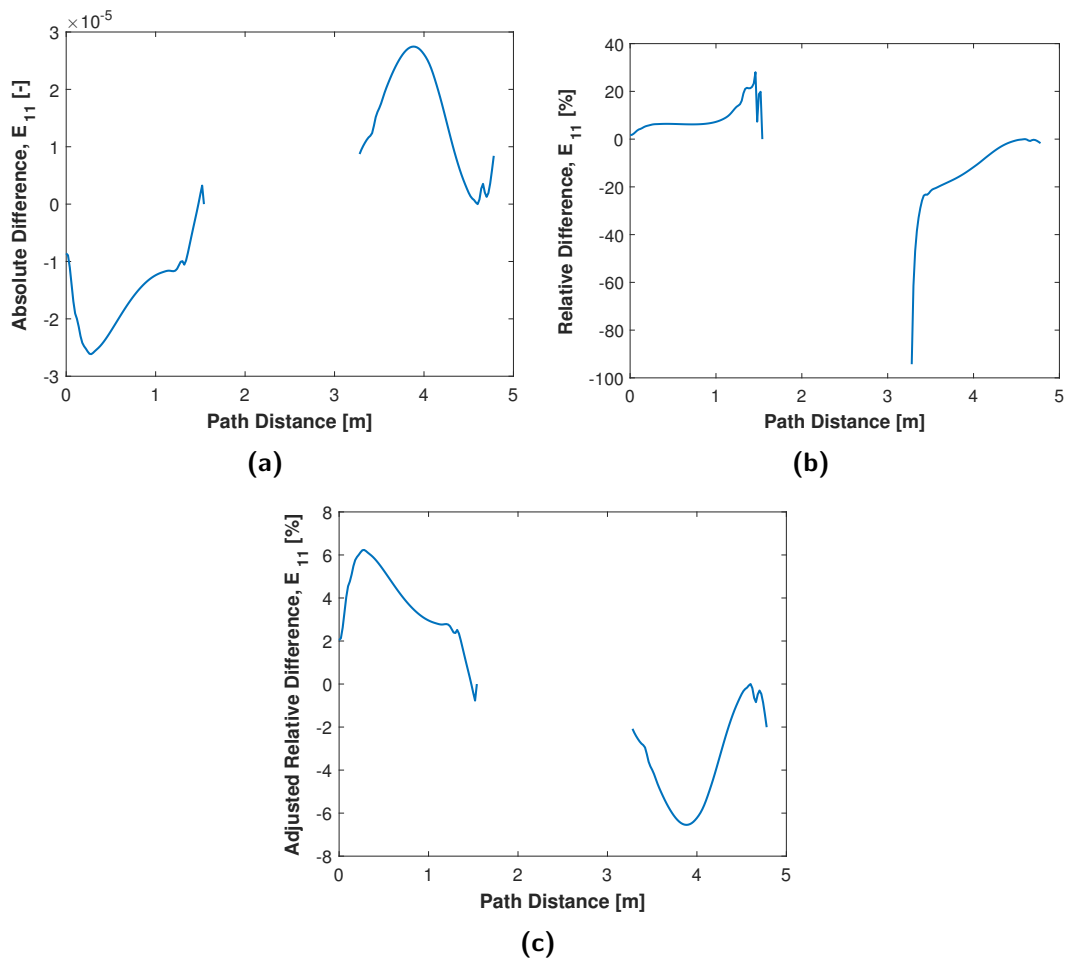


Figure 5.12: a) Spline fit through longitudinal strain data points at 20% load along the path at  $z=14.5\text{m}$  for full-scale blade and sub-component section scaled from 80 kN b) Points generated on the curve fit at constant interval of 2 cm.



**Figure 5.13:** The results are for the path at  $z=14.5$  m a) Absolute longitudinal strain difference between full-scale blade and sub-component. b) Relative difference between longitudinal strain of full-scale blade and sub-component. c) Adjusted relative difference between longitudinal strain of full-scale blade and sub-component.

## 19.4 Section

The strain results for the 19.4 sub-component section is shown here. A comparison of Figure 5.14 and Figure 5.15 shows that the match is better under 20% LTT loading. The results in Figures 5.16 and 5.17 were therefore calculated for 20% LTT. The scaled sub-component strain from 20 kN and 40 kN also appear identical and the one from 40 kN was chosen for the relative difference analysis. The adjusted relative difference graph was made based on the maximum strain at 0.64 m. The relative difference for this section is below 10% and this suggests a good match.

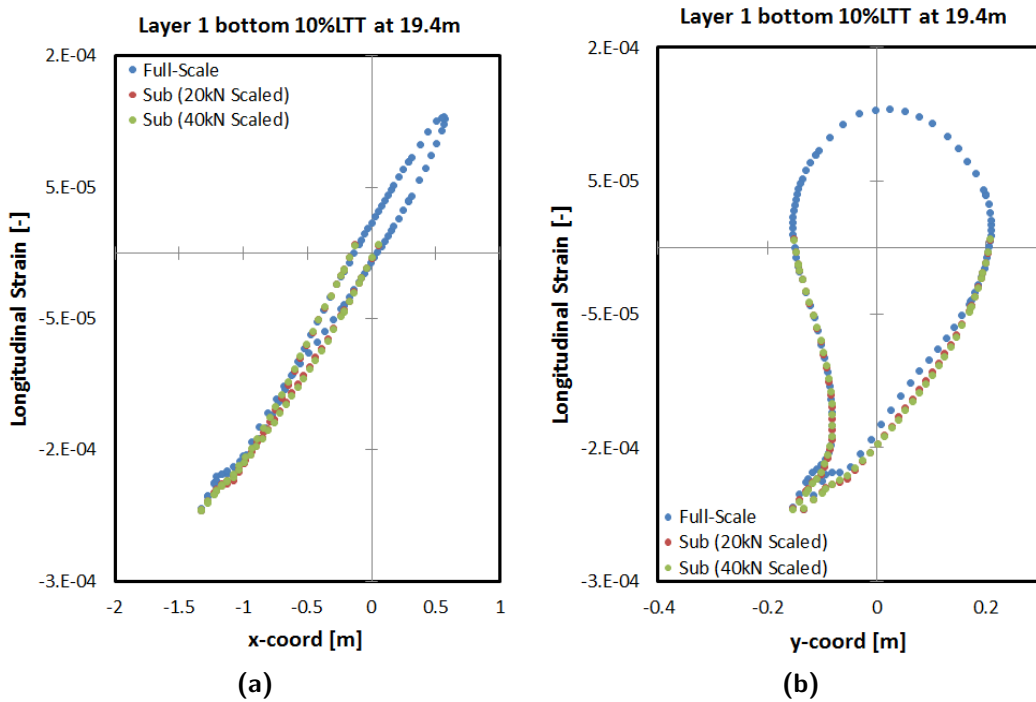


Figure 5.14: a) Longitudinal strain at 10% load along the path at  $z=19.4$  m vs.  $x$ -coordinate for full-scale blade and sub-component section, the latter scaled from both 20 kN and 40 kN. b) Same strain results vs.  $y$ -coordinate.

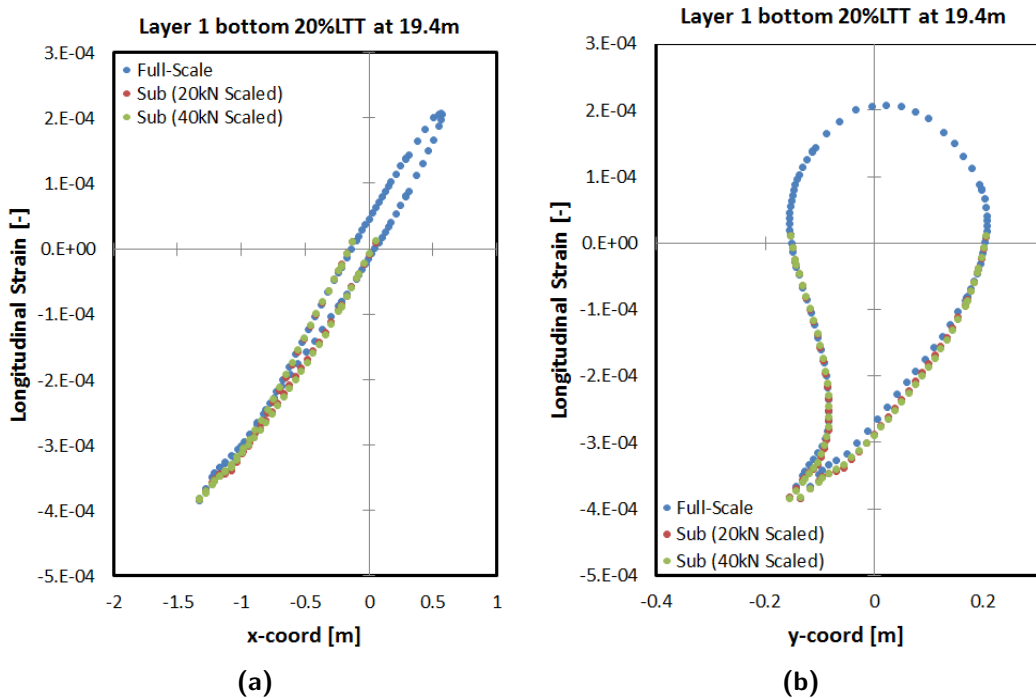
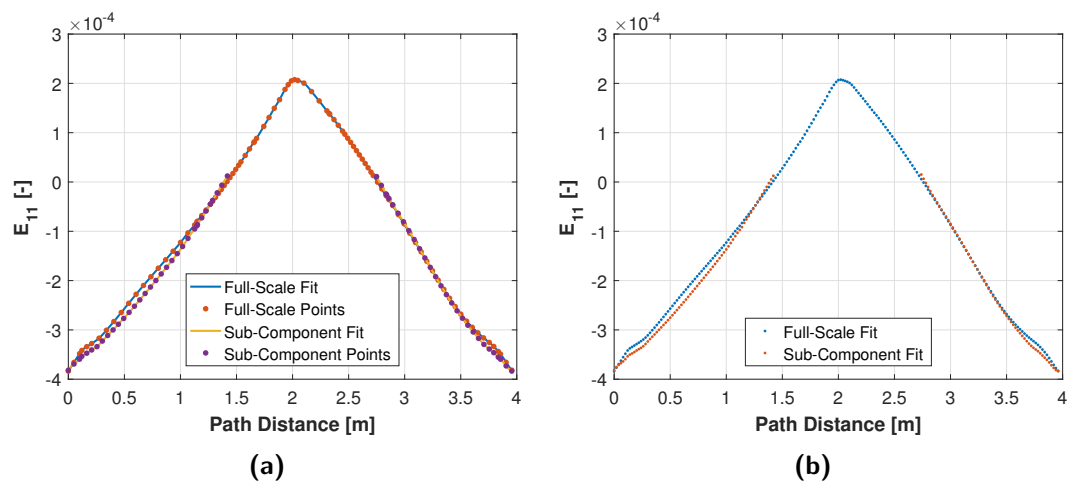
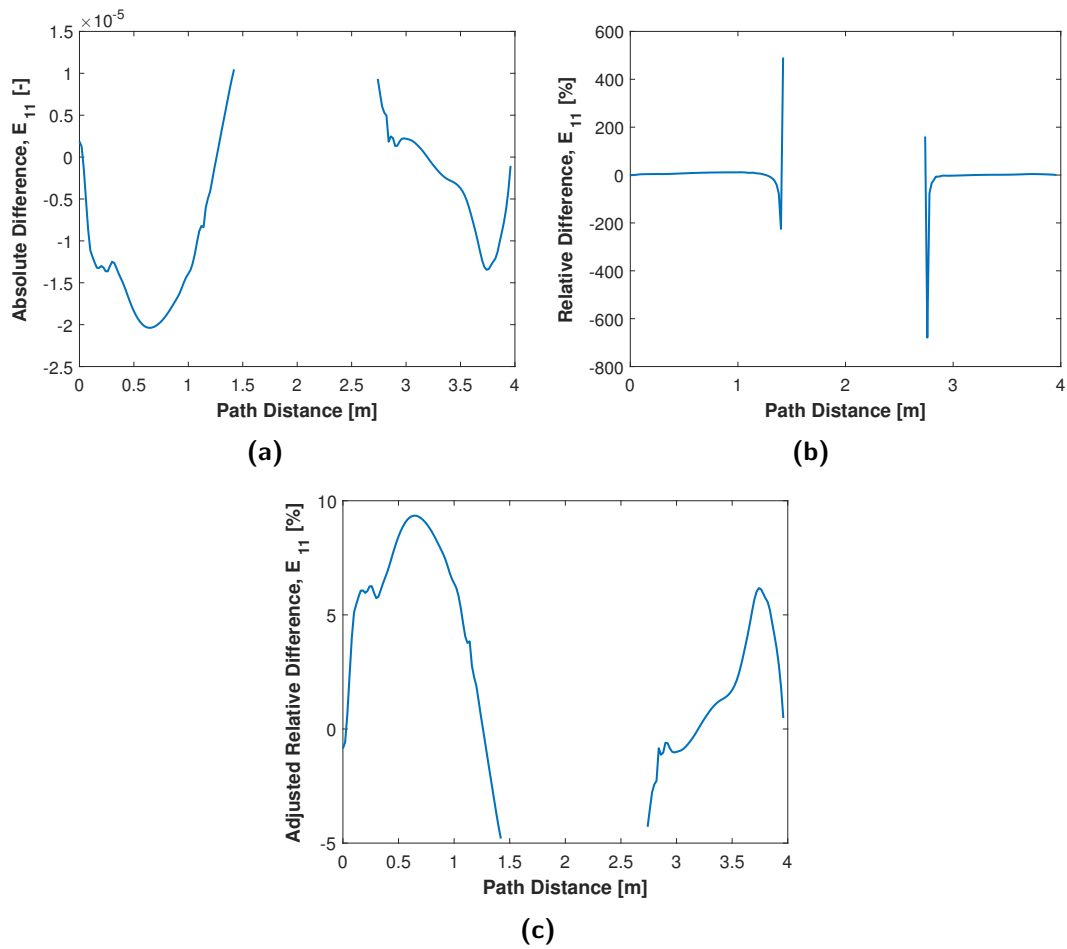


Figure 5.15: a) Longitudinal strain at 20% load along the path at  $z=19.4$  m vs.  $x$ -coordinate for full-scale blade and sub-component section, the latter scaled from both 20 kN and 40 kN. b) Same strain results vs.  $y$ -coordinate.



**Figure 5.16:** a) Spline fit through longitudinal strain data points at 20% load along the path at  $z=19.4$  m for full-scale blade and sub-component section scaled from 40 kN  
b) Points generated on the curve fit at constant interval of 2 cm.



**Figure 5.17:** The results are for the path at  $z=19.4$  m a) Absolute longitudinal strain difference between full-scale blade and sub-component. b) Relative difference between longitudinal strain of full-scale blade and sub-component. c) Adjusted relative difference between longitudinal strain of full-scale blade and sub-component.

### 20.75 Section

The strain results for the 20.75 section is shown in this section. A comparison of Figure 5.18 and Figure 5.19 shows that the match is better under 20% LTT loading. The results in Figures 5.20 and 5.21 were therefore calculated for 20% LTT. The scaled sub-component strain from 20 kN and 40 kN also appear identical and the one from 40 kN was chosen for the relative difference analysis. The adjusted relative difference graph was made based on the maximum strain at 0.4 m. The relative difference for this section is below 5% and again shows a very good match in strain.

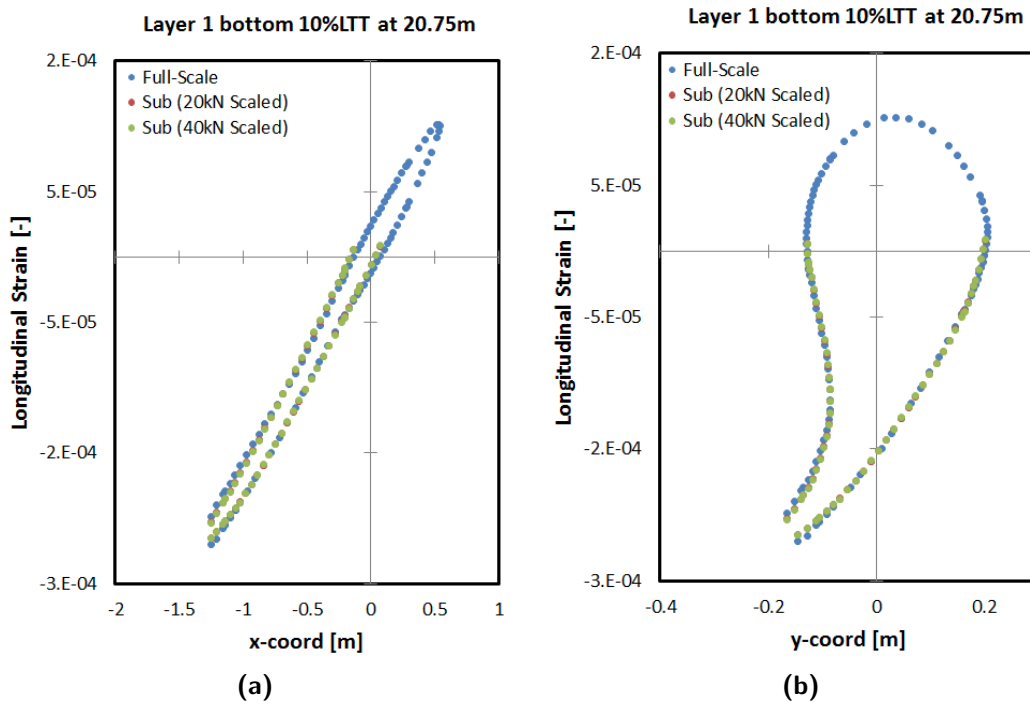


Figure 5.18: a) Longitudinal strain at 10% load along the path at  $z=20.75\text{ m}$  vs.  $x$ -coordinate for full-scale blade and sub-component section, the latter scaled from both 20 kN and 40 kN. b) Same strain results vs.  $y$ -coordinate.

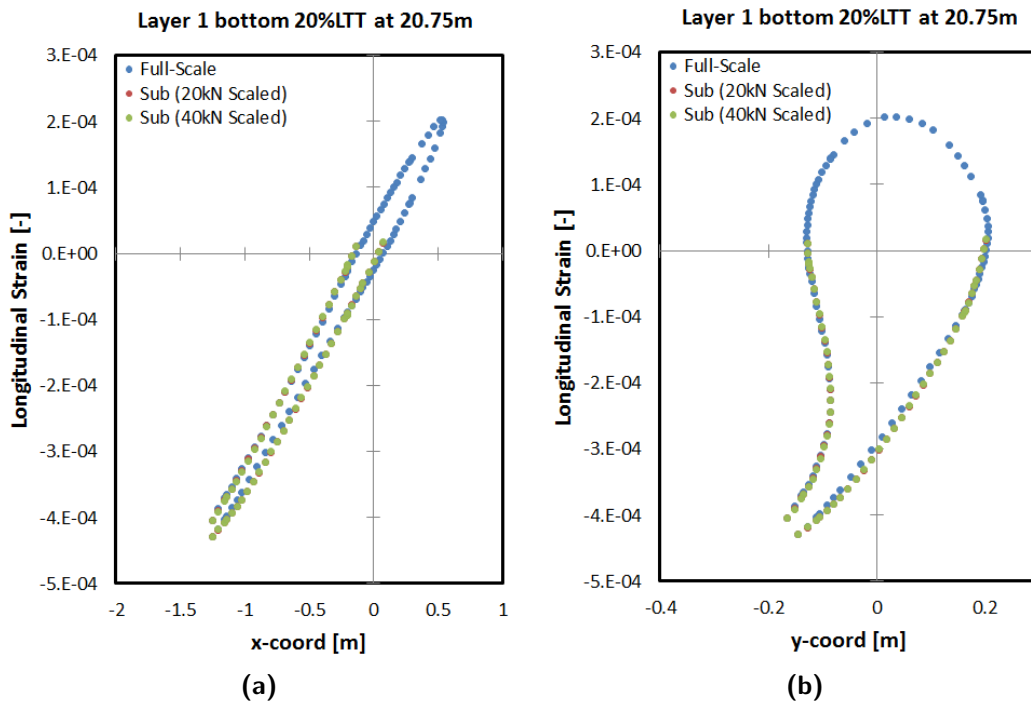
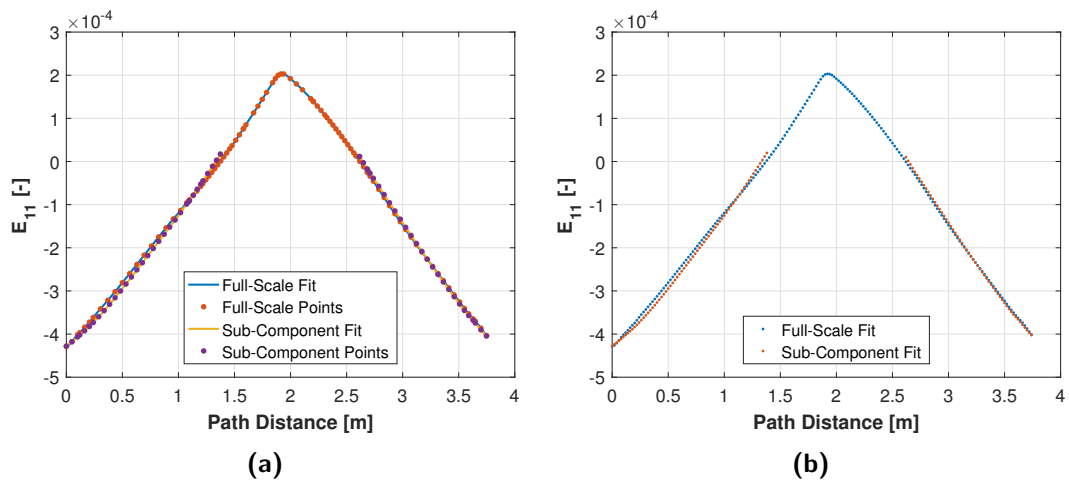
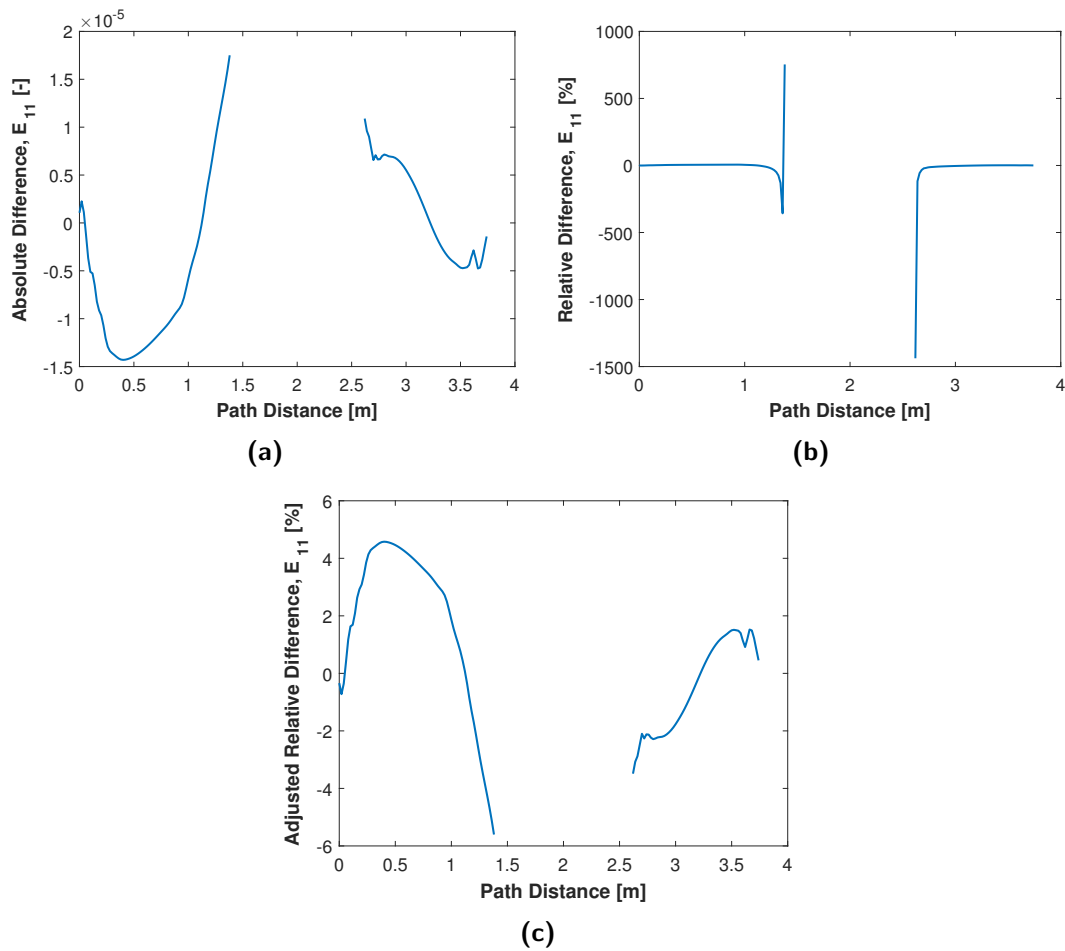


Figure 5.19: a) Longitudinal strain at 20% load along the path at  $z=20.75\text{ m}$  vs.  $x$ -coordinate for full-scale blade and sub-component section, the latter scaled from both 20 kN and 40 kN. b) Same strain results vs.  $y$ -coordinate.



**Figure 5.20:** a) Spline fit through longitudinal strain data points at 20% load along the path at  $z=20.75$  m for full-scale blade and sub-component section scaled from 40 kN b) Points generated on the curve fit at constant interval of 2 cm.



**Figure 5.21:** The results are for the path at  $z=20.75$  m a) Absolute longitudinal strain difference between full-scale blade and sub-component. b) Relative difference between longitudinal strain of full-scale blade and sub-component. c) Adjusted relative difference between longitudinal strain of full-scale blade and sub-component.

## 5.5 Discussion

The results show that the longitudinal strain distribution on the specimens is very close to the strain distribution seen by the blade under LTT loading. The sub-component test set-up is therefore able to quite closely generate a loading distribution similar to a full-scale test. The difference in strain, while small, may be caused by the simplification of the applied moment on the sub-component specimen. Before demonstrating why that is, Figure 5.22 should first be well understood.

The illustration of Figure 5.22 provides a detailed pictorial description of the difference in loading acting on a given blade section between the full-scale LTT methodology and the sub-component methodology. First, the root x and y-axis are the global axis of the blade and are oriented as shown. As mentioned, the LTT loading condition consists of shear forces acting in the -x direction. This in turn results in the bending moment denoted as

$M_{LTT}$  about the y-axis. Because wind turbine blades are slightly twisted when going from root to tip in order to more efficiently capture the energy from the wind,  $M_{LTT}$  acts at an angle with respect to the cross-section of the blade at a certain radial distance from the root. Blade cross-sections have principal axis (which are axis at which the strain would be zero along that axis if a moment was taken about that axis) that are generally oriented as shown for an airfoil geometry [43]. Interesting fact, if this was a symmetric airfoil, then the principal axis would be aligned with the chordline. This is because if an area has an axis of symmetry, then that axis and an axis perpendicular to it would create a set of principal axes [44]. The  $M_{LTT}$  moment can then be broken down into components in both principal axis. We call these  $M_{edge}$  and  $M_{flap}$ . When bending occurs on an unsymmetric cross-section at an angle from the principal axes, the neutral axis (which means that strain is zero along that axis) is offset at an angle from both the bending moment and the axis of symmetry. This is because the strain coming from  $M_{edge}$  cancels out with the strain from  $M_{flap}$  along this line. The derivation for the governing formulas are shown in Section 6.5 of [44]. This explains why the neutral axis is more slanted from the root y-axis and therefore also the principal axis when taking a cross-section farther away from the root.

The sub-component test rig is designed such that the hinge should be aligned with the neutral axis of the blade cross-section. The force acting on the plates creates a moment, called  $M_{sub}$  which is in the direction of the neutral axis and creates a triangular loading as shown in Figure 5.22. The slight problem is that in this section, we are comparing the strain results from  $M_{LTT}$  and  $M_{sub}$  but these are slightly offset from each other. They are in fact off by a slight moment called,  $M$ , which is about the root x-axis. This moment component does not affect the sub-component strain but does play part of the full-scale strain. Perhaps this small moment  $M$  is contributing to a slight difference in the sub-component strain and full-scale strain.

What is certain, however, is that the slight tensile strain at the bottom of the blade section (i.e close to the neutral axis of the full-scale cross-section) that was found on all strain comparison figures is attributed to resultant forces acting at a distance from the elastic axis of the cut blade section. This is well explained by Figure 5.23. The resulting strain distribution from the contribution of both moments gives a strain distribution that is slightly tensile at the bottom of the section, while the upper portion is under compressive loading.

Overall, there does not appear to be any clear trend in the location at which the strain difference is higher between the sections. Other observations includes the fact that scaling the sub-component strain from slightly lower or higher load levels does not affect the results since the response is very linear at this load level. This is not true for the response difference of the full-scale blade between 10% and 20% LTT load. While the distribution appears very similar at 14.5, there are important differences in the response at 19.4 and 20.75. The strain matched better at 20% LTT over 10% maybe because of less potential noise coming from a very low load and/or less initial response from when the load is applied (i.e transient effects). In any case, it also preferable in the experiment for the strain to not be measured at too low loading in order for the sensors to not see too much noise, and also not to have the results be influenced by an initial response.

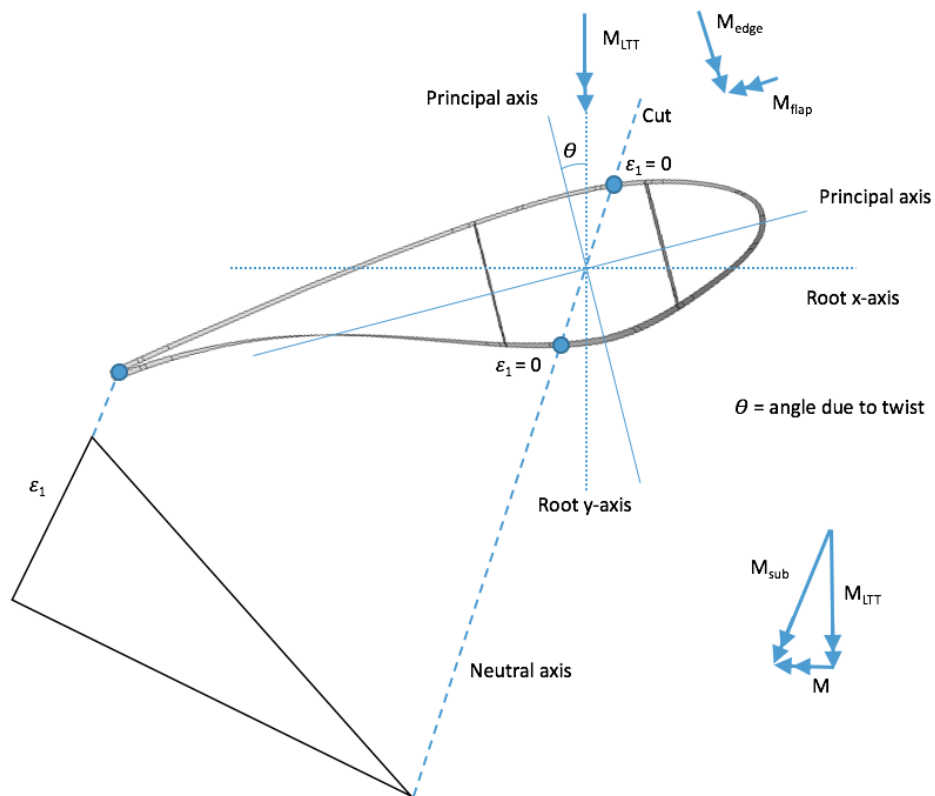


**Figure 5.22:** Schematic showing a comparison of the moment acting on the section under the full-scale LTT load case vs. the simplified moment acting on the sub-component specimen.

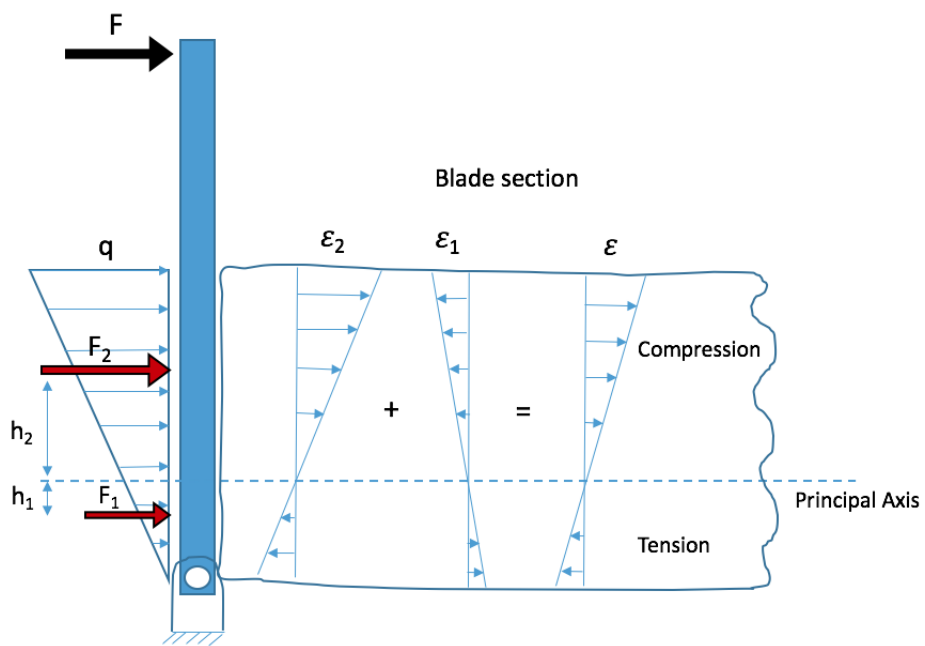


**Figure 5.23:** Schematic illustrating that the forces on the sub-component create two resultant bending moments, one above and the other below the principal axis of the blade. The contribution of each of these moments give the total strain distribution shown.

## Buckling Analysis of the Three Sections

In this chapter, buckling analyses are done on the 14.5, 19.4 and 20.75 sections by using the numerical models from Chapter 5 and applying the knowledge gained from Chapter 3 in performing buckling analyses. The results will help predict the buckling behavior of those sections but also allow determining which cases are prone to boundary effect problems. This information will set the stage for analyzing how to shift the buckling wave towards to middle of the specimen.

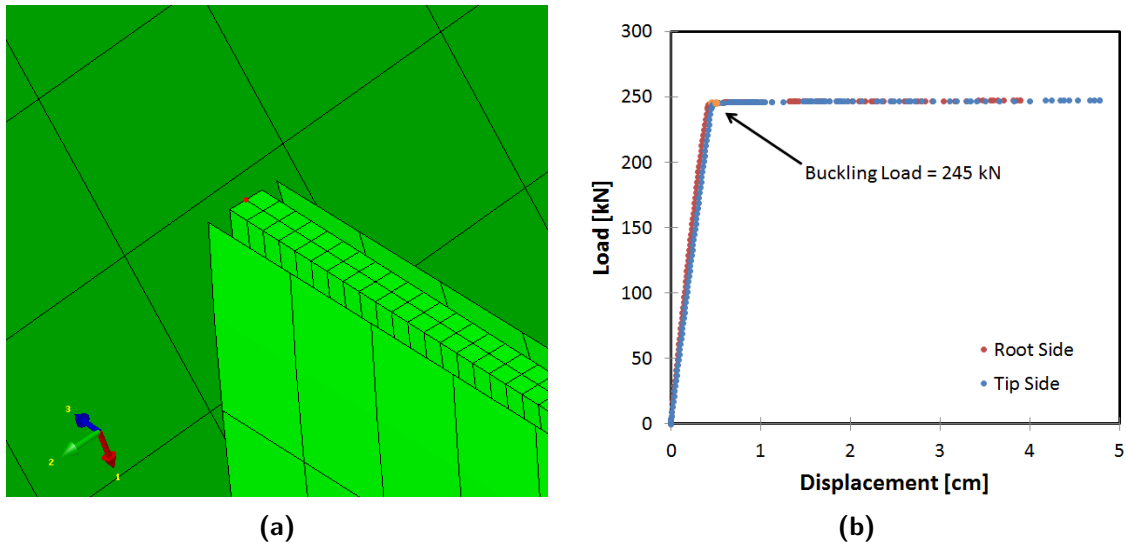
In Chapter 3, it was determined that using a characteristic length of 4 cm for the shell elements give results that have sufficiently converged for the buckling analysis of the 27.5 section. This mesh density is applied to the three blade section and the mesh details are found in Table 6.1.

**Table 6.1:** Mesh details of the 3 blade section assemblies for buckling analyses.

Section	Part	Element Type	Char. Element Size [m]	# Elements	# Nodes
14.5	Composite	S8R	0.04	7,441	22,678
		STR165	0.05	2	
	Glue Plates	C3D8I	0.01	4,800	10,836
		C3D8I	0.05	5,120	6,970
	<b>Total:</b>			14,878	32,965
19.4	Composite	S8R	0.04	6,080	18,555
		C3D8I	0.01	4,800	10,836
	Glue Plates	C3D8I	0.05	7,680	10,250
		<b>Total:</b>			16,758
20.75	Composite	S8R	0.04	5,850	17,857
		C3D8I	0.01	4,800	10,836
	Glue Plates	C3D8I	0.05	8,960	11,890
		<b>Total:</b>			17,780

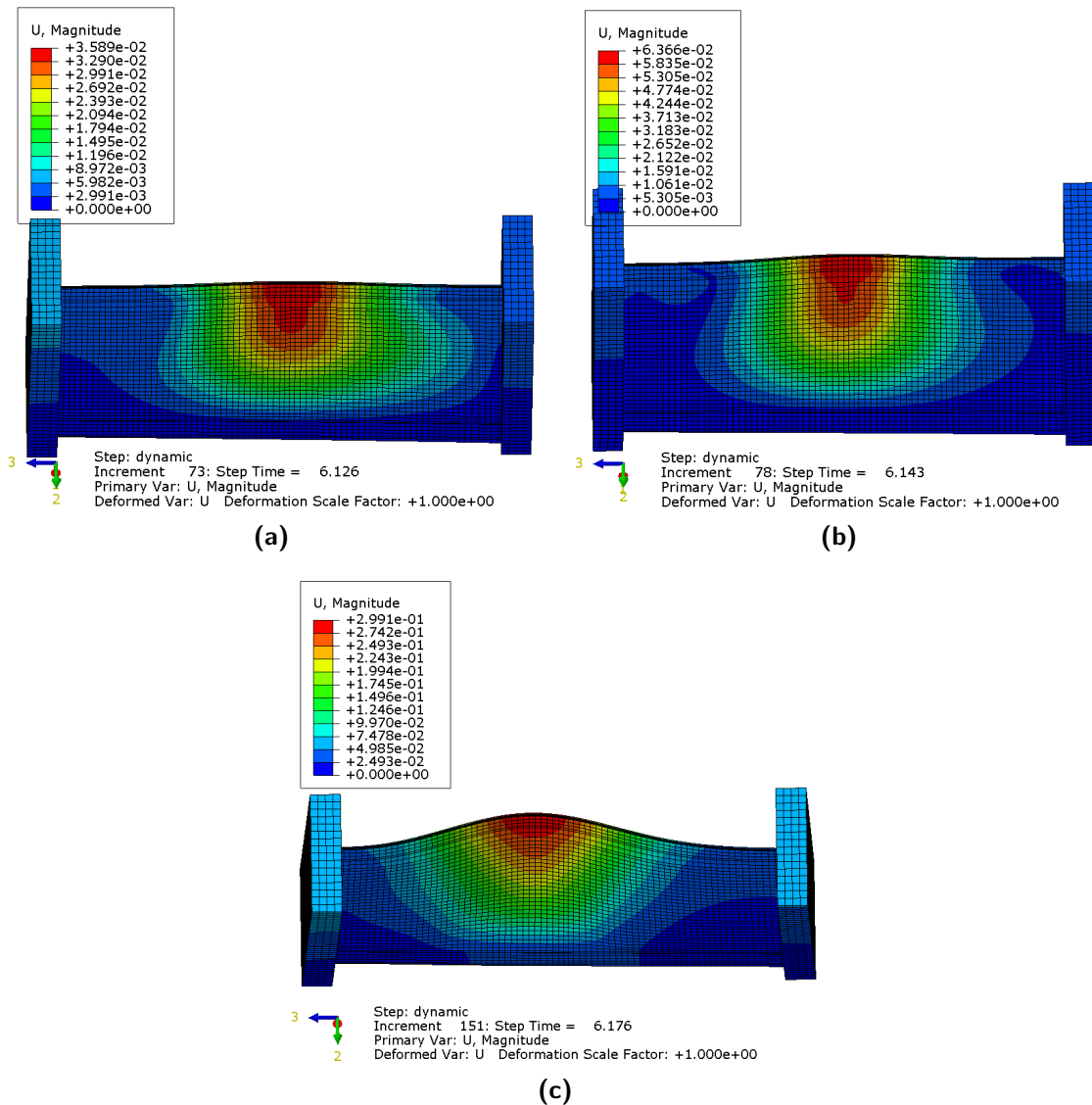
## 6.1 14.5 Section

A buckling analysis was performed on the 14.5 section using the implicit dynamic solver. The displacement history in the z-direction was extracted at two end nodes, one on the tip side and the other on the root side, in order to calculate the end-displacement. See Figure 6.1a for the location of the node on the tip side, in red. A load displacement graph was then created from the displacement of the two end nodes, as shown in Figure 6.1b. The overlap of the curves indicate that both top ends of the section deform equally. The buckling load was found to be 246 kN and was found using the method described in Section 3.5.



**Figure 6.1:** a) Location of node at which displacement is calculated for the load-displacement diagram, in this case on the tip side. b) Load-displacement diagram of the 14.5 section. The end-displacement is calculated in the z-direction.

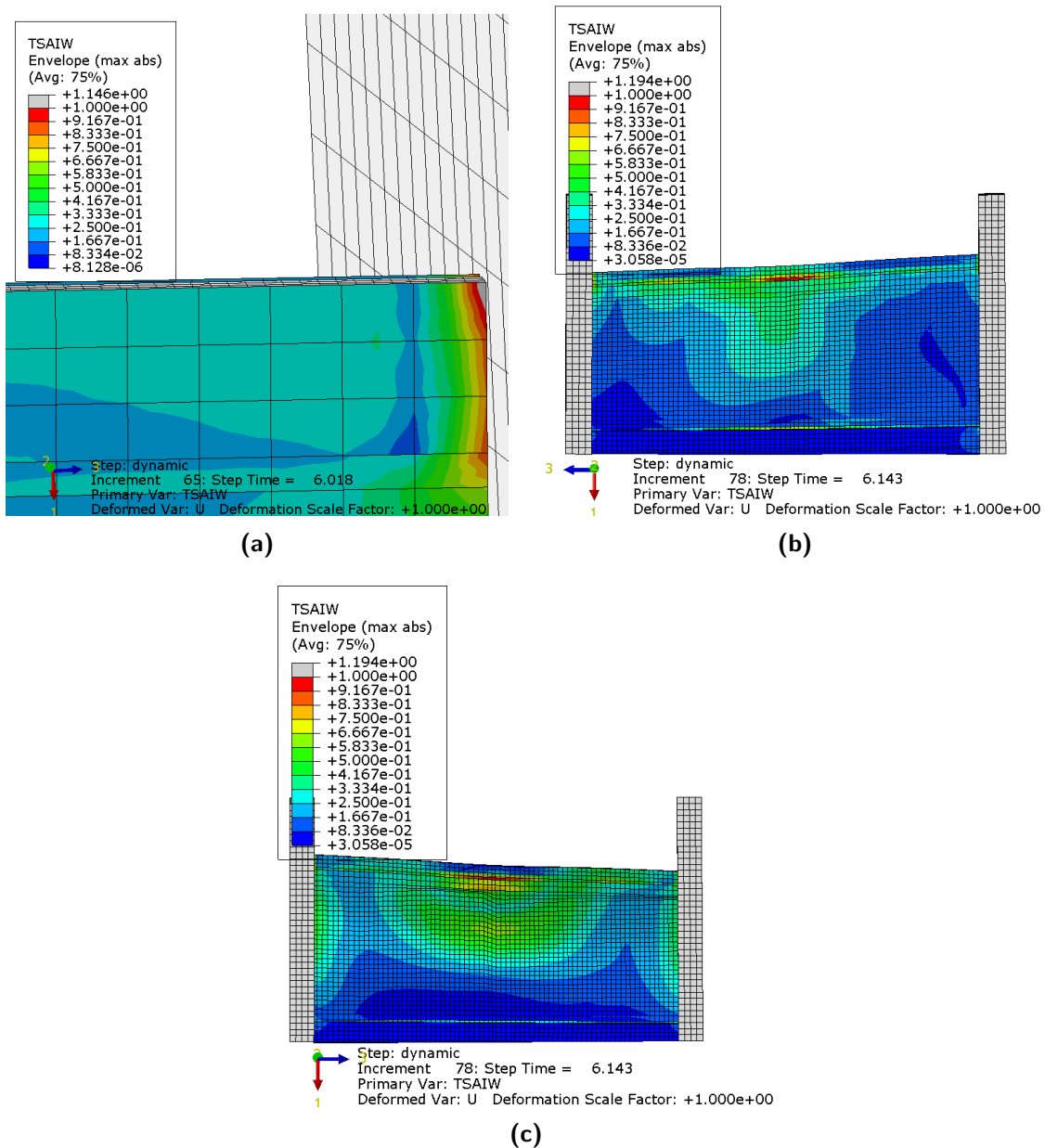
The displacement field of the 14.5 section is shown in Figure 6.2, at three different times in the load history. Figure 6.2a shows the displacement field at the buckling load of 245 kN, the displacement field at the failure load of 246 kN (which is described soon) is shown in Figure 6.2b and the displacement field at the final recorded instance (247 kN) is shown in Figure 6.2c. The results show that the buckling wave develops approximately in the middle of the specimen for this section.



**Figure 6.2:** These results are for the 14.5 section. a) Displacement field at buckling load. b) Displacement field at failure load. c) Displacement field at last recorded step.

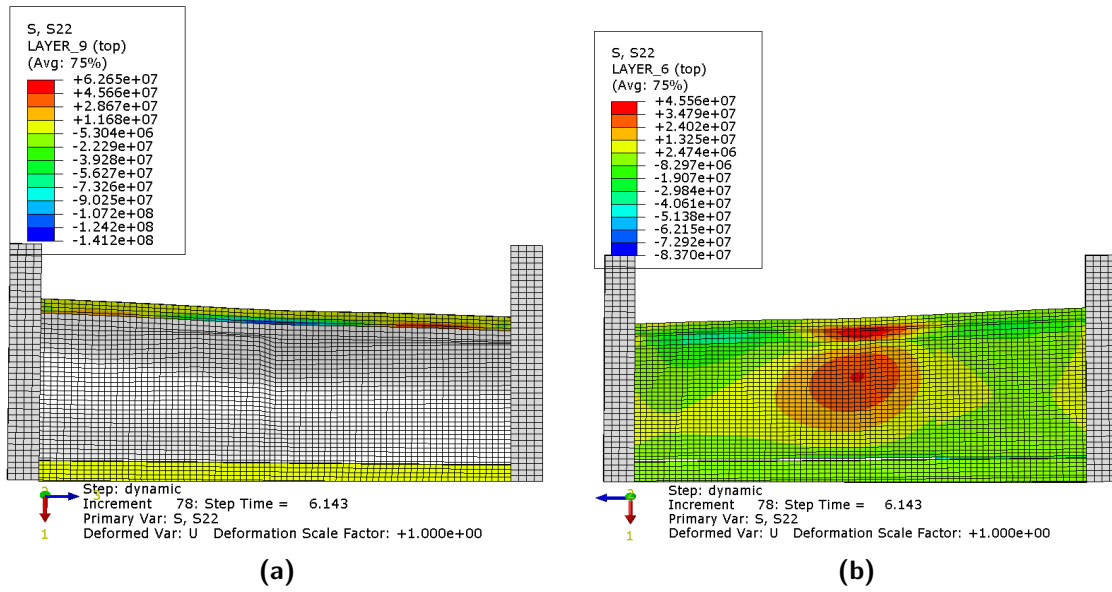
The Tsai-Wu criterion field in Figure 6.3a shows that material failure might occur first at a load of 241 kN in the top region of the boundaries in grey. This is however likely a stress concentration in the numerical model. Since the high stress concentration occurs in one element, it would be wise to refine the mesh to assess whether it is simply a numerical error from the interpolation within the element.

At a load of 247 kN, the material failure is shown to occur on both the suction side (Figure 6.3b) and pressure side (Figure 6.3c) right under the adhesive bondline at the buckling wave location.



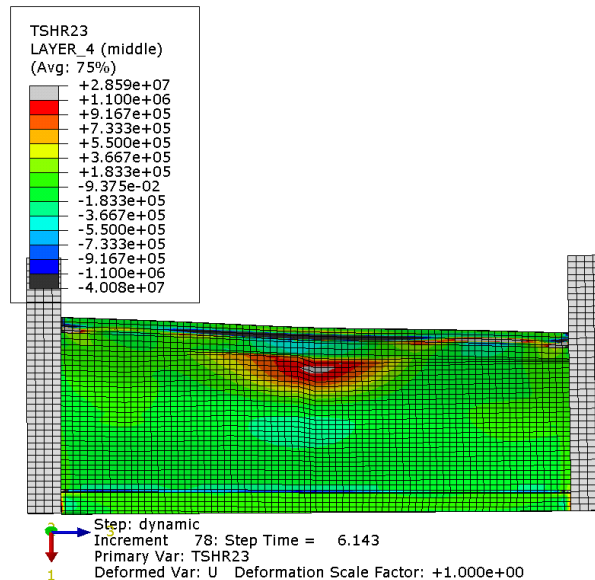
**Figure 6.3:** These results are for the 14.5 section. a) Example of stress concentration at boundaries. b) Tsai-Wu failure criterion field at failure on suction side. c) Tsai-Wu failure criterion field at failure on pressure side.

A closer look at the predicted failure on the pressure side suggests that transverse compressive stress on ply-9 (the innermost ply) is the predominant stress on the pressure side since the maximum transverse compressive stress at this load level is  $-1.412 \times 10^8$  Pa which exceeds the transverse compressive strength of  $-1.271 \times 10^8$  Pa for the YE900 composite material that makes this lamina (Figure 6.4a). On the suction side, the main driver for failure is transverse tensile stress on ply-6. As shown in Figure 6.4b, the maximum transverse tensile stress is  $4.556 \times 10^7$  Pa and this exceeds the transverse tensile strength of the material EGL1600 which makes up this ply with a strength of  $4.214 \times 10^7$  Pa.



**Figure 6.4:** a) Transverse stress on pressure side of 19.4 section, showing compressive failure.  
 b) Transverse stress on suction side of 19.4 section, showing tensile failure.

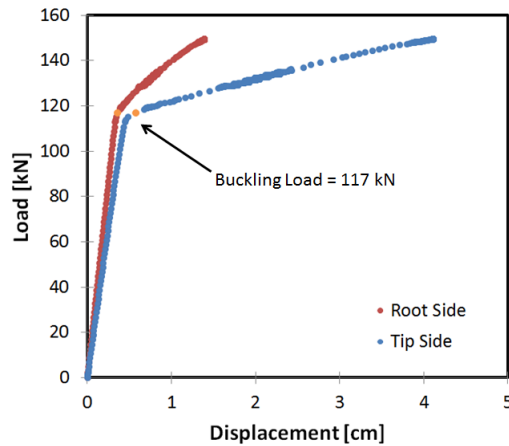
An evaluation of the out-of plane shear stress was also performed in order to assess the possibility of core shear failure on the specimen. This failure type turned out to be the failure mode observed during full-scale LTT testing of the three SSP blades in the DTU study. Figure 6.5 demonstrates that core shear failure does occur on the pressure side of the blade, shown in red, from the out-of plane shear stress exceeding the core shear strength of 1.1e6 Pa also at 247 kN.



**Figure 6.5:** Out of plane shear stress field of the 14.5 section at which core shear failure initiates, in red.

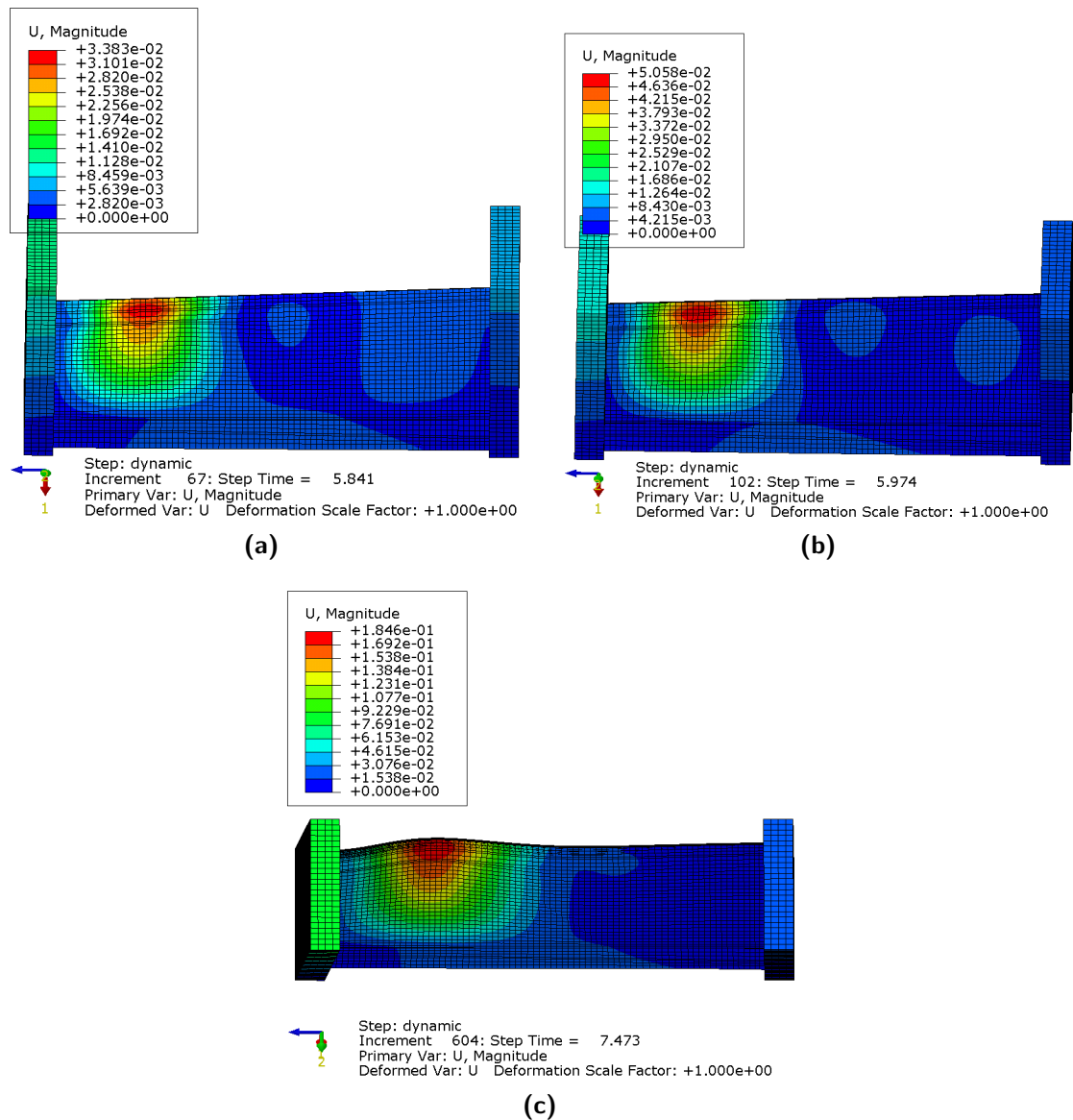
## 6.2 19.4 Section

Figure 6.6 demonstrates the load-displacement diagram for the 19.4 section. Both ends of the section have a different load history curve, and it illustrates that the tip side has a higher displacement than the root side. The buckling load was found to be equal to 117 kN, using the same method as for the 14.5 section.



**Figure 6.6:** Load-displacement diagram of the 19.4 section.

The displacement fields for the 19.4 section at buckling load (117 kN), failure load (119.5 kN) and final recorded step (149.5 kN) are shown in Figure 6.7. The results show that the buckling wave forms towards the pressure side, closer to the tip end of the section.



**Figure 6.7:** These results are for the 19.4 section. a) Displacement field at buckling load. b) Displacement field at failure load. c) Displacement field at last recorded step.

Looking at the Tsai-Wu failure criterion shows that as for the 19.4 section, there is a stress concentration near at the top boundary (See Figure 6.8a). The figure also shows that material failure will occur on the pressure side of the buckling wave, below the bondline, at 119.5 kN. After careful investigation, this failure is caused by high transverse compression on the innermost ply of this region. Figure 6.8b demonstrates that the maximum compressive stress in the transverse direction of this ply is  $-1.374 \times 10^8$  Pa, which is higher than the compressive strength in the transverse direction of  $-1.271 \times 10^8$  Pa for the YE900 composite lamina of this ply.

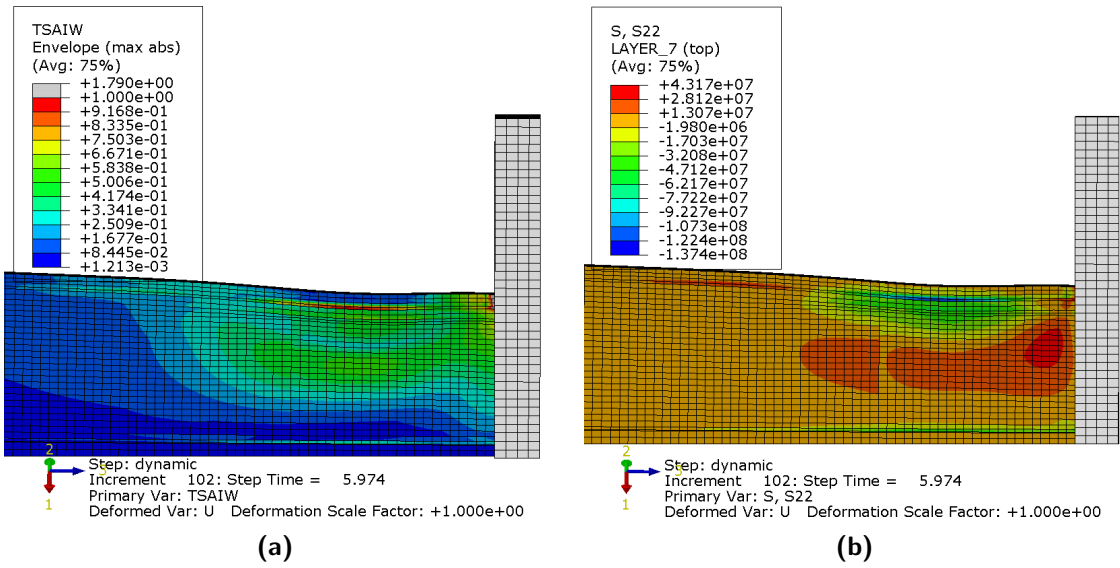


Figure 6.8: a) Tsai-Wu failure criterion field at failure on the pressure side of the 19.4 section. b) Transverse stress on the pressure side of the 19.4 section, showing compressive failure.

Core shear failure is expected on the pressure side of the buckling wave, shown in grey on Figure 6.9, at a load of 120 kN.

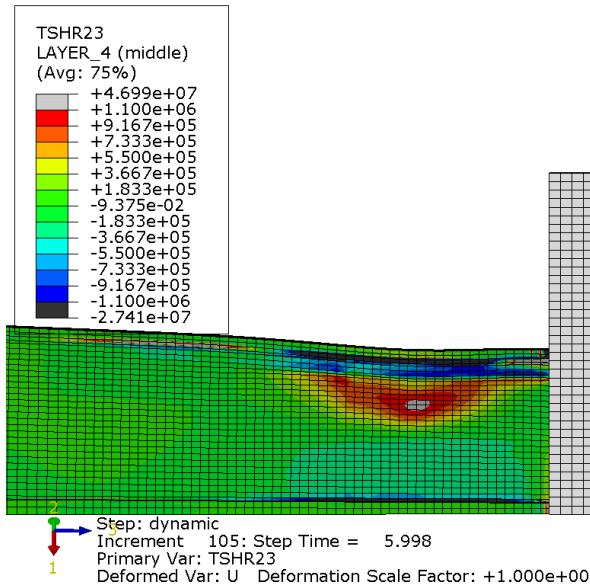
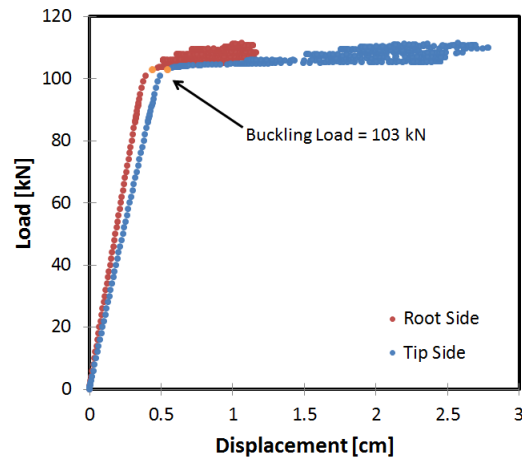


Figure 6.9: Out of plane shear stress field of the 19.4 section at which core shear failure initiates, in grey.

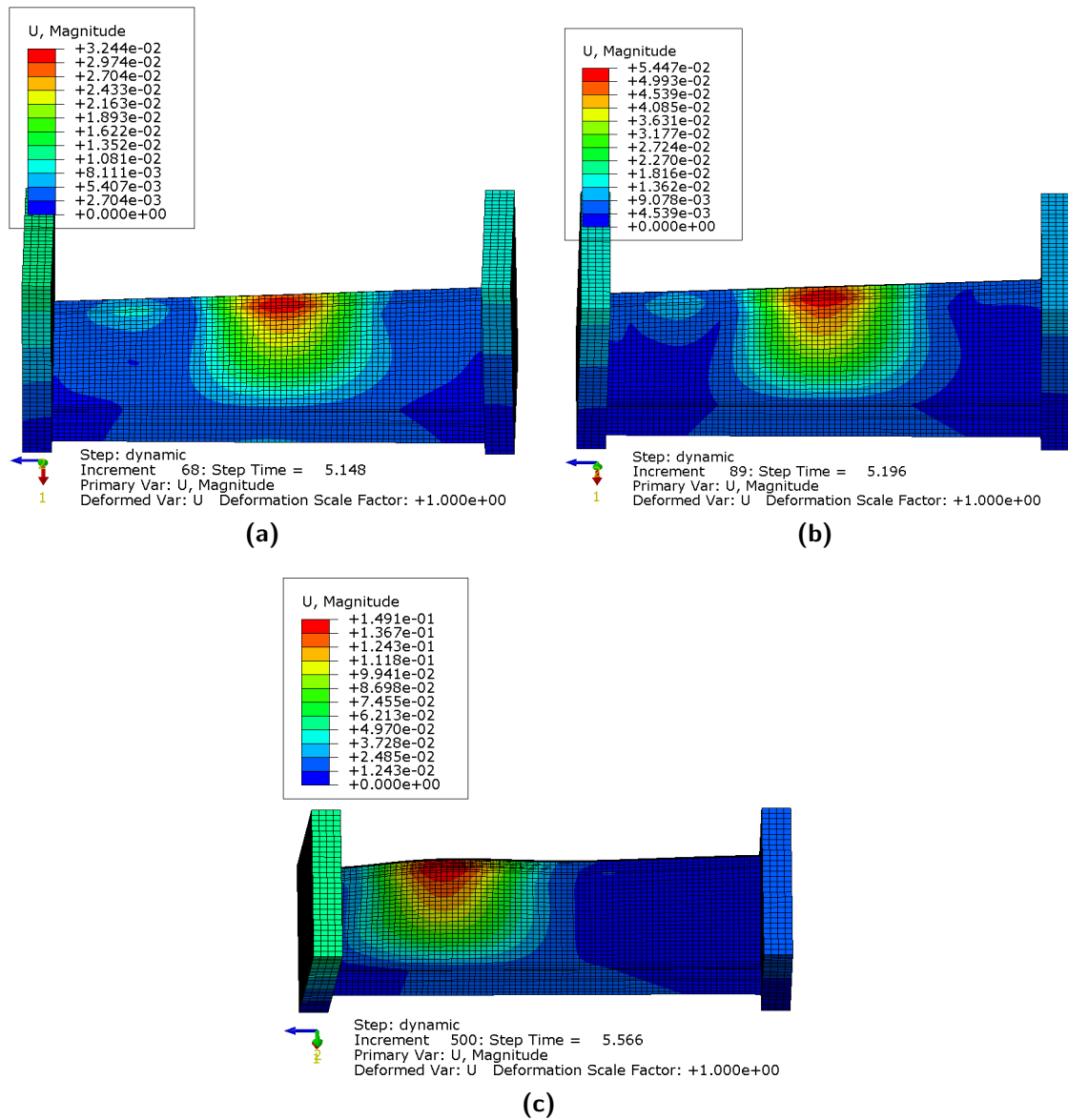
### 6.3 20.75 Section

The load vs. displacement of both ends of the 20.75 section is presented in Figure 6.10. Buckling is found to occur when the plates are loaded at 103 kN. The solver has more difficulty finding equilibrium on this section, hence why there is a slight back and forth movement of the plates.



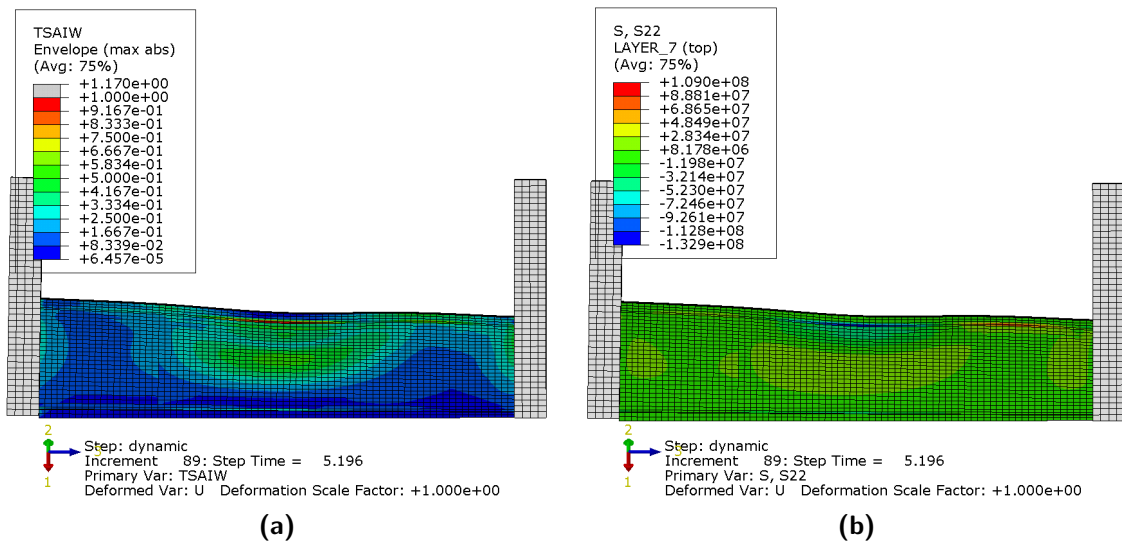
**Figure 6.10:** Load-displacement diagram of the 20.75 section.

Figure 6.11, shows the displacement field of the 20.75 section at buckling load (103 kN), at Tsai-Wu criterion material failure load (104 kN) and last recorded step (111 kN). The buckling wave therefore appears in the middle of the specimen but then shifts towards the tip side of the specimen as the load is increased.



**Figure 6.11:** These results are for the 20.75 section. a) Displacement field at buckling load. b) Displacement field at failure load. c) Displacement field at last recorded step.

The Tsai-Wu Failure criterion field shows failure on the top edge of the tip side and slightly below the adhesive section on the pressure side of the buckling wave, as seen in Figure 6.12a. Figure 6.12b, shows that like the 19.4 section, transverse compressive stress is the driver for failure and this occurs in the innermost ply. Again, the ply that fails is composed of the material YE900.



**Figure 6.12:** a) Tsai-Wu failure criterion field at failure on the pressure side of 20.75 section. b) Transverse stress on the pressure side of 20.75 section, showing compressive failure.

Core shear failure is expected on the pressure side of the buckling wave, shown in grey on Figure 6.13, at a load of 104 kN.

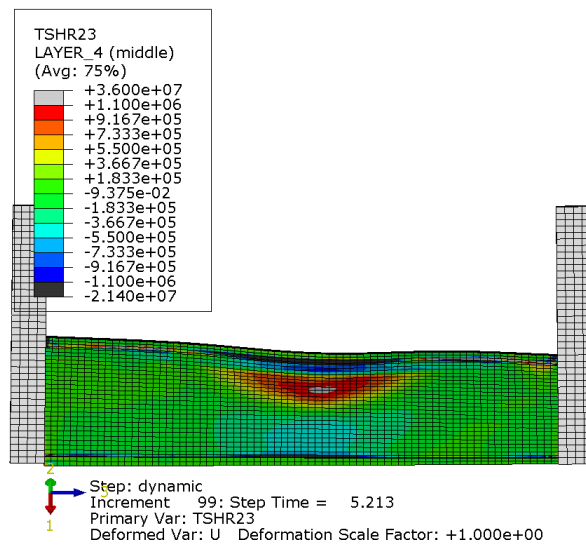


**Figure 6.13:** Load-displacement diagram of the 20.75 section.

## 6.4 Discussion

A few general observations can be made based on the buckling results of the three specimens.

1. The buckling wave points towards the pressure side of the blade for all three sections.

2. As Figure 6.14a demonstrates, there appears to be a general trend that the location of the wave center lies closer to the tip boundary edge as the section taken is closer to the tip. However, the buckling wave location of the 20.75 section when a mesh of 4 cm is used does not follow this trend as it lies approximately in the center of the blade section. It is quite surprising that this data point does not follow the trend. Finer meshes of 3 cm and 2 cm were used to verify this observation and it showed the same behavior. When a 5 cm mesh was used, it seemed like the buckle would appear in the center up until it finally emerged on the tip side (see Figure 6.15). This preliminary small deformation in one location and the buckling wave appearing in another was only seen on the 20.75 section, suggesting that the buckling wave is not so predictable for this section and the equilibrium struggles between two solutions. The reason why it turns out to appear in the center of the section is not so clear but one idea is that it might be influenced by the composite section distribution in this blade sub-component. In any case, it does converge towards the other solution as the load is increased. This interesting response is revisited later in this discussion section.
3. Figure 6.14b shows that the buckling load goes down as the section taken lies closer to the tip. This is because the section "height" with respect to the plate is smaller and so less force is needed to buckle the blade section due to less reaction moment. These results are from using a 4 cm mesh for the shell elements, and using a 5 cm do not change the results. It is therefore interesting to note that the buckling load for the 20.75 section is the same between using a 4 cm mesh compared to a 5 cm while the buckling location is completely different.
4. Ply failure according to the Tsai-Wu criterion and core shear failure are expected to occur simultaneously right when the section buckles. This failure is expected on the pressure side of the blade behind the buckling wave, right under the adhesive bond line, for all three section. Ply failure occurs from compression in the transverse direction to the fibers, in the innermost ply of the region. The results show that failure might also occur at the top corner of the specimen from stress concentrations but this might only be a numerical result from a mesh that is too coarse. Mesh refinement is recommended to assess its effect on the results.
5. The blade section retains load bearing capacity after buckling, as seen on load-displacement graphs, while the stiffness of the section goes down considerably. This is as expected because the load normally taken on by the failed region is then covered by other regions of the sections that can still carry some load.

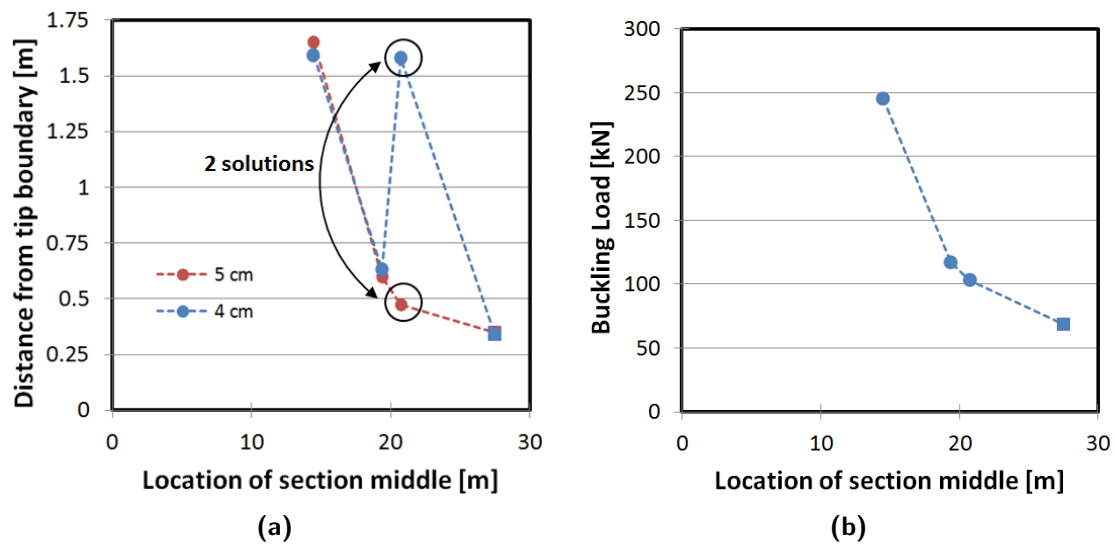


**Figure 6.14:** a) Buckling wave location per section location. b) Buckling load per section location. Note that the 27.5 section results (shown by a square) have also been included even though it was cut differently from the other sections.

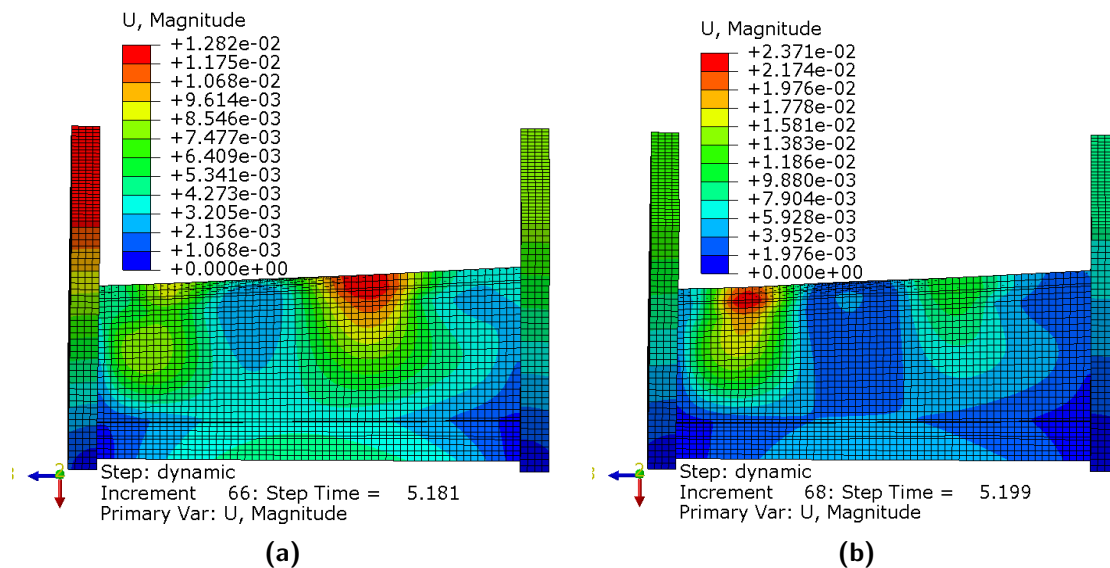


**Figure 6.15:** Displacement field of the 20.75 blade section using a mesh with characteristic lengths of 5 cm. a) Results at time step 5.181 b) Results at time step 5.199. There is a sudden shift in maximum displacement location.

This analysis showed that there appears to be a trend where the buckling wave is off-centered, and prone to boundary effects, for sections of the blade lying closer to the tip of the blade, starting somewhere at a  $z$ -location of the middle of the section somewhere between  $z=14.5$  and  $z=19.4$ . However, the results from the 20.75 section are not so easy to interpret because the solver appears to struggle in finding equilibrium between two solutions. With the converged mesh, it initially picked the solution not following the trend but later converged to the solution supporting the observed trend (Figure 6.11).

What is clear, however, is that it is best to take the 19.4 section for upcoming analyses on shifting the buckling wave towards the center. The results show that the 14.5 section is known to already buckle in the center of the section, away from the ends, while the results of the 20.75 section appear unpredictable due to the struggle between two solutions and so it would not be a good choice for further analysis. The 19.4 section is therefore selected for the analysis of Chapter 8.

It is not clear at this point what influences the buckle location. Knowing this information might help in clarifying which solution is most likely to succeed in shifting the buckling wave location and so an attempt at understanding the main factors that influences the buckling location is investigated in great depth in the following chapter.

# Factors Affecting Buckling Wave Location

Before trying to move the buckling wave towards the middle, it would be wise to first try to understand what factors influence where the buckling wave will appear on a given section. This would in turn provide great insights in determining which strategies should be employed in shifting the wave. The buckling wave location could be attributed to the geometry and/or the composite design of the section since these govern the blade stiffness. The geometry and composite details are now investigated individually in order to pinpoint any specific factor that greatly impacts the buckling wave location.

## 7.1 Inspection of the Blade Section Geometries

The results in the last chapter showed that the buckling wave is generated in some instances in the center of the blade section (the 14.5 and one solution of the 20.75 section) or close to the blade section boundary (the 19.4 section and one of the solutions of the 20.75 section). If it is believed that the trend from Figure 6.14a, is correct, then one idea for why this trend occurs is the chord distribution. Perhaps, the chord distribution along the blade section varies more for sections closer to the tip of the blade and so the pronounced lower cross-sectional area on one side of the blade section means that it is less stiff in this region, hence why it would be prone to buckle. On a similar note, perhaps it is due to the difference in the distance between the suction side panel and the pressure side panels of the blade cross-section between the two ends. Blades are designed more or less as I beams and so a thicker profile means a larger moment of inertia and consequently a greater bending stiffness (as covered in undergraduate mechanics of material courses). The stiffer it is in bending, the less likely it would be triggered to buckle there. Thought the other way around, buckling would most likely occur in a region with lower distance between the plates, which we will also refer to as “thickness”. The thickness at a given z-location is a function of both the chord length and of the profile (i.e shape) of the airfoil

at that location. In order to verify these ideas, the blade cross-sections were plotted at each ends of the three blade sections (Figure 7.1). For example, Figure 7.1a shows the cross-section at both ends of the 14.5 blade section, namely at  $z=13$  m and  $z=16$  m.

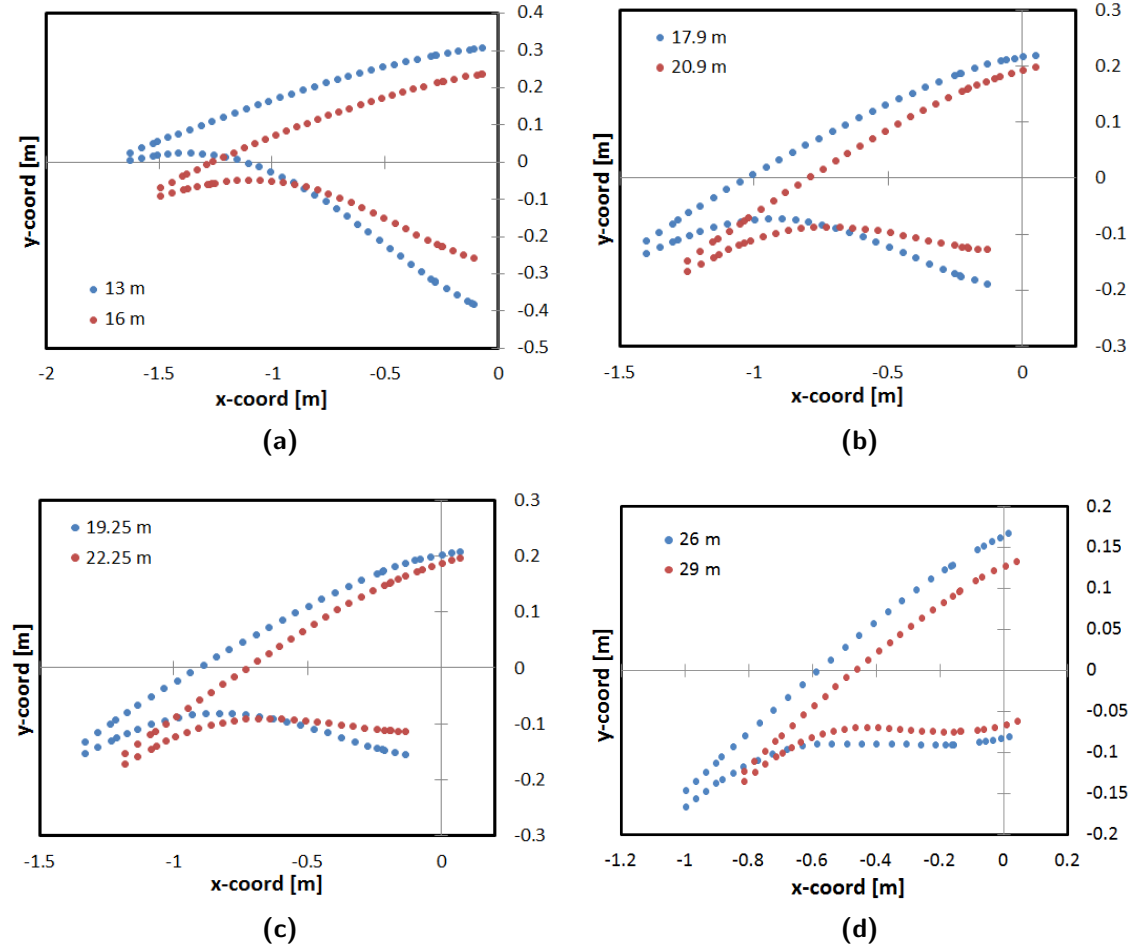


**Figure 7.1:** a) Cross-section coordinates at the ends of the 14.5 section. b) Cross-section coordinates at the ends of the 19.4 section. c) Cross-section coordinates at the ends of the 20.75 section. d) Cross-section coordinates at the ends of the 27.5 section.

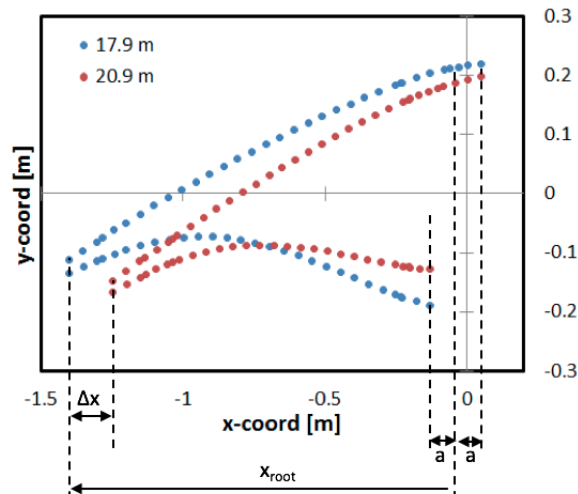
At first glance, Figure 7.1 demonstrates that the difference in either chord length, cross-sectional area or even twist between the ends of each sections appears quite consistent across the three sections. Figure 7.1a is also quite revealing because it shows that the buckling wave occurred in the middle of the section even though the cross-sectional area between the different ends of the 14.5 sections are very different. Here we assume that the transition in cross-section from one end to the other end is quite linear. Blades are typically created by lofting surfaces between different cross-sections spaced at a few meters interval and so the transition is very linear. This particular blade was modeled this way as well.

Figures might sometime be misleading, especially from scaling, so a more quantitative approach is employed next. One factor to be specifically verified is the chord length

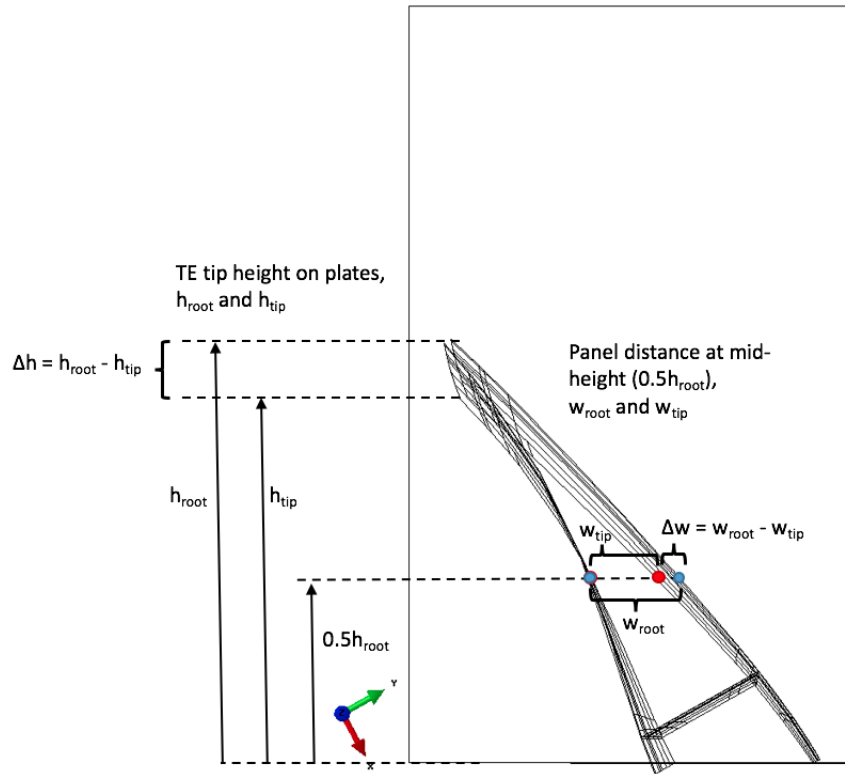
difference. However, since only the trailing edge region of the cross-section is used in the buckling test, a rough alternative is to compare the x-direction distance of the trailing edge tip between the two end cross-sections ( $\Delta x$  in Figure 7.2), or look at the difference in height (on the plates) where the trailing edge tip is located between the two ends of the blade section ( $\Delta h$  in Figure 7.3). For the latter measurement, the point lying at the center of the adhesive trailing edge tip is used (i.e same node as in Figure 6.1a). The difference in distance between the pressure and suction side panels at both cross-section ends was also computed for each section. For this rough calculation, this difference was decided to be consistently computed at the mid-height of the root side ( $0.5h_{root}$ ) as shown in Figure 7.3.

The results are shown in Table 7.1. The relative difference of the measured dimensions between the section ends are shown in Figure 7.4 against the section location. The results show that as the section lies closer to the tip, there is a greater drop in what is analogous to the chord length for these cut sections. Note also that the difference in results between the x-coordinate and heights on plates methodologies for the 19.4 and 20.75 sections are due to how the blade sections are slanted with respect to the plates. The reduction in what is analogous to the thickness of the airfoil is much more drastic since it is both a function of chord length and airfoil profile (which gets thinner towards the tip). While the 14.5, 19.4 and 20.75 sections have similar thickness drop at around 30-35%, the 27.5 section has a much steeper drop in thickness from one end to the other. It sees a decrease of around 50% in thickness. As explained earlier, this could have significant influence on the bending stiffness distribution of the blade section.

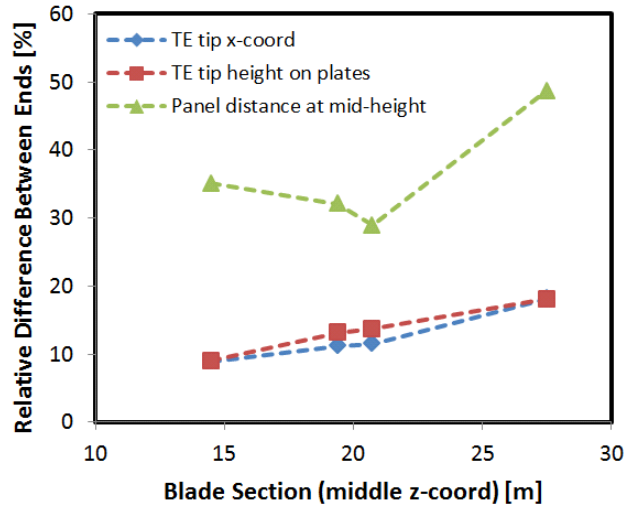
While these results provide great information, they do not appear to give any clues as to why for example the 14.5 section buckles in the middle while the 19.4 does not. The results of the geometry found for the first 3 sections are not so different and so it is hard to imagine that it would alone have such large effect on the buckling wave location. The composite details from these sections should therefore also be checked and this is done next.



**Figure 7.2:** Dimensions used in determining the absolute and relative differences in x-coordinates. The 19.4 section is used for this example.



**Figure 7.3:** Dimensions used in determining the absolute and relative difference in height on the plates and distance between the panels. The 19.4 section is shown for this example.



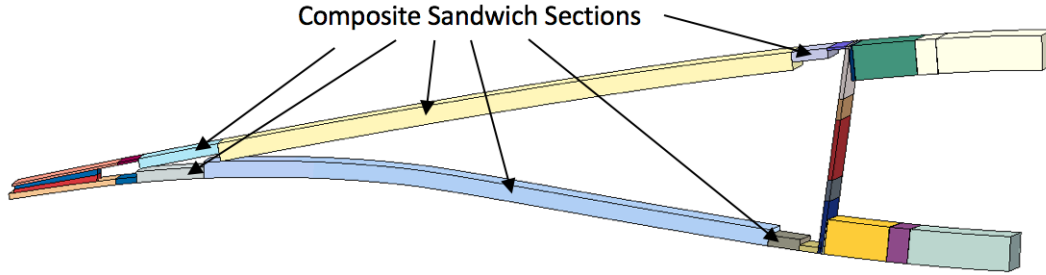
**Figure 7.4:** The percent decrease in trailing edge tip x-coord, trailing tip height on plate and distance between the pressure and suction side panels at half the height on the plate of the largest cross-section of the section, between the two cross-section ends of the plate. The results for all 4 blade sections are shown.

Table 7.1: Cross-section measurement results

	14.5 section		19.4 section		20.75 section		27.5 section	
Cross-section (z-coord)	13 m	16 m	17.9 m	20.9 m	19.25 m	22.25 m	26 m	29 m
TE tip x-coord [m]	-1.629	-1.493	-1.401	-1.249	-1.332	-1.183	-0.994	-0.810
Absolute Difference, $\Delta x$ [cm]	13.5		15.2		14.9		18.4	
Relative Difference, $\Delta x/x_{root}$ [%]	8.9		11.2		11.5		18.2	
TE tip height on plates, $h_{root}$ and $h_{tip}$ [cm]	153.0	139.3	111.4	96.8	98.5	85.0	107.5	88.0
Absolute Difference, $\Delta h$ [cm]	13.8		14.6		13.5		19.5	
Relative Difference, $\Delta h/h_{root}$ [%]	9.0		13.1		13.7		18.1	
Panel distance at mid-height ( $0.5h_{root}$ ), $w_{root}$ and $w_{tip}$ [cm]	26.4	17.1	31.5	21.4	20.4	14.5	11.3	5.8
Absolute Difference, $\Delta w$ [cm]	9.3		10.1		5.9		5.5	
Relative Difference, $\Delta w/w_{root}$ [%]	35.1		32.1		28.9		48.7	

## 7.2 Inspection of the Composite Design

The blade is made out of different composite sections, each having specific number of plies, types of materials and thicknesses. The trailing edge section is modeled as shown in Figure 7.5.



**Figure 7.5:** Cross-section of the numerical model showing the six composite sandwich sections in the trailing edge region.

The two closest sections to the tip, on both pressure and suction panels, are composed of a laminate construction and the next three sections are made out of a sandwich construction, as indicated in Figure 7.5. A composite sandwich is the build-up from inserting a soft core material in between two laminates (which are called faces when talking about sandwich construction) in order to increase the moment of inertia of the structure, and hence its bending stiffness (also called flexural rigidity). This is because the flexural rigidity,  $D$ , is the product of the elastic modulus,  $E$ , and the moment of inertia,  $I$ . According to [45], if one assumes a symmetrical lay-up of the faces (i.e both faces have the same thickness,  $t_f$ , and are made of the same materials and so both faces have the same elastic modulus,  $E_f$ ), then the expression for the flexural rigidity of a sandwich with thin faces ( $t_f \ll t_c$ ) and weak core ( $E_c \ll E_t$ ) is approximately:

$$D = \frac{E_f t_f d^2}{2} \quad (7.1)$$

where  $d$  is the sum of the core thickness,  $t_c$ , and the face thickness,  $t_f$ . Most ordinary engineering materials used in sandwich construction have a core/face thickness ratio lying between 10 to 50 and a face/core modulus ratio between 50 to 1000, hence why the thin face and weak core assumption is appropriate [45]. Expression 7.1 reveals that the flexural rigidity is most dependent on the core thickness since it scales with a factor of two with  $d$  and the core thickness makes up most of that value.

A high flexural rigidity means an increase in resistance of out of plane displacement, therefore increasing the resistance to buckling. It is thus a good idea to examine the sandwich construction of the 4 blade sections, especially core thickness as was found from Equation 7.1. Figure 7.6 to Figure 7.9 depicts the composite sections of the 4 blade pieces. The core thickness of the sandwich sections are indicated with colored labels. When going towards the tip direction, the addition or removal of plies in the face is also indicated. Note that by “one ply”, it means one ply in one face only, not in both faces.

Figure 7.6 shows that the 14.5 section has a constant core thickness along the  $z$ -direction in both pressure and suction side panels. This means that the flexural rigidity of the sandwich sections are quite constant throughout and so it supports the finding in the previous chapter of the buckling wave occurring in the center of the section. This is reasonable because the buckling wave would naturally stay away from the blade ends because the fixed boundary conditions prevents out-of-plane deformation at those locations.

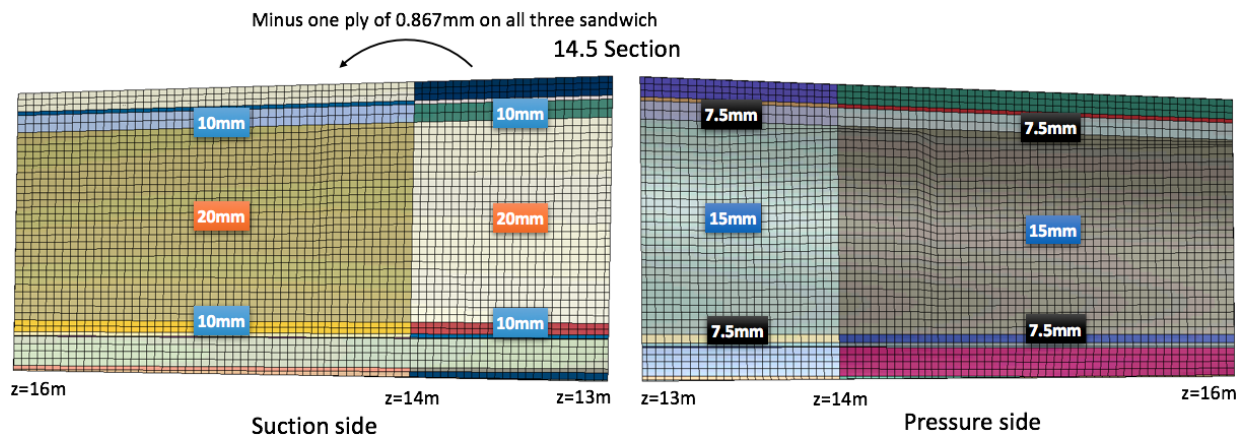


Figure 7.6: Core thickness of the sandwich sections on both sides of the 14.5 blade section.

On the other hand, it was found that the pressure side of the 19.4 section sees a drop in core thickness of 33% about 1 m from the tip boundary (Figure 7.7). This is quite a considerable difference. A simple calculation using Equation 7.1, demonstrates that it equates to an approximate reduction in flexural rigidity of 56%. It therefore strongly insinuates why the simulation showed the blade to buckle at this location.

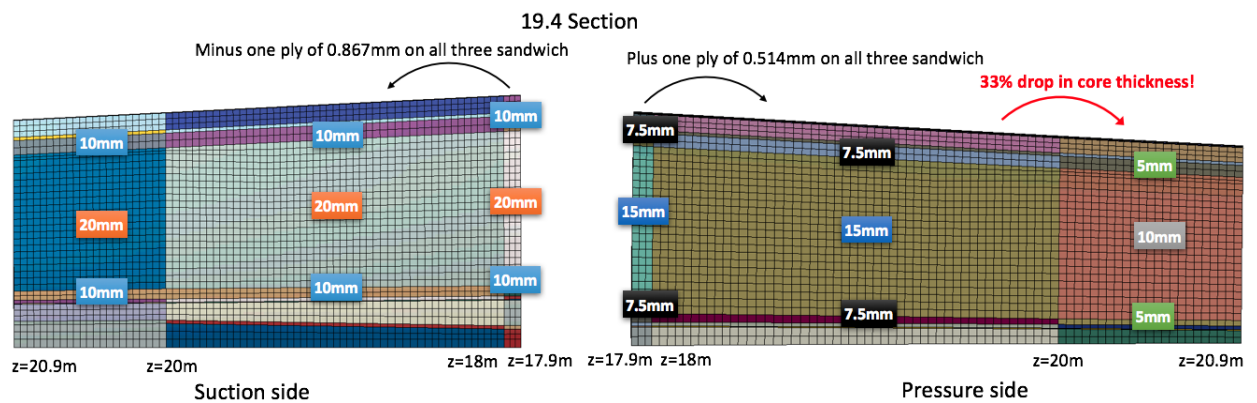
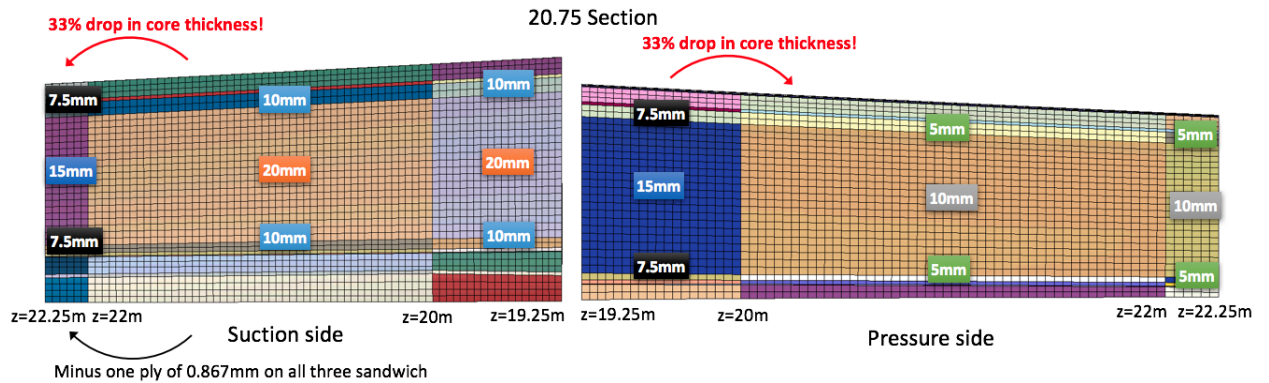


Figure 7.7: Core thickness of the sandwich sections on both sides of the 19.4 blade section.

Interestingly, the 20.75 section has a 33% drop in stiffness on both pressure and suction side panels, at different  $z$ -locations (as seen in Figure 7.8). This is in great accordance with the previous finding of this blade section having two buckling wave solutions. The location of these buckling waves also roughly match with where the relatively thinner sandwich panels are located.



**Figure 7.8:** Core thickness of the sandwich sections on both sides of the 20.75 blade section.

Finally, Figure 7.9 demonstrates that there is a region on the suction side panel near the tip side that has a core thickness 33% lower than the rest of that panel. Again, this agrees very well with where the blade section buckled in the simulations.

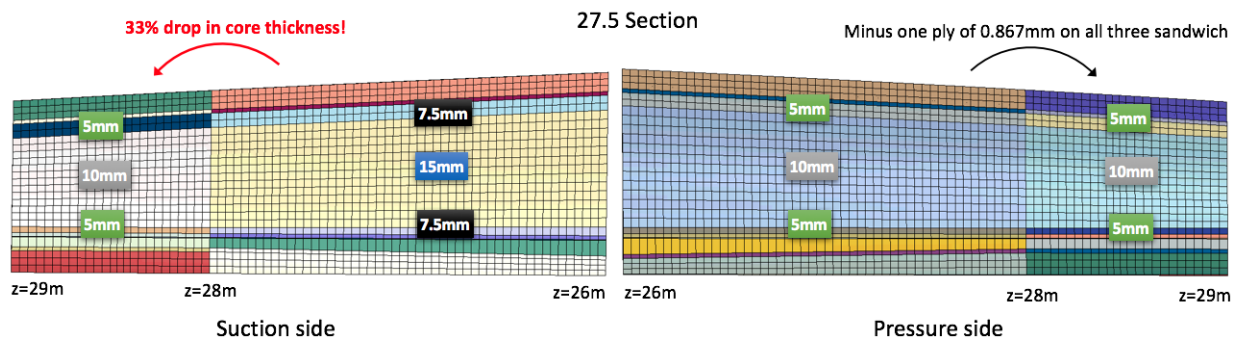


**Figure 7.9:** Core thickness of the sandwich sections on both sides of the 27.5 blade section.

In order to more confidently assess that the varying core thickness indeed changes the buckling wave location, an extra test was performed. The idea is that if the core thickness is made to be constant with respect to the  $z$ -direction in the 19.4, 20.75 and 27.5 sections, then the buckling wave would be expected to shift and potentially lie in the center, such as for the 14.5 section. For this test, the core thickness of the pressure side panel of the 19.4 section was made constant at [7.5mm, 15mm, 7.5mm], the core thickness of the suction side panel of the 20.75 section was made constant at [10mm, 20mm, 10mm] and for the pressure side panel at thickness [5mm, 10mm, 5mm] and finally, the suction side panel of the 27.5 piece was made to have a core thickness of [7.5mm, 15mm, 7.5mm]. To conclude, when there was a difference in core thickness on a given panel, the core thickness of the smaller area was changed such that it matched the core thickness of the largest area of that panel.

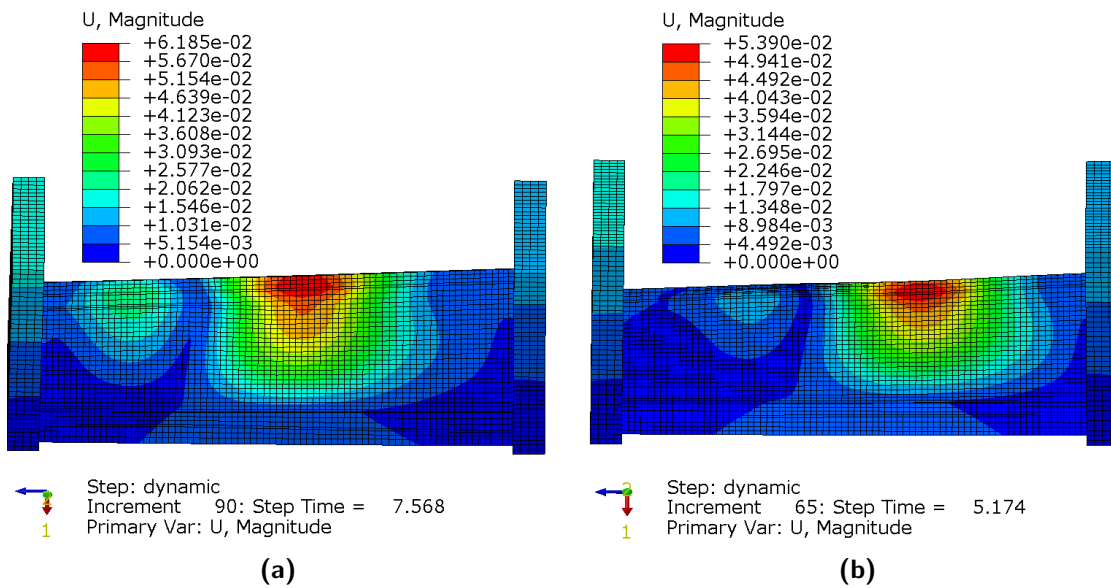


**Figure 7.10:** a) Displacement field of the 19.4 section with uniform core thickness on each panels, right after buckling. b) Displacement field of the 20.75 section with uniform core thickness on each panels, right after buckling.

Figure 7.10 reveals that the 19.4 and 20.75 sections do in fact buckle relatively close to the center when their core thickness is constant. This is not true for the 27.5 section, however, although the buckling wave did shift slightly towards the center (Figure 7.11a and Figure 7.11b). Since the tip end also saw a ply drop of 0.867 mm, therefore lowering  $E_f$  another test was done with this ply being added such that the face thickness is also constant across the panel. Figure 7.11c shows that this further shifted the wave towards the center. It demonstrates that the face thickness can also have an important influence on the buckling wave location. This becomes more important when the core thickness is lower, which is exactly the case here.

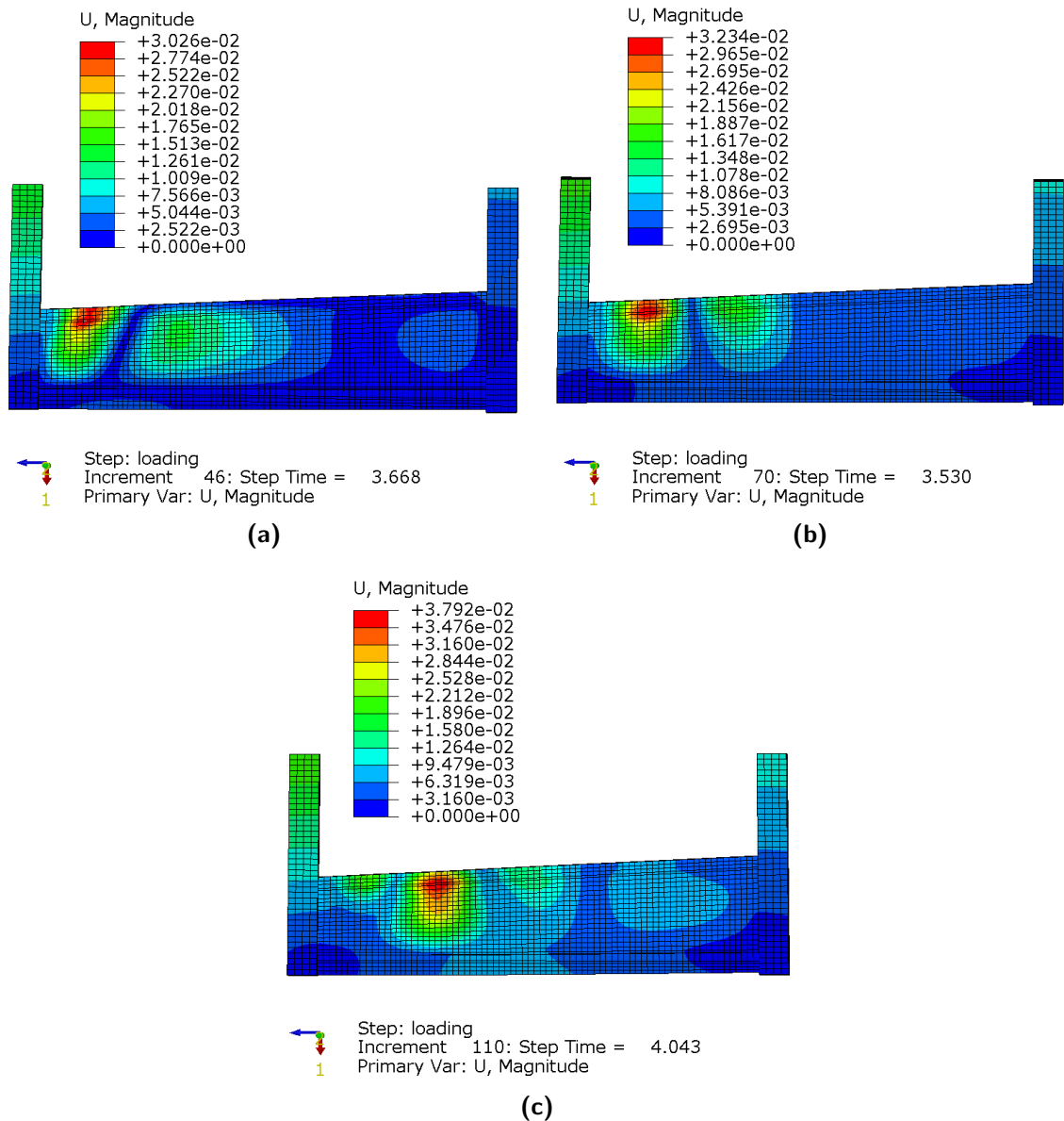


**Figure 7.11:** Displacement field of the 27.5 section at buckling load a) Original blade section without modifications of the composite sandwich. b) Blade section with uniform core thickness on each panels c) Blade section with uniform core and face of the composite sandwich of both panels.

### 7.3 Discussion

We can conclude that since the buckling wave location of the 27.5 section does not lie in the center of the blade section after making all sandwich constructions be invariant with respect to the  $z$ -direction, geometrical effects do also play a role and is especially prominent for this specific section. Looking back at Figure 7.4 does show the distance between panels to go down significantly more from one end to the other for the 27.5 section compared with the other blade sections. It is believed to be the reason why the

buckling wave location of the 27.5 section still lies closer to the tip after the composite property differences are ruled out, while it does not happen for the other sections. It also seem to confirm why the buckling wave of the 27.5 section was so close to the tip end in the first place. This would be due to seeing significant effects from both the geometry and composite design.

A very important point to talk about is the comparison of the core thickness distribution seen in the model vs. in a real blade. While the model showed a very significant step change in core thickness at certain locations along the z-direction, this is not how it looks in a real blade. Typically, core sheets of constant thickness are separated by smaller transition core pieces that linearly go from one thickness to the other. The tapering of these transition sections are suggested to fall in between 1:3 to 1:10 according to [46]. The abrupt jump in core thickness in the model used is not ideal and could significantly affect any analysis to precisely shift the buckling wave. This model was fine for simulations involving the entire blade but is not recommended for analysis on a small section of the blade. It is recommended that the model be updated so as to have more steps in the transition regions or to instead use tapered shell elements or solid elements in these regions.

On a side note, the pressure side panel was found to always have a lower core thickness than the suction side panel. This, along with the curvature of the blade section, might explain why the blade sections always buckle towards the pressure side.

The main concluding remarks of this chapter are:

- Core thickness distribution greatly influences where the blade will buckle. This is because it is the variable that most affects the flexural rigidity of sandwich constructions and the majority of the pressure and suction panels are made of sandwich constructions.
- Face thickness and modulus also has an impact on flexural rigidity of sandwich structures but it is more relevant when the core thickness is smaller, such as for blade regions closer to the blade tip (i.e farther in the z-direction).
- Geometrical effects also play a role in influencing the buckling wave location but was seen to have a significant role only closer to the blade tip. This is likely because the distance between the trailing edge panel decreases at a faster rate when going from root to tip. This is explained from a reduction in chord length but also from a steeper reduction in airfoil thickness to chord ratio towards the blade tip.
- It would be preferable to use a blade model that does not have such abrupt change in thickness. While this blade model was appropriate for simulations involving the entire blade, it is not so appropriate for the level of detail required in analyzing relatively small sections of the full blade. The model could be improved by having more composite sections, or to use tapered shell or solid elements when needed.

In the next chapter, an attempt is made at shifting the buckling wave towards the center of the blade section.

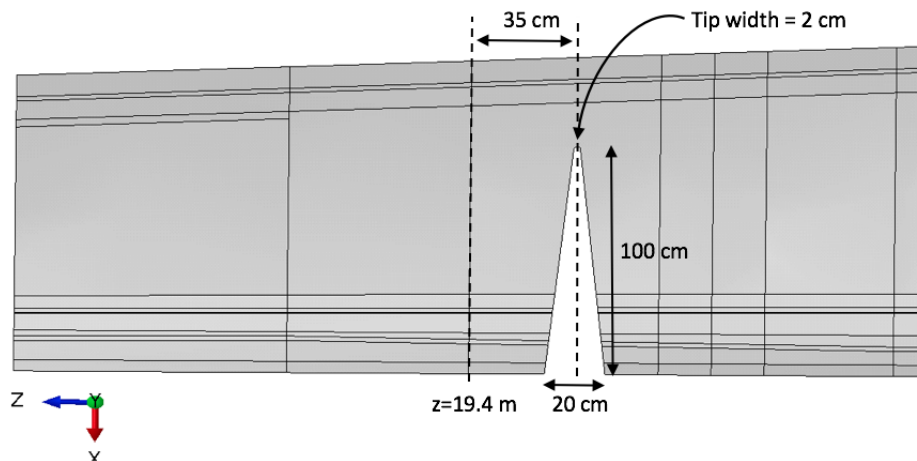


# Solutions to Translate the Buckling Wave

In this chapter, a first attempt is made at shifting the buckling wave towards the center of the section. The knowledge gained from this attempt, along with the information gained in the last chapter are then used to devise and discuss future solutions that appear promising.

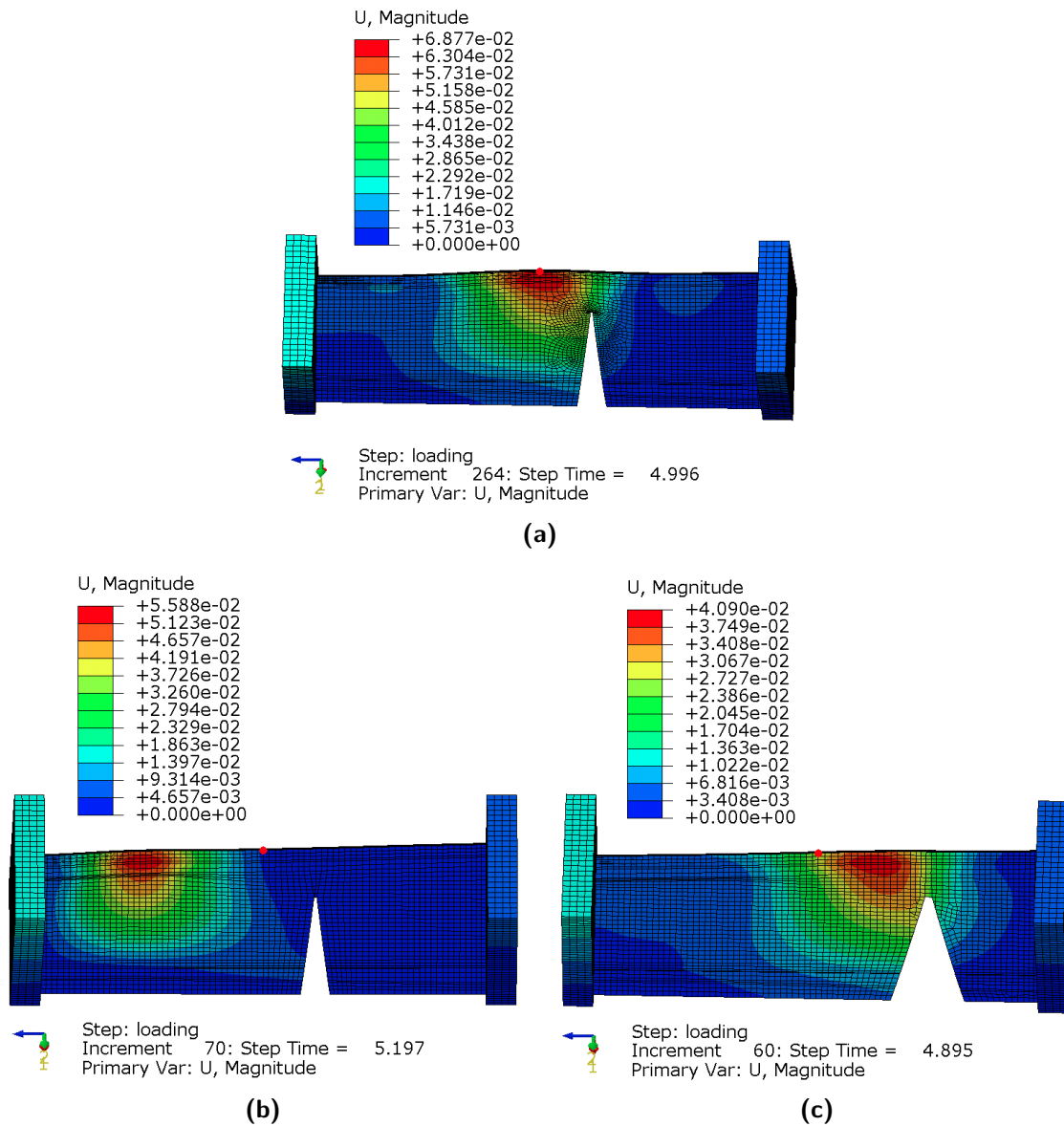
## 8.1 Cutting Away a Section of the Blade

One idea to shift the buckling wave towards the center of the specimen is to reduce the flexural rigidity of an intended region by cutting away a section of the blade. This method was attempted on the 19.4 section since the buckling wave of this section is clearly near one of the boundaries and because it was cut to have a strain distribution that matches that of the full-scale blade under LTT loading. As was discovered in the last chapter, the pressure side panel of the 19.4 has a region of approximately 1 m in length towards the tip side that has considerably lower flexural rigidity due to a core thickness that is 33% lower than the rest of the panel. The idea is then to cut away part of the region that has higher flexural rigidity in order for the overall flexural rigidity to be more balanced along the blade piece. The blade section was cut with the goal of having the buckling wave as close as possible to the middle of the section while keeping the cut as far away as possible from the trailing edge tip. After many iterations, a final design for the cut was obtained (Figure 8.1). The cut was done in the z-x plane and cuts through both panels. It is in the form of a trapezoid shape in order to minimize the amount of material taken out close to the trailing edge tip and prevent a stress singularity that would have arisen from a triangular cut. Fillets of 1 cm radius was also used at the the top two edges to make the surface smoother and potentially alleviate stress concentrations.



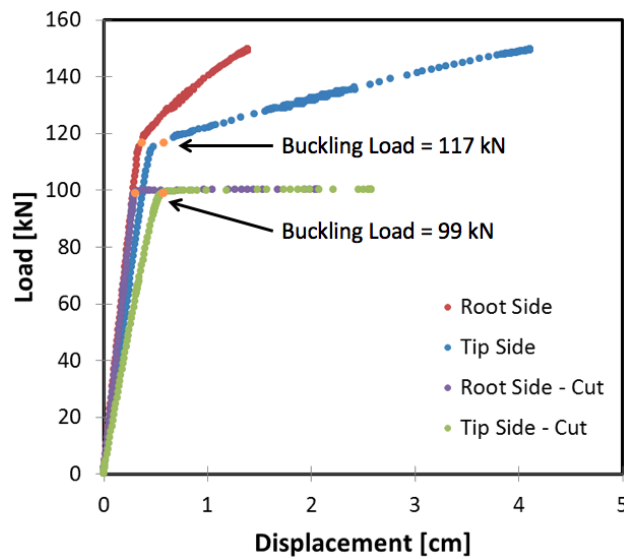
**Figure 8.1:** Location and dimension of the trapezoid cut in the 19.4 section. The cut was done in the  $z$ - $x$  plane.

Figure 8.2a demonstrates that the cut was able to make the blade buckle right in the center of the section! The red dot is exactly at the middle and so this shows how well in the center the buckling wave is. It is also worth mentioning the findings of similar cuts on the buckling wave. If the cut is slightly shorter with a height of  $95 \text{ cm}$ , the buckling wave hardly moves (Figure 8.2b). Cuts lower than  $95 \text{ cm}$  therefore also do not appear to have any significant effect on the buckling wave location. Another finding is how the buckling wave follows the cut when the cut is moved along the  $z$ -direction (Figure 8.2c).



**Figure 8.2:** a) Displacement field of the 19.4 section with final cut, at the buckling load of 99.0 kN. b) Displacement field with cut that has a height of 95 cm c) Displacement field with cut of 100 cm height and shifted to the right by 75 cm. This cut is slightly different with a base width of 50 cm and tip width of 5 cm.

The load-displacement diagram of Figure 8.3 shows that the buckling load for the specimen with the cut is slightly lower than without the cut, at 99 kN instead of 117 kN. This behavior is expected because the cut weakened the specimen.



**Figure 8.3:** Load-displacement diagram of the 19.4 section with and without cut.

One potential drawback of this method is the likelihood of a stress concentration at the cut tip. Figure 8.4 shows that the blade section would in fact be expected to fail at the cut tip. This would happen right before the blade buckles, at a load of 97.6 kN. The main problem here is that failure would not happen like it would if no cut was present. It is not how the blade would fail in full-scale testing and in the field and so it defeats the purpose of doing a sub-component test.

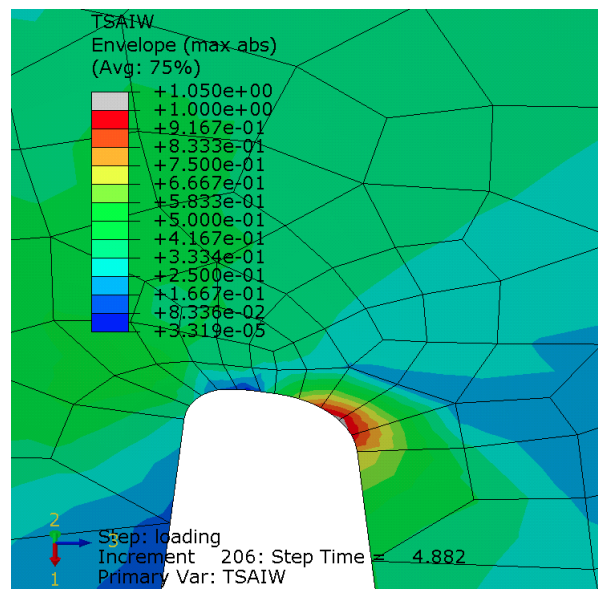


**Figure 8.4:** Tsai-Wu field for the 19.4 section with final cut, at a failure load of 97.6 kN.

Finally, the longitudinal strain was extracted at the middle cross-section and compared with the longitudinal strain without the cut at a load of 20 kN. Figure 8.5 shows that the section above the cut sees most of the load while the bottom section hardly sees any load.

Scaling the strain with the full-scale LTT strains shows that the strain distribution from the specimen with the cut is very off from the strain distribution of the full-scale LTT (Figure 8.6).

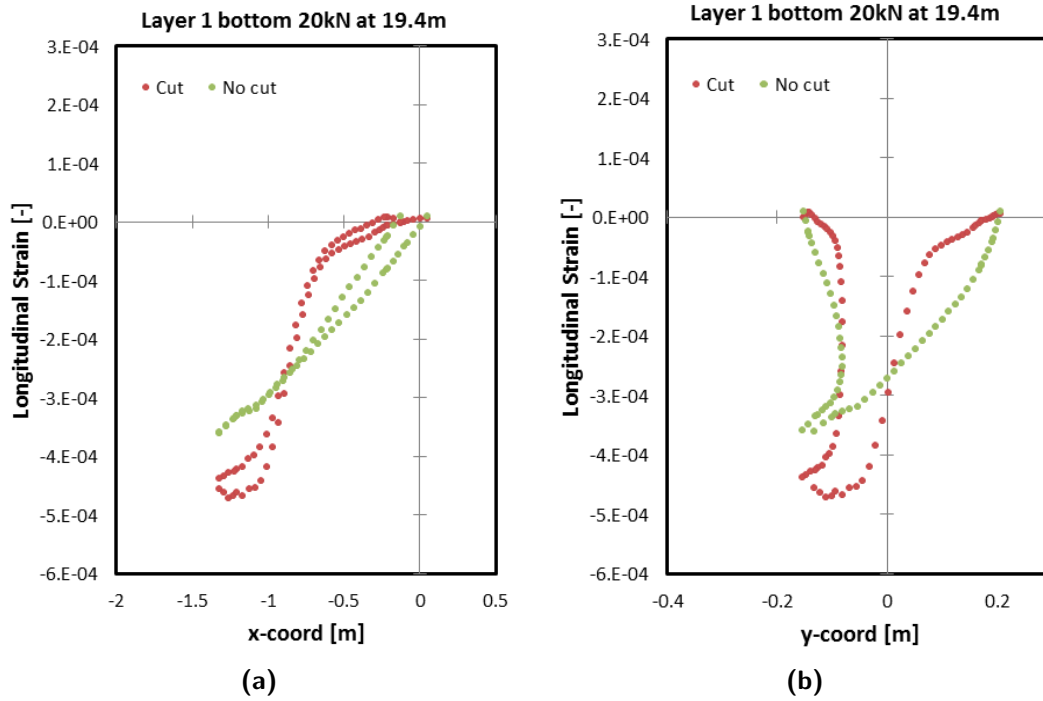


**Figure 8.5:** a) Comparison of longitudinal strain at 20 kN load along the path at  $z=19.4$  m vs. x-coordinate between cut and uncut specimen b) Same strain results vs. y-coordinate.

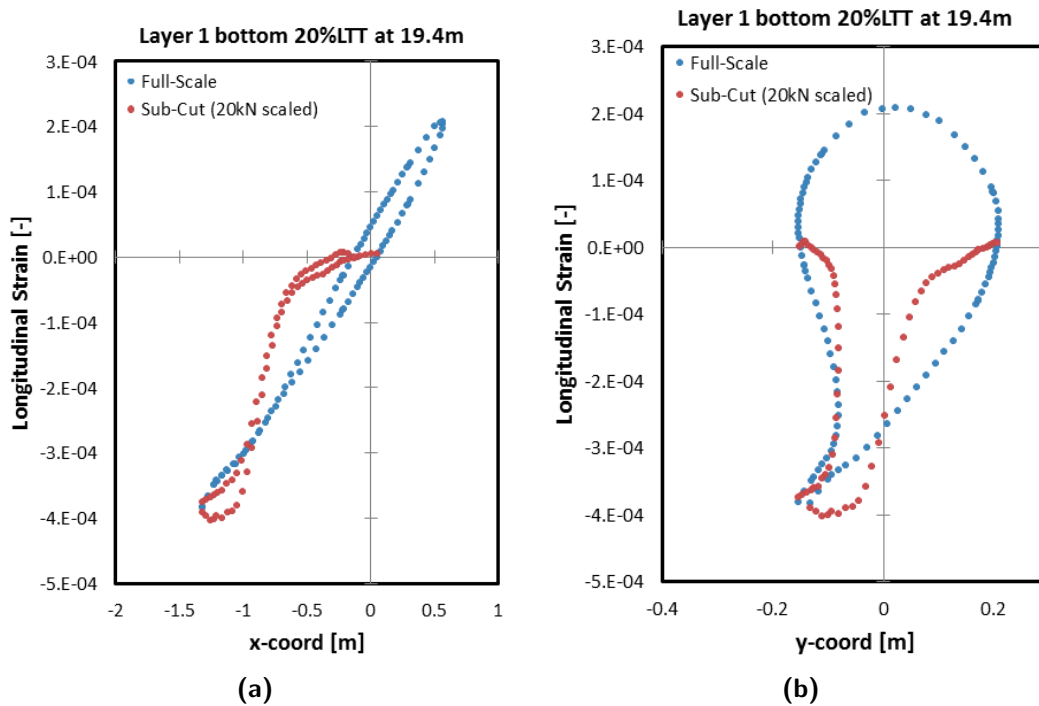


**Figure 8.6:** a) Longitudinal strain at 20% load along the path at  $z=19.4$  m vs.  $x$ -coordinate for full-scale blade and sub-component section with cut, the latter scaled from both 20 kN. b) Same strain results vs.  $y$ -coordinate.

The results clearly demonstrate that this cut is not a viable option. First, failure would occur at a load slightly lower than the buckling load and second, the load distribution on the section is not representative of what is seen during a full-scale test under LTT loading. Perhaps only cutting a section of the pressure side panel would work better but it appears like this method still has major problems. This cut shows that a gradual drop in flexural rigidity would most likely work better than a sudden drop in flexural rigidity. This would ensure that the load would not be concentrated in a particular region.

On a last note, this analysis might have been affected to a certain extent by the step transition in core thickness. This quite possibly made it harder for the buckling wave to move past this boundary when cuts at 95 cm or lower were attempted. It is recommended that this method be tried again with a more satisfactory model to see if better results can be obtained.

## 8.2 Recommended Solutions to Attempt Next

Before attempting any new solutions, it is first recommended to update the numerical model so that changes in thickness do not occur in one step. This would be done by breaking the step change in multiple steps or using tapered shell or solid elements. Only then will the model be able to reach the required level of preciseness to correctly evaluate the upcoming proposed solutions.

The findings from the previous chapter revealed that the buckling wave location was greatly affected by an imbalance in flexural rigidity. To successfully move the buckling wave towards the center, it would be good to balance this flexural rigidity. Now this was done fictitiously, by increasing or decreasing the core thickness in the model. This is however not a possible solution to apply on the physical blade sections. There are other ways to increase the flexural rigidity. Equation 7.1 tells us that the face modulus and thickness also affects flexural rigidity. One solution could be to apply over-lamination, which is the addition fabric (i.e plies), on the sandwich panels that have lower core thickness. This would physically be done via the method of hand lay-up. It would be difficult in practice to over-laminate the inside of the blade and so a first numerical simulation would look at over-laminating the exterior surface only. In the numerical model, plies would be added until the simulation shows the buckling wave to lay at the center of the section.

An alternate proposed solution to try would be to cut the specimen once again but in an extended horizontal fashion at about the mid-panel height. This cut would be located on the composite section having greater core thickness than the rest of the panel in order to reduce its flexural rigidity. The height of the cut would be the main optimized variable in order to effectively tune the flexural rigidity so that it becomes leveled along the specimen. For example, the cut could look like shown in Figure 8.7 on the pressure side of the 19.4 section. The figure also shows where over-lamination would be applied.

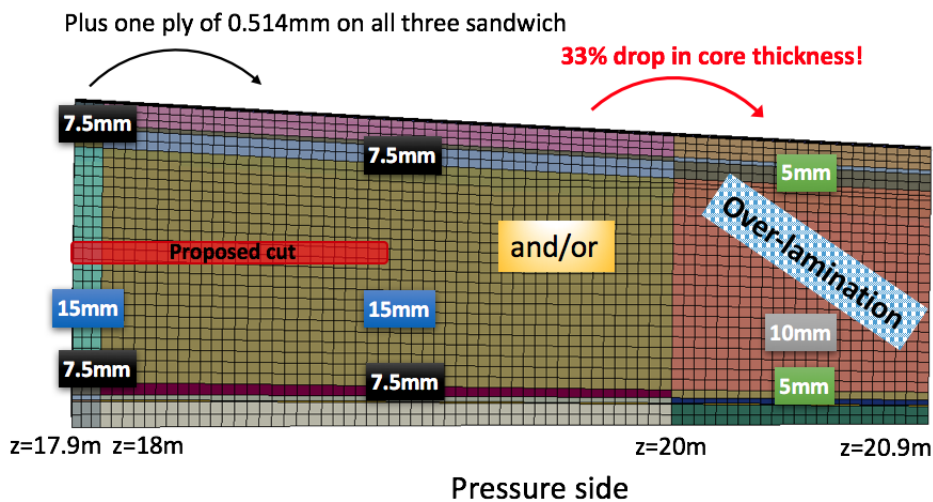


**Figure 8.7:** Example of proposed solutions to try on the pressure side panel of the 19.4 section.

Both methods would inherently account for any geometrical influence as well since the end goal is for the tuning to make the wave lie in the center. The great advantage from this methods is that it employs a fine tuning process that smoothly changes the flexural rigidity along the plate instead of implementing a drastic change such as shown by the cut attempted earlier in this chapter. This would make the longitudinal strain distribution likely remain quite close to the distribution from the full-scale blade under LTT loading. A combination of both methods could even be attempted.

Finally, perhaps future blade sections for sub-component testing of the trailing edge under

compression loads could be chosen more carefully such that they do not include any variation in core thickness, such as the 14.5 section in this analysis. This would automatically remove the highest factor in making the buckling wave lie away from the center. If it is not already predicted to be at the center, then it would still be easier to shift than if a varying core thickness was present.

To summarize, the two proposed solutions are:

- Over-lamination of areas that have lower core thickness.
- Horizontal cut at about the mid-height of the blade section in the region of higher core thickness.

---

## Chapter 9

---

# Conclusion

This research project uncovered many different findings that could be beneficial to the development of sub-component testing for cut-out wind turbine blade trailing edge sections. An attempt is made at listing the most important findings in an organized manner by first explicitly answering the sub-questions that were formulated at the end of Chapter 2, and then by answering the main research question of this research project.

Research sub-questions:

1. Which modeling methods and settings are recommended for successfully simulating the buckling test?
  - (a) Out of the linear eigenvalue buckling analysis, the non-linear static with Newton-Raphson formulation, the nonlinear static analysis with Riks formulation and the quasi-static analysis using the dynamic solver, the dynamic solver performed best. The small damping terms in its formulation provides greater stability.
  - (b) A mesh convergence study showed elements with characteristic element size of 4 cm to give results that have sufficiently converged.
  - (c) While technically not the most efficient method, applying the load distribution on the sub-component by modeling stiff plates worked quite well and made it easier to visualize the simulation. This set-up involved preventing nodal displacements where the hinges are located, applying a force at the top center of each plates and fixing the plates to the blade section via tie constraints.
  - (d) Defining surface-to-surface interaction between the blade panels was found to be extremely important because it prevented penetration of the panels.
  - (e) It was shown that S8R shell elements performed much better than S4 elements and so this element type was chosen.
  - (f) The boundary conditions that were applied at the bottom of the blade section were found not to be necessary.

- (g) Using the node at the glue center at the blade section boundary worked very well to display the load-displacement history and finding the buckling loads.
  - (h) The Tsai-Wu failure criterion was effective in determining where failure would occur. Further tricks in Abaqus allowed to find which ply would fail first, and also determine core shear failure.
  - (i) These simulation strategies allowed obtaining results that matched relatively well with what was seen in the first experiment. The Tsai-Wu failure criterion showed that the pressure side panel would be expected to fail right below the adhesive bondline, which is exactly where failure initiated during the first experiment. The model also predicts core shear failure, and this failure mode was also observed when DTU tested 34 m SSP blades to failure.
2. How well can the sub-component set-up mimic the load distribution acting on the trailing edge region of full-scale blades? What arrangement should be taken to ensure a good match?
    - (a) The longitudinal strain at the center cross-section of the blade section models was found to match very well with the longitudinal strain from simulating the full-scale blade model under LTT loading. For the three blade sections tested, the relative difference between these strains was found to be almost always less than 6%.
    - (b) In order to ensure a good match the blade section suction side and trailing edge panels should be cut at the neutral axis of the full-blade when it is acted under LTT loading.
    - (c) Slight tension was observed at the bottom of the sub-component sections, which is not seen in the full blade simulation. This is due to a bending moment that arises from loading the blade section above its elastic center.
  3. How does the buckling response vary between blade sections from different radial locations?
    - (a) The buckling load decreases when the blade section is taken farther towards the tip of the full blade. This is because the section is smaller and so less reaction moment counters the force acting on the plate. It can also be due to the composite sandwich panels having lower flexural rigidity in these sections.
    - (b) The buckling wave location was shown to vary. This is explained in the next sub-question.
    - (c) The buckling wave direction does not vary. It always buckled towards the pressure side. This is probably due to the curvature of the blade and the lower core thickness of the pressure side panel.
  4. What makes the buckling wave occur near the section boundary? Or in a more general sense, what are the main factors that determine where the buckling wave will be located?
    - (a) The largest factor that was found to determine the buckling wave location was the flexural rigidity distribution of the sandwich panels along the z-direction.

This is affected by both the core thickness and the facing thickness and modulus, with the former accounting for most of the difference in flexural rigidity. Some of the blade panels were found to have areas with 33% lower core thickness compared with the remaining areas of that panel. This in turn accounts for a drop of approximately 56% in flexural rigidity. This highly influenced were the blade buckled in the section.

- (b) The geometry of the blade sections was also found to have an effect on the buckling wave location. The main geometrical factor affecting the wave location is the change in distance between the pressure and suction side panels from one end of the blade section to the other. This difference was found to be especially high on the 27.5 m which in turn can explain why the buckling wave occurred closer to the tip end. It can therefore be assumed that geometrical effects play a larger role when sections are taken closer to the blade tip.

Main research question: *What is the best solution or set of solutions for moving the buckling wave towards the center of trailing edge sub-component specimens so as to solve boundary effect problems while keeping a load distribution that is representative of what is seen in the trailing edge region of full-scale blade when this region is under compression.*

First, for the load distribution to match with the full blade, the blade section needs to be cut where the neutral axis lies on the full-scale blade when loaded under LTT loading. This by defaults provides a very good match in longitudinal strain which is an indicator that the load distribution is approximately the same. When strategies are employed the shift the buckling wave, the stiffness of the blade inherently has to change and if this change is too abrupt, then the strain distribution will be off. This was shown in Chapter 9 by cutting out a significant portion of the blade. The change in stiffness, or flexural rigidity, should therefore be relatively smooth.

Since a varying flexural rigidity of the sandwich construction, which makes up most of the trailing edge panels, along the z-direction significantly affects the buckling wave location, the solution should try to balance this flexural rigidity on the panel that sees the variation. This can be done two ways; by reducing the flexural rigidity where it is higher and/or increasing the flexural rigidity where it is lower. One recommended solution to increase this flexural rigidity is by applying more plies on the region (i.e over-lamination). Alternatively, the flexural rigidity could be reduced by cutting a small horizontal slab at about the mid-height of the specimen.

To perform these extra studies, it is recommended that that the numerical model be improved by having a more gradual (and representative) thickness transition between regions. This could be done by stepping up the thickness incrementally from simply having more composite sections or by using tapered or solid shell elements.

It is hoped that this thesis provided valuable insights on the buckling behavior of trailing edge sub-component sections and the findings will fuel further research in this area.



---

## References

- [1] S. Sheng, "Report on Wind Turbine Subsystem Reliability - A Survey of Various Databases," *NREL/PR-5000-59111*, National Renewable Energy Laboratory, 2013.
- [2] W. Liu, Y. Ma, X. Su, and K. Huang, "Buckling Analysis of Wind Turbine Blade Using Pressure Distributions Obtained from CFD," no. 2007, pp. 2–5, 2009.
- [3] M. A. Eder, K. Branner, P. Berring, F. Belloni, H. S. Toft, J. D. Sørensen, A. Corre, T. Lindby, A. Quispitupa, and T. K. Petersen, "Experimental Blade Research - Phase 2," no. March, 2015.
- [4] International Electrotechnical Commission, "IEC 61400-23, Wind turbines Part 23: Full-scale structural testing of rotor blades," 2014.
- [5] DNV GL, "DNVGL-ST-0376 Standard - Rotor blades for wind turbines," 2015.
- [6] K. Branner, A. Antoniou, D. Lekou, I. Nuin, and R. Nijssen, "Methodology for testing subcomponents ; background and motivation for subcomponent testing of wind turbine rotor blades," tech. rep., Centre for Renewable Energy Sources and Saving, 2015.
- [7] B. H. Sun, K. Y. Yeh, and F. P. J. Rimrott, "On the Buckling of Structures," *Technische Mecahnik*, pp. 129–140, 1995.
- [8] C. Felippa, "Stability of Structures: Basic Concepts," 2015.
- [9] Det Norske Veritas, "DNV-OS-C501 Composite Components," no. November, p. 250, 2013.
- [10] Det Norske Veritas, "Design and Manufacture of Wind Turbine Blades, Offshore and Onshore Wind Turbines," *DNV Standard, DNV-DS-J102*, no. OCTOBER, 2010.
- [11] C. Felippa, "Imperfections," 2016.
- [12] F. Jensen and K. Branner, *Advances in Wind Turbine Blade Design and Materials*. Woodhead Publishing Limited, 2013.

- [13] ANSYS Inc., “Chapter 7- Buckling Analysis,” 1998.
- [14] P. M. Kurowski and T. P. Kurowski, “Buckling Analysis with FEA,” 2011.
- [15] M. Bak, “Nonlinear Buckling Analysis Using Workbench v15,” 2014.
- [16] H. Sönerlind, “Buckling, When Structures Suddenly Collapse,” 2014.
- [17] R. D. Cook, D. S. Malkus, M. E. Plesha, and R. J. W. Witt, *Concept and Applications of Finite Element Analysis*. John Wiley & Sons, Inc, 4th ed., 2002.
- [18] S. Krenk, *Non-Linear Modeling and Analysis of Solids and Structures*. New York: Cambridge University Press, 2009.
- [19] J. Sun, K. Lee, and H. Lee, “Comparison of implicit and explicit finite element methods for dynamic problems,” *Journal of Materials Processing Technology*, vol. 105, no. 1-2, pp. 110–118, 2000.
- [20] N. Gaudern and D. D. Symons, “Comparison of Theoretical and Numerical Buckling Loads for Wind Turbine Blade Panels,” *Wind Engineering*, vol. 34, no. 2, pp. 193–206, 2010.
- [21] P. U. Haselbach, M. A. Eder, and F. Belloni, “A comprehensive investigation of trailing edge damage in a wind turbine rotor blade,” *Wind Energy*, 2016.
- [22] Germanischer Lloyd, “Guideline for the Certification of Offshore Wind Turbines,” 2012.
- [23] P. U. Haselbach and K. Branner, “Initiation of trailing edge failure in full-scale wind turbine blade test,” *Engineering Fracture Mechanics*, 2016.
- [24] E. R. Jørgensen, K. K. Borum, M. Mcgugan, C. L. Thomsen, F. M. Jensen, C. P. Debel, and B. F. Sørensen, “Full scale testing of wind turbine blade to failure - flapwise loading,” 2004.
- [25] B. F. Sørensen, E. Jørgensen, C. P. Debel, F. M. Jensen, H. M. Jensen, T. K. Jacobsen, and K. M. Halling, *Improved design of large wind turbine blade of fibre composites based on studies of scale effects (Phase 1) - Summary Report*. Roskilde: Risø-R-1390(EN), 2004.
- [26] M. A. Eder and R. D. Bitsche, “Fracture analysis of adhesive joints in wind turbine blades,” *Wind Energy*, vol. 18, no. 6, pp. 1007–1022, 2015.
- [27] M. Eder, R. Bitsche, M. Nielsen, and K. Branner, “A practical approach to fracture analysis at the trailing edge of wind turbine rotor blades,” *Wind Energy*, vol. 17, no. 3, pp. 483–497, 2014.
- [28] P. U. Haselbach, R. D. Bitsche, and K. Branner, “The effect of delaminations on local buckling in wind turbine blades,” *Renewable Energy*, vol. 85, pp. 295–305, 2016.
- [29] L. Boni, D. Fanteria, and A. Lanciotti, “Post-buckling behaviour of flat stiffened composite panels: Experiments vs. analysis,” *Composite Structures*, vol. 94, no. 12, pp. 3421–3433, 2012.

- [30] M. A. Arbelo, S. F. M. de Almeida, and M. V. Donadon, “An experimental and numerical analysis for the post-buckling behavior of composite shear webs,” *Composite Structures*, vol. 93, no. 2, pp. 465–473, 2011.
- [31] S. Guo, D. Li, X. Zhang, and J. Xiang, “Buckling and post-buckling of a composite C-section with cutout and flange reinforcement,” *Composites Part B: Engineering*, vol. 60, pp. 119–124, 2014.
- [32] T. Kubiak, Z. Kolakowski, J. Swiniarski, M. Urbaniak, and A. Gliszczynski, “Local buckling and post-buckling of composite channel-section beams Numerical and experimental investigations,” *Composites Part B: Engineering*, vol. 91, pp. 176–188, 2016.
- [33] L. Lanzi, “A numerical and experimental investigation on composite stiffened panels into post-buckling,” *Thin-Walled Structures*, vol. 42, no. 12, pp. 1645–1664, 2004.
- [34] Y. B. Kwon, B. S. Kim, and G. J. Hancock, “Compression tests of high strength cold-formed steel channels with buckling interaction,” *Journal of Constructional Steel Research*, vol. 65, no. 2, pp. 278–289, 2009.
- [35] P. Kankeri, P. K. Ganesh Mahidhar, S. S. Prakash, and M. Ramji, “Experimental study on behavior of GFRP stiffened panels under compression,” *Ocean Engineering*, vol. 114, pp. 290–302, 2015.
- [36] M. A. Arbelo, K. Kalnins, O. Ozolins, E. Skukis, S. G. P. Castro, and R. Degenhardt, “Experimental and numerical estimation of buckling load on unstiffened cylindrical shells using a vibration correlation technique,” *Thin-Walled Structures*, vol. 94, pp. 273–279, 2015.
- [37] Dassault Systèmes, “Abaqus 6.14 Online Documentation,” 2014.
- [38] Dassault Systèmes, “28.1.1 Solid (continuum) elements.”
- [39] I. M. Daniel and O. Ishai, *Engineering Mechanics of Composite Materials*. New York: Oxford University Press, 1st ed., 1994.
- [40] Dassault Systèmes, “22.2.3 Plane stress orthotropic failure measures.”
- [41] Y. SudhirSastry, P. R. Budarapu, N. Madhavi, and Y. Krishna, “Buckling analysis of thin wall stiffened composite panels,” *Computational Materials Science*, vol. 96, no. JANUARY, pp. 459–471, 2015.
- [42] Dassault Systèmes, “42.6.2 Understanding result value averaging.”
- [43] M. Hansen, *Aerodynamics of Wind Turbines*. London: Earthscan, 2nd ed., 2008.
- [44] J. M. Gere, “Mechanics of Materials,” *Mechanics of Materials*, p. 913, 2008.
- [45] D. Zenkert, *Laminate and Sandwich Structures. An Introduction to Sandwich Structures. Notes for the course: Laminate and Sandwich Structures*. Kgs. Lyngby, Denmark: Technical University of Denmark, Department of Mechanical Engineering, 2nd ed., 2009.
- [46] Germanischer Lloyd, “Guideline for the Certification of Wind Turbines,” 2010.

